Longitudinal Analysis of Extreme Prematurity: a Neuroimage Investigation of Early Brain Development

Eliza Orăşanu

A dissertation submitted in partial fulfillment

of the requirements for the degree of

Doctor of Philosophy

of the

University College London.

Centre for Medical Image Computing

2016

I, Eliza Orăşanu, confirm that the work presented in this thesis is my own.

Where information has been derived from other sources, I confirm that this has been indicated in the thesis.

Abstract

Brain development is a complex process, and disruptions from its normal course may affect the later neurological outcome of an individual. Preterm infants are at higher risk of disability, since a substantial part of brain development happens outside the mother's womb, making it vulnerable to a range of insults. Understanding the early brain development during the preterm period is of critical importance and magnetic resonance imaging (MRI) allows us to investigate this. Methodologically, this is a challenging task, as classical approaches of studying longitudinal development over this period do not cope with the large changes taking place.

This thesis focuses on the development of tools to study the changes in cortical folding, shape of different brain structures and microstructural changes over the preterm period from longitudinal data of extremely preterm-born infants. It describes a tissue segmentation pipeline, optimised on a postmortem fetal dataset, and then focuses on finding longitudinal correspondences between the preterm and term-equivalent brain regions and structures in extremely preterm-born infants using MRI.

Three novel registration techniques are proposed for longitudinal registration of this challenging data. These are based on matching the spectral components associated with either the cortical surfaces, diffusion tensor images, or both. These allow us to quantify longitudinal changes in different brain regions and structures. We investigated changes in cortical folding of different lobes, microstructural changes and tracts in the white matter, cortical thickness and changes in cortical fractional anisotropy and mean diffusivity. We used cortical surface registration to look at shape differences between controls and extremely preterm-born young adults to gain an insight into the long-term impact of prematurity.

This research may contribute to the development of early biomarkers for predicting the neurological outcome of preterm infants and illuminate our understanding of brain development during this crucial period.

Acknowledgements

I would like to firstly thank my primary supervisor, Professor Sébastien Ourselin, for his guidance, inspiration, moral support and advice over the last years. I am very grateful for his enthusiasm and motivating me throughout my PhD.

I am also grateful to my secondary supervisor, Professor Neil Marlow, for his helpful comments and support over the course of my PhD. His overview of the direction of my thesis has been both insightful and motivating.

My gratitude goes as well to Dr. Andrew Melbourne, who provided me valuable guidance and everyday support over the course of the last years, and various advice concerning my research, writing, and running. I also offer my thanks to all my internal and external collaborators, especially: Marco, who helped me with all the maths and making my papers sound geeky; Marc, the registration master; Jorge, the segmentation master; and Hervé, who introduced me to the world of spectral matching.

I am very thankful to the Neurophysics Department at the Max Planck Institute (MPI) for Cognitive and Brain Sciences in Leipzig, Germany, in particular Dr. Pierre-Louis Bazin and Prof. Nikolaus Weiskopf, for the warm welcome and support over the 4 months I spent with them.

I would like to thank all my frolleagues (friends/colleagues) from Centre for Medical Image Computing (CMIC) and MPI, especially Zach, Felix, Alex, Mark, Maria, Julia and Sophia, for all the laughter, frustrations, cookies and litres of coffee shared, and pulling through all the deadlines with me.

Many thanks to all my friends from all over the world who always made time to catch up, spontaneously travel with me and patiently listen to my PhD-related (and other) problems.

A very special thanks to my parents, grandparents and Polly. Without them I would not be who and where I am today.

Publication List

Peer-reviewed Journal papers

1. **Orasanu, E.**, Melbourne, Atkinson, D., Beckmann, J., Marlow, N., Ourselin, S., Shape analysis of the thalamus and cortical folding patterns in extremely preterm born young adults. *Submitted to Human Brain Mapping*, 2017

2. **Orasanu, E.**, Melbourne, A., Lorenzi, M., Lombaert, H., Modat, M., Eaton-Rosen, Z., Kendall, G.S., Robertson, N.J., Marlow, N., Ourselin, S., Tensor Spectral Matching of Diffusion Weighted Images: Application on Extremely Preterm-Born Neonates. *Submitted to MedIA*, 2016

3. **Orasanu, E.**, Melbourne, A., Cardoso, M.J., Lombaert, H., Kendall, G.S., Robertson, N.J., Marlow, N., Ourselin, S., Cortical folding of the preterm brain: a longitudinal analysis of extremely-preterm born neonates using spectral matching. Brain and Behaviour, 2016

4. Melbourne, A.; Eaton-Rosen, Z.; **Orasanu, E.**; Price, D.; Bainbridge, A.; Cardoso, M. J.; Kendall, G. S.; Robertson, N. J.; Marlow, N., Ourselin, S. Longitudinal development in the preterm thalamus and posterior white matter; MRI correlations between Diffusion Weighted Imaging and T2 relaxometry. Human Brain Mapping: 37(7), 2479-2492, 2016.

5. Dingwall, N., Chalk, A., Martin, T.I., Scott, C.J., Semedo, C., Le, Q., **Orasanu, E.**, Cardoso, J.M., Melbourne, A., Marlow, N., Ourselin, S., T2 relaxometry in the extremely-preterm brain at adolescence. MRI, 2016

6. Eaton-Rosen, Z., Melbourne, A., **Orasanu, E.**, Cardoso, M.J., Bainbridge, A., Kendall, G.S., Robertson, N.J., Marlow, N., Ourselin, S., Longitudinal measurement of the developing grey matter in preterm subjects using multi-modal MRI. NeuroImage, 111, 580-589, 2015

7. **Orasanu, E.**, Melbourne, A., Cardoso, M.J., Modat, M., Taylor, A.M., Thayyil, S., Ourselin, S., Brain volume estimation from post-mortem newborn and fetal MRI. NeuroImage: Clinical. 6: 438-444, 2014

Conference papers

1. **Orasanu, E.**, Bazin, P.L., Melbourne, A., Lorenzi, M., Lombaert, H., Kendall, G.S., Robertson, N.J., Weiskopf, N., Marlow, N., Ourselin, S., Longitudinal analysis of the preterm cortex

using multi-modal spectral matching. Accepted for Medical Image Computing and Computer-Assistance Intervention (MICCAI) Conference, 2016.

2. Eaton-Rosen, Z., Cardoso, M.J., Melbourne, A., **Orasanu, E.**, Bainbridge, A., Kendall, G.S., Robertson, N.J., Marlow, N., Ourselin, S., Fitting parametric models of diffusion MRI in regions of partial volume. In SPIE Medical Imaging, 2016

3. **Orasanu, E.**, Melbourne, A., Lorenzi, M., Modat, M., Lombaert, H., Eaton-Rosen, Z., Kendall, G.S., Robertson, N.J., Marlow, N., Ourselin, S., Tensor Spectral Matching of Diffusion Weighted Images. In Workshop on Spectral Analysis in Medical Imaging (SAMI), Medical Image Computing and Computer-Assistance Intervention (MICCAI) Conference, 2015

4. **Orasanu, E.**, Melbourne, A., Lombaert, H., Cardoso, M.J., Johnsen, S., Kendall, G.S., Robertson, N.J., Marlow, N., Ourselin, S., Pre-frontal cortical folding of the preterm brain: a longitudinal analysis of preterm-born neonates. In Workshop on Spatiotemporal Image Analysis for Longitudinal and Time-Series Image Data (STIA), Medical Image Computing and Computer-Assistance Intervention (MICCAI) Conference, 2014, LNCS 8682, pp. 3-12, 2015.

5. Eaton-Rosen, Z., Melbourne, A., **Orasanu, E.**, Modat, M., Bainbridge, A., Cardoso, M.J., Kendall, G.S., Robertson, N.J., Marlow, N., Ourselin, S., Longitudinal measurement of the developing thalamus in the very-preterm brain using multi-modal MRI. In Medical Image Computing and Computer-Assistance Intervention (MICCAI) Conference, 2014. LNCS, 201

Conference abstracts

1. **Orasanu, E.**, Melbourne, A., Modat, M., Lorenzi, M., Lombaert, H., Eaton-Rosen, Z., Robertson, N.J., Kendall, G.S., Marlow, N., Ourselin, S., Mapping longitudinal white matter changes in extremely preterm born infants. Oral Presentation at ISMRM, 2016. **Awarded ISMRM Summa Cum Laude, First Place Best Abstract Presentation in the Pediatrics Study Group and Third Place Best Abstract Presentation in the White Matter Study Group**

2. **Orasanu, E.**, Melbourne, A., Eaton-Rosen, Z., Atkinson, D., Lawan, J., Beckmann, J., Marlow, N., Ourselin, S., Local shape analysis of the thalamus in extremely preterm born young adults. Oral Presentation at ISMRM, 2016. **Awarded ISMRM Summa Cum Laude**

3. **Orasanu, E.**, Melbourne, A., Eaton-Rosen, Z., Atkinson, D., Saborowska, A., Beckmann, J., Marlow, N., Ourselin, S., Cortical folding patterns in extremely preterm born young adults. Electronic Poster at ISMRM, 2016.

4. Eaton-Rosen, Z., Melbourne, A., **Orasanu, E.**, Beckmann, J., Stevens, N., Atkinson, D., Marlow, N., Ourselin, S., White matter alterations in young adults born extremely preterm: a microstructural point of view. Traditional Poster at ISMRM, 2016.

5. Melbourne, A., **Orasanu, E.**, Eaton-Rosen, Z., Manuel J Cardoso, Beckmann, J., Smith, L., Atkinson, D., Marlow, N., Ourselin, S., Analysis of brain volume in a 19 year-old extremely- preterm

born cohort. Electronic Poster at ISMRM, 2016.

6. Melbourne, A., Eaton-Rosen, Z., **Orasanu, E.**, Beckmann, J., Saborowska, A., Atkinson, D., Marlow, N., Ourselin, S., Perfusion and diffusion in the extremely preterm young adult thalamus. Traditional Poster in ISMRM, 2016.

7. Melbourne, A., **Orasanu, E.**, Eaton-Rosen, Z., Beckmann, J., Saborowska, A., Atkinson, D., Marlow, N., Ourselin, S., Characterizing microstructure and shape of the extremely preterm 19 year-old corpus callosum. Traditional Poster at ISMRM, 2016.

8. **Orasanu, E.**, Melbourne, A., Lombaert, H., Cardoso, M.J., Kendall, G.S., Robertson, N.J., Marlow, N., Ourselin, S., Cortical folding of the preterm brain: a longitudinal analysis using spectral matching. Oral Presentation at Mind, Brain and Body Symposium, Berlin, Germany, 2016

9. **Orasanu, E.**, Melbourne, A., Cardoso, M.J., Modat, M., Taylor, A.M., Thayyil, S., Ourselin, S., Fully automated estimation of brain volumes in post-mortem newborn and stillborn infants. Traditional Poster at ISMRM 2014 (1517)

10. **Orasanu, E.**, Melbourne, A., Cardoso, M.J., Modat, M., Taylor, A.M., Thayyil, S., Ourselin, S., Average probabilistic brain atlases for post-mortem newborn and stillborn populations and application to tissue segmentation. Traditional Poster at ISMRM 2014 (2001)

11. Eaton-Rosen, Z., Melbourne, A., **Orasanu, E.**, Bainbridge, A., Kendall, G.S., Robertson, N.J., Marlow, N., Ourselin, S., Cortical maturation in the preterm period revealed using a multi-component diffusion-weighted MR model. Oral Presentation at ISMRM 2014, 80.

Contents

Abstract **3**

Acknowledgements **4**

Publication List **5**

Glossary of terms **15**

1 Introduction **17**

1.1 Problem statement 17

1.2 Thesis contributions 18

1.3 Thesis structure 19

2 Background **21**

2.1 Early brain development 21

2.1.1 Cortical development 22

2.1.2 Structural and microstructural changes 24

2.2 Impact of extreme prematurity on brain development 25

2.3 Overview of Magnetic Resonance Imaging (MRI) 26

2.4 Imaging of the early brain using MRI 27

2.4.1 Post-mortem Fetal MRI 28

2.4.2 MRI of extreme prematurity 29

2.5 Image processing techniques for early developmental data 32

2.5.1 Probabilistic atlases and tissue segmentation 32

2.5.2 Infant brain registration 33

2.6 Summary 37

3 Data and Image Preprocessing **38**

3.1 Post-mortem Fetal Data: MaRIAS 38

3.1.1 Subjects 38

3.1.2 Recruitment 39

3.1.3 MR Acquisition 39

3.1.4 Image Preprocessing . . . 39
3.2 Preterm Infant Data: Preterm Development Project . . . 39
3.2.1 Subjects . . . 39
3.2.2 MR Acquisition . . . 40
3.2.3 Image Preprocessing . . . 41
3.3 Preterm Young Adult Data: EPICure Study . . . 41
3.3.1 Subjects . . . 41
3.3.2 MR Acquisition . . . 42
3.3.3 Brain Segmentation . . . 42

4 Voxel-wise Image Analysis: Application to Post-mortem Fetal MRI 44
4.1 Methods . . . 45
4.1.1 Newborn Brain Segmentation . . . 45
4.1.2 Post-mortem Newborn Average Atlas . . . 45
4.1.3 Fetal Brain Segmentation . . . 46
4.1.4 Validation . . . 46
4.1.5 Eliminating Cerebral Fluid . . . 47
4.1.6 Post-mortem Cerebrum Weights . . . 47
4.2 Results . . . 47
4.2.1 Atlas-based Brain Segmentation . . . 47
4.2.2 Post-mortem Cerebrum Volumes . . . 48
4.2.3 Brain Growth Rates of Normal Development from Post-mortem MRI . . . 48
4.3 Discussion . . . 52
4.3.1 Post-mortem MRI as an alternative to conventional autopsy . . . 53
4.3.2 Brain growth rates from post-mortem MRI . . . 54
4.3.3 Limitations of voxel-wise intensity-based methods . . . 55

5 Spectral Graph Theory 56
5.1 Introduction to Graph Theory . . . 56
5.2 Matrices associated with a graph . . . 56
5.3 Spectral Decomposition of a Graph Laplacian . . . 57
5.4 Spectral Graph Methods in Medical Imaging . . . 59
5.5 Matching of the Spectral Representations . . . 59
5.6 Summary . . . 60

6 Surface Spectral Matching for Cortical Development during the Preterm Period 61
6.1 Methods . . . 62
6.1.1 Infant Brain Segmentation and Parcellation . . . 62
6.1.2 Triangular-based meshes . . . 64
6.1.3 Longitudinal Joint-Spectral Matching of Cortical Surfaces . . . 64

6.1.4 Consistency of surface matching . . . 65
6.1.5 Measurement of longitudinal development . . . 66
6.1.6 Longitudinal Differences: Group Analysis . . . 67
6.2 Results . . . 67
6.2.1 Joint-Spectral Matching Correspondence . . . 67
6.2.2 Consistency of surface matching . . . 68
6.2.3 Longitudinal brain development over the preterm period . . . 68
6.3 Discussion . . . 76

7 Surface Spectral Matching for Shape Analysis in the Epicure Data 81
7.1 Methods . . . 82
7.1.1 Image Processing . . . 82
7.1.2 Groupwise Analysis using Spectral Matching . . . 83
7.1.3 Statistical Analysis . . . 83
7.2 Results . . . 84
7.2.1 Volume and surface area . . . 84
7.2.2 Cortical folding patterns . . . 86
7.2.3 Thalamus shape analysis . . . 88
7.2.4 Cerebellum Shape Analysis . . . 88
7.3 Discussion . . . 92

8 Tensor Spectral Matching 93
8.1 Tensor Spectral Matching . . . 94
8.1.1 Computation of Tensor Spectral Components . . . 94
8.1.2 Tensor Spectral Matching (TSM): Spatial Correspondence estimation of DTI through spectral matching . . . 94
8.1.3 Combining global spectral features with local tensor information: TSM-DTI-TK 95
8.2 Experiment 1: Average Group Template of Adult Data . . . 96
8.2.1 Methods . . . 96
8.2.2 Results . . . 97
8.3 Experiment 2: Validation on Longitudinal Infant Data . . . 98
8.3.1 Methods . . . 98
8.3.2 Results . . . 98
8.4 Experiment 3: Application of TSM-DTI-TK to Longitudinal Extremely Preterm-Born Infant Data . . . 99
8.4.1 Methods . . . 99
8.4.2 Results . . . 100
8.5 Discussion . . . 101

9 Multi Modal Spectral Matching 105

9.1 Pairing Images using Multi-Modal Spectra (PIMMS) . . . 106
9.1.1 Level Set representation of surface boundary . . . 106
9.1.2 Spectral components of surface in image domain . . . 106
9.1.3 Combined Level Set and Diffusion Tensor Spectra . . . 108
9.1.4 Matching of multi-modal spectra . . . 108
9.2 Validation . . . 109
9.2.1 Comparison of PIMMS with Joint-Spectral Surface Matching . . . 109
9.2.2 Comparison of PIMMS with Multi-contrast Multi-scale Surface Registration (MMSR) . . . 109
9.3 Data processing and experiments . . . 110
9.3.1 Cortical Thickness . . . 110
9.3.2 Laminar Analysis . . . 110
9.3.3 Longitudinal and cross-sectional mapping . . . 111
9.4 Results . . . 111
9.4.1 Cortical Thickness, cortical FA and cortical MD . . . 111
9.4.2 Groupwise Analysis of Longitudinal Changes . . . 112
9.5 Discussion . . . 112

10 Discussion **116**

10.1 Summary and impact of results . . . 116
10.2 Future Research Directions . . . 120

11 Appendix **123**

A. Global Changes over the Preterm Period . . . 123
A.1. Volume and surface area over the preterm period . . . 123
A.2. Multivariate folding descriptor . . . 126

References **131**

List of Figures

2.1 Longitudinal T1-weighted MRI of the Preterm Brain 22
2.2 Longitudinal diffusion-weighted MRI of the Preterm Brain 24

3.1 Example Segmentation of EPICure Subject 43

4.1 Brain segmentation of MaRIAS dataset: Processing pipeline 46
4.2 MaRIAS Newborn Brain Segmentation 47
4.3 MaRIAS Fetal Brain Segmentation 48
4.4 Bland-Altman plot for MaRIAS newborn cohort 51
4.5 Bland-Altman plot for MaRIAS fetal cohort 51
4.6 Brain Growth Rates from Post-mortem Infant MRI 52
4.7 Cerebrum Density Estimation from Post-mortem MRI 54

5.1 Example Spectral Decomposition 58
5.2 Example of spectra of the Big Ben 58

6.1 Original Preterm Infant Brain Segmentation 62
6.2 Preterm Infant Brain Segmentation 63
6.3 Preterm Infant Brain Parcellation 64
6.4 Improvement of spectral matching using CPD for initialisation 65
6.5 Surface Spectral Matching Pipeline 65
6.6 Principal surface curvatures 66
6.7 Spectral components of a Preterm Infant 68
6.8 Regional vs. whole-brain Spectral Matching variation 69
6.9 Mean Curvature Changes during the Preterm Period 70
6.10 Gaussian Curvature Changes during the Preterm Period 70
6.11 Mean Curvature Changes during the Preterm Period in the Prefrontal Cortex 71
6.12 Gaussian Curvature Changes during the Preterm Period 72
6.13 Bending Energy during the Preterm Period in the Prefrontal Cortex 72
6.14 Mean Curvature Changes during the Preterm Period in the Temporal Lobe 73
6.15 Bending Energy during the Preterm Period in the Temporal Lobe 74
6.16 Mean Curvature Changes during the Preterm Period in the Occipital and Parietal Lobes . 75

6.17 Mean Curvature Changes during the Preterm Period in all infants for the Prefrontal and Temporal Lobes . . . 77
6.18 Mean Curvature Changes during the Preterm Period in all infants for the Occipital and Parietal Lobes . . . 78
6.19 Statistical Maps of Longitudinal Changes in Cortical Folding over the Preterm Period . . 79

7.1 Volume and surface area of the white matter . . . 84
7.2 Volume and surface area of the thalamus . . . 85
7.3 Volume and surface area of the cerebellum . . . 86
7.4 Local shape differences between the preterm and term mean white-grey matter boundary 87
7.5 Local shape differences between the female preterm and female term mean white-grey matter boundary . . . 87
7.6 Local shape differences between the male preterm and male term mean white-grey matter boundary . . . 87
7.7 Significance maps of white-grey matter group difference controlling for white matter volume and gender . . . 88
7.8 Local shape differences between the preterm and term mean thalamus . . . 89
7.9 Local shape differences between the female preterm and female term mean thalamus . . 89
7.10 Local shape differences between the male preterm and male term mean thalamus . . . 89
7.11 Significance maps of thalamus group difference controlling for thalamic volume and gender . . . 90
7.12 Local shape differences between the preterm and term mean cerebellum . . . 91
7.13 Local shape differences between preterm and female term mean cerebellum by gender . 91

8.1 Tensor Spectra for Sparks infant *c* . . . 95
8.2 Registration framework for TSM-DTI-TK . . . 96
8.3 Visual validation of TSM-DTI-TK on EPICure control data . . . 97
8.4 Quantitative validation of TSM-DTI-TK on EPICure control data . . . 98
8.5 Visual validation of TSM-DTI-TK on longitudinal Sparks preterm infant data . . . 99
8.6 Quantitative validation of TSM-DTI-TK on longitudinal Sparks preterm infant data . . . 100
8.7 Groupwise registration of Sparks preterm data using TSM-DTI-TK . . . 101
8.8 Longitudinal changes over the preterm period in the white matter from DTI . . . 102

9.2 Spectral modes of shape variation from level set and surface . . . 107
9.1 Level set of the white-grey matter boundary and its first 3 spectral modes of shape variation 107
9.3 Combined spectral modes from level set and diffusion tensor image . . . 108
9.4 Registration error maps of PIMMS, JSM and MMSR . . . 110
9.5 Registration pipeline for investigating longitudinal preterm changes in CT, cortical FA and MD . . . 111
9.6 Example maps of CT, cortical fractional FA and MD . . . 112

9.7 Average cortical changes per lobe in all infants as function of gestational age 113
9.8 Mean Longitudinal Rates of Change in CT, cortical FA and MD 114

10.1 Brain development in prematurity 119

11.1 Surface area and volume change for all 9 Sparks subjects of the left and right white matter 124
11.2 Surface area and volume change for all 9 Sparks subjects of the left and right prefrontal cortex 124
11.3 Surface area and volume change for all 9 Sparks subjects of the left and right temporal lobe 125
11.4 Surface area and volume change for all 9 Sparks subjects of the left and right parietal lobe 125
11.5 Surface area and volume change for all 9 Sparks subjects of the left and right occipital lobe 126
11.6 Group mean of the multivariate surface descriptors P(C,S) for the whole brain white matter left and right 127
11.7 Group mean of the multivariate surface descriptors P(C,S) for the prefrontal cortex left and right 128
11.8 Group mean of the multivariate surface descriptors P(C,S) for temporal left and right . . 129

List of Tables

2.1 Regional Development of Sulci and Gyri for the Last Trimester of Pregnancy (gestational weeks) [33] 23

3.1 Preterm Infant Subjects used in this study. Quality control was qualitatively established during preprocessing by visual inspection. 40

4.1 Dice overlap of automatic segmentation with manual segmentation for each structure amongst each cohort 48

4.2 Comparison between MRI weights, MRI manual weights and autopsy weights of the cerebrum for newborns. Density for cerebrum used to compute the weight from the MR volume: 1.08 g/mL. The threshold values used to remove the CSF from the MR segmentation are also included. The subjects for which manual segmentation was performed are indicated with *. 49

4.3 Comparison between MRI weights, MRI manual weights and autopsy weights of the cerebrum for fetuses. Density for cerebrum used to compute the weight from the MR volume: 1.08 g/mL. The threshold values used to remove the CSF from the MR segmentation are also included. The subjects for which manual segmentation was performed are indicated with *. 50

4.4 Brain growth rates from post-mortem infant MRI 50

6.1 Surface area increase as a function of equivalent gestational age in 9 preterm born infants, scanned both at early (31.6 weeks EGA) and term-equivalent age timepoints (41.7 weeks EGA) 75

9.1 Statistically significant (0.05 significance, FDR corrected) correlation coefficients between multi-modal cortex parameters in all four lobes. Negative values imply a negative correlation, while positive imply a direct positive correlation. The regions not mentioned did not have a significant correlation between certain parameters. 114

Glossary of terms

ADHD	Attention deficit hyperactivity disorder
AdaPT	Adaptive Preterm segmentation algorithm
C	Curvedness
cGM	Cortical Grey Matter
cortFA	Cortical Fractional Anisotropy
cortMD	Cortical Mean Diffusivity
CC	Corpus Callosum
CPD	Coherent Point Drift
CRUISE	Cortical Reconstruction Using Implicit Surface Evolution
CSF	Cerebrospinal Fluid
CT	Cortical Thickness
dGM	Deep Grey Matter
DT	Diffusion Tensor
DTI	Diffusion Tensor Imaging
DWI	Diffusion-weighted Imaging
DW-MRI	Diffusion-weighted Magnetic Resonance Imaging
EGA	Equivalent Gestational Age
EM	Expectation Maximisation
EPICure	Extreme Prematurity in Infancy - Cure
FA	Fractional Anisotropy
fMRI	Functional Magnetic Resonance Imaging
FOCUSR	Feature Oriented Correspondence using Spectral Regularisation
G	Gaussian Curvature
GA	Gestational Age
GAB	Gestational Age at Birth
GIF	Geodesic Information Flow
GM	Grey Matter
GW	Gestational Weeks
IQ	Intelligence Quotient

JSM	Joint-Spectral Matching
M	Mean Curvature
MaRIAS	Magnetic Resonance Imaging Autopsy Study
MD	Mean Diffusivity
MMSR	Multi-contrast Multi-scale Surface Registration
MR	Magnetic Resonance
MRI	Magnetic Resonance Imaging
NODDI	Neurite Orientation Dispersion and Density Imaging model
PFC	Prefrontal Cortex
PIMMS	Pairing Images using Multi Modal Spectra
PDF	Probability Density function
S	Shape Index
Sparks PDP	Sparks (UK Charity) Preterm Development Project
SPD matrix	semi-positive definite matrix
T1-w	T1-weighted imaging
T2-w	T2-weighted imaging
TE	Echo Time
TR	Relaxation Time
TSM	Tensor Spectral Matching
WM	White Matter

Chapter 1

Introduction

1.1 Problem statement

Early brain development is a complex process and understanding it and how disruptions from the natural course can affect it is one of the main challenges in neuroscience.

Development of the human brain is being intensively researched nowadays and it is a current area of interest for several other fields, including biology, medicine and computational anatomy. Being aware of each stage of brain development, and what is expected to be normal, can be crucial for diagnosis of disease and prediction of functional neurological outcome. Brain development can be investigated using MRI and this has been done in newborns and fetuses so that brain structures could be monitored as accurately as possible for different gestational ages.

Recent developments in technology have allowed the scientific community to give more insight into prenatal and neonatal life and to try to identify the reasons of mortality and disability among these populations. Non-invasive imaging techniques such as MRI have been improved and adapted for newborns and even for fetuses that are still inside the mother's womb. Compared to ultrasound modalities that are usually used for these patients, MRI offers a better resolution for soft tissue contrast and allows for a better understanding of the underlying structure of the organs, capturing more of their details.

Postmortem MRI has come into more common use, offering several advantages over conventional autopsy. It could be as efficient as conventional autopsy in establishing the causes of death in fetuses and neonates, as well as the risk of susceptibility in siblings and family members. Conventional autopsy rates are decreasing worldwide [76] because of its invasive nature, thus having a non-invasive alternative would be of great importance for advances in science and medicine. Furthermore, postmortem MRI can also give an insight into the early brain development, in cases where death was not caused by brain damage. Although there are more and more atlases that capture the brain growth in newborns, little is known about earlier gestational ages (before 30 weeks gestational age).

There is also an increased interest in infants born very preterm (less than 32 weeks of gestation) and extremely preterm (less than 28 weeks of gestation), since early birth is the main cause of infant mortality

and morbidity worldwide [25]. During the last 10 weeks of pregnancy, major changes occur in the appearance and connectivity of the fetal brain. During this relatively short period of time, the cortex develops from a lissencephalic state to a very folded one and dramatically increases in volume and surface area [73]. Following premature birth the structural development of the brain takes place outside the mother's womb, under the altered conditions of the extrauterine environment. In the harsh conditions of the intensive care unit, the brain is vulnerable to a range of insults. Hence, these infants are at higher risk of disability that may persist into their adult life. Although in the last decade mortality rates have decreased due to technological development and advances in the intensive care unit in the UK, the rates of disability in these infants remain unchanged [89]. Neuroimaging can help us understand how the brain develops during this crucial period and provide us with potential biomarkers of future disability to make interventions possible. Longitudinal studies of preterm infants are a way of predicting what happens over the preterm period. The field of preterm brain imaging is still growing, and to study these changes there is a need for software tools and methods that can cope with image processing for the early developing brain. Methods developed for adult populations or term-born infants do not usually cope with the challenging early brain.

Although there are an increasing number of studies that look at differences between extremely preterm born infants and their term peers, it is also important that these infants are followed into adolescence and adulthood to investigate the long-term effects of pretermature birth. Preterm infants studied back in 1990 are now reaching adulthood and the long term effect can now be investigated by comparing these preterm-born adults with their term-born socially matched peers [103].

1.2 Thesis contributions

The purpose of the research described in this thesis was to study the brain development over the preterm period in extremely preterm born infants, by developing advanced techniques for tissue segmentation and labelling and image registration of developmental MRI.

The contributions of this thesis include but are not limited to the following:

- A population-specific probabilistic brain atlas from T2-weighted MR images of postmortem fetuses and newborns that provides templates for automatic atlas-based segmentation of new subjects of this type. A very detailed atlas is very useful for developing biomarkers for several malformations, disease or prospective measurements of neurological function. Having such an atlas is of extreme use not only in research but also in the clinic, in order to follow the changes that take place during and after death. The resulting segmentations provide an accurate estimation of brain volumes from MRI which are comparable to conventional autopsy volumes. To the best of my knowledge, prior to this work, there was no other brain atlas existent for postmortem newborns or fetal subjects.
- A population-specific tissue probabilistic brain atlas from T1-weighted MR images of preterm born infants with two time points that provides templates for automatic atlas-based segmentation

of new subjects of this type and is essential for brain research studies of this particular population.

- The improvement of the surface spectral matching algorithm by using a Coherent Point Drift initialisation. The improved algorithm allows, for the first time, the mapping of longitudinal data of extremely preterm infants. This novel method has much potential for the assessment of the preterm brain development, and was used to look at changes in cortical folding and speculate the regions affected affected by prematurity. Furthermore, this method was also used for the groupwise shape analysis of extremely preterm born young adults and compare them with term controls, which might increase the understanding of the psychological outcome in extremely preterm individuals. Furthermore, they can provide us information on the long-term structural impact of extreme prematurity. To the best of our knowledge, this is the first study to investigate the long term impact of prematurity on the thalamic and cortical shapes. Shape analysis of brain structures is of increasing interest to the neuroimaging community, as it can locate morphological changes between healthy and pathological structures.

- A novel diffusion tensor registration method based on spectral matching of tensors, which enables us to study white matter differences in brains with very different structure. The algorithm was develop to account for global anatomical descriptors and cope with very large spatial deformations, such as complex anatomical changes during the preterm period. The proposed tensor registration pipeline represents a promising tool to investigate microstructural brain changes over the preterm period, how it is affected by preterm birth and how it might influence neurological outcome.

- A novel multi-modal registration based on spectral matching by decomposing a level set representation of the white-grey matter surface boundary (structural information) and the white matter diffusion tensors, to guide a more accurate and biologically relevant correspondence for surfaces with low gyrification. The lissencephalic brain of an early scanned preterm infant is more challenging to register cross-sectionally using regular surface registration techniques, since there is less surface information to drive the registration. The mapping enables us to study group multi-modal variations and interdependency between parameters obtained from different imaging modalities.

Algorithms and pipelines presented in this thesis were implemented in MATLAB[1], unless stated otherwise.

1.3 Thesis structure

The thesis is organised as follows: Chapter 2 is a literature review of similar neonatal work related to the thesis, how early brain development can be investigated, what its long term impact is and what tools exist to investigate it. Chapter 3 describes the three data sets (postmortem fetal data, in-vivo preterm infant data and in-vivo preterm born young adult data) used in this thesis as well as the basic image processing techniques carried out for each of them. Chapter 4 contains the segmentation processing tools and results for the postmortem fetal data. Chapter 5 describes the basic concepts of spectral graph theory. In chapter

[1] https://uk.mathworks.com/products/matlab/

6, we describe the Joint-Spectral Matching (JSM) for matching of surfaces and apply it to study the longitudinal development over the preterm period in extremely preterm born infants, by matching intra-subject surfaces that are at an early developmental stage (about 30 weeks equivalent gestational age) to a later stage at term time. In chapter 7 we then also use JSM to investigate shape differences between extremely preterm born young adults and their term born peers. In chapter 8, we propose a new diffusion tensor registration technique based on matching of spectra obtained from the decomposition of tensors (Tensor Spectral Matching - TSM). After validating our method, we apply it to the challenging problem of registering longitudinal diffusion tensor images (DTIs) of preterm infants covering a period of crucial development and investigate the white matter changes that are taking place. In chapter 9, we propose a multi-modal registration technique based on Pairing Images using Multi-Modal Spectra (PIMMS), a method that combines JSM and TSM, so that we can ensure an alignment based on both shape and microstructural information and a more accurate biological correspondence. In Chapter 10, we discuss all our results, their meaning and how they can be improved and used in the future.

Chapter 2

Background

This chapter is a review of the relevant literature and concepts that underpin the novel work presented in the subsequent chapters. In Section 2.1, we describe the early developmental stages of the brain, during the fetal and early neonatal period and more specifically, we look into the anatomical and structural changes that are taking place. Section 2.2 summarises some of the neurological findings typically associated with prematurity. Section 2.3 describes the basic concepts of MRI and the different contrasts. Section 2.4 summarises the main studies that look into early brain development, such as post-mortem fetal studies and preterm infant studies. Section 2.5 presents an overview of existing image processing and analysis techniques available for such populations.

2.1 Early brain development

Human brain development and maturation is a complex, lifelong process and one of the most fascinating aspects of the human condition [154]. The maturation of the brain begins in the second trimester (after 14 weeks of gestation) and continues progressively to reach an almost mature adult-like folding and structural pattern at around 2 years of age [57].

Brain development begins in the embryonal period and consists of changes in brain morphology and composition [57]. The changes in morphology include an increase in 1) brain volume, 2) changes in the cortical surface configuration which are caused by sulcation processes, 3) ventricular shape changes and 4) a decrease in subarachnoid spaces, all of which are usually seen in the fetal period. From mid-gestation through infancy, brain maturations includes changes in brain composition: neuronal differentiation and synapse formation (axonal and collateral formation, dendritic arborisation and spine formation, synaptogenesis and organisation of the cortical layers), glial cell differentiation and formation of myelin, programmed cell death, neurotransmitter development and vascular development [57]. Fetal cerebellar development is gradual, steady and grossly comparable to the development of entire brain, almost doubling its diameter between 19 and 37 weeks of gestation [155].

Although the brain change and adaptation is a lifelong process, these very early stages of fetal and neonatal brain development are probably the most dramatic [154]. Many neurological conditions might

depend on the course of the brain development during the first years of life, including schizophrenia, attention-deficit-hyperactivity disorder and Williams syndrome [154]. The changes are also very sudden and rapid compared to changes in an adult brain, thus monitoring all stages at high temporal resolution is of crucial importance.

2.1.1 Cortical development

The last trimester of pregnancy represents a period of rapid brain growth and shape change, a period when the brain develops from a lissenchephalic shape to one with a complex degree of folding (Figure 2.1). In this period, the cortex develops several secondary and tertiary gyri and sulci in all its lobes.

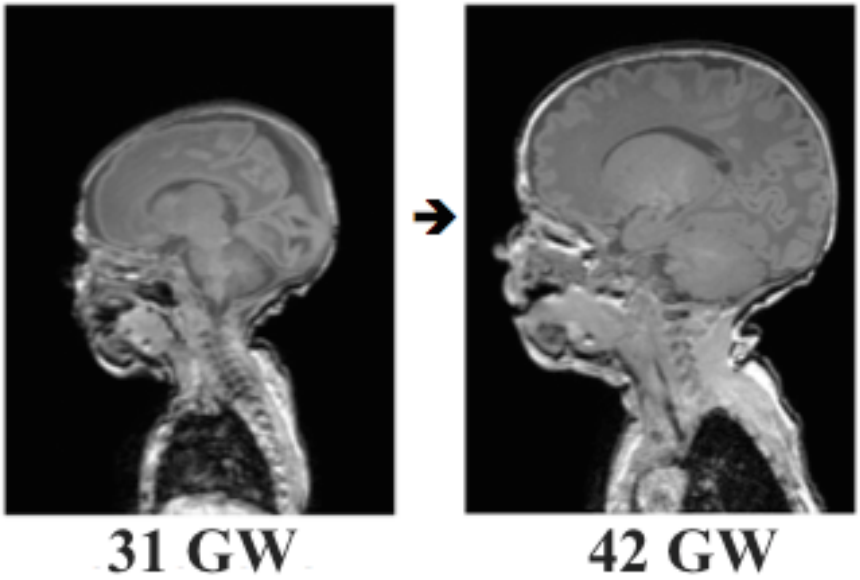

Figure 2.1: Example of a T1-weighted MRI of an extremely preterm born infant, scanned twice: once shortly after birth and once around term time.

The prefrontal cortex (PFC) is situated in the anterior part of the frontal lobes of the brain, inferior to the motor and premotor areas. This neocortical region is thought to play an important role in cognitive control, executive function and habituation [100]. Because of its anatomical connections with the cortical and subcortical centres, important for movement control, the PFC plays a role in coordinating motor function. Thus, accurate measurements in this region, in particular its volume and shape change, might be predictive of early delays in motor control. The superior frontal gyrus of the PFC becomes defined by 25 gestational weeks (GW) [33]. The inferior frontal sulcus is visible by 28 GW, followed by the delineation of the middle and inferior gyri [33]. All three main regions show secondary gyri at about 32 GW, while tertiary gyri are distinctive by 40 GW [33].

The temporal lobe plays a crucial role in the formation of explicit long-term memory and appears to be an area of increased vulnerability in the fetal brain since abnormalities in its morphology may contribute to learning difficulties [75]. Most of the temporal lobe development takes place after 30 weeks of gestation. By this time, the middle temporal and inferior temporal gyrus can be distinguished, while the superior

Table 2.1: Regional Development of Sulci and Gyri for the Last Trimester of Pregnancy (gestational weeks) [33]

Lobe	Weeks	Sulci and fissures	Gyri
Frontal	25	Superior frontal	Superior frontal gyrus
	27		Middle frontal gyrus
	28	Inferior frontal	Triangular gyrus, callosomarginal gyrus, medial and lateral orbital gyrus
	36		**Anterior and posterior orbital gyrus**
Temporal	26	Middle temporal sulcus	Middle temporal gyrus
	27		Fusiform gyrus
	30	**Interior temporal sulcus**	**Inferior temporal gyrus, external occipitotemporal gyrus**
	31		**Transverse temporal gyrus**
Occipital	27	Lateral occipital sulcus	Superior and inferior occipital gyri, cuneus, lingual gyrus
	30		**External occipitotemporal gyrus**
Parietal	25	Postrolandic sulcus	Postrolandic gyrus
	26	Interparietal sulcus	Superior and inferior parietal gyri
	28		Angular and supramarginal gyri
	35		**Paracentral gyri**

temporal gyrus begins to be recognisable from about 23 weeks of gestation [33]. A right-left asymmetry can be noticed in the temporal lobe since the right transverse temporal gyrus develops at approximately 31 GW, while the left transverse temporal gyrus develops one or two weeks later [33]. The secondary sulci of the superior temporal gyri are visible at 34 to 35 GW, while the secondary gyri of the transverse temporal gyrus appear after 36 GW [33].

The parietal lobe plays an important role for sensory integration and visual attention [64] and the occipital lobe is the visual processing center of the human brain, containing most of the visual cortex [162]. These two lobes have a different time frame of development and the gyri and sulci corresponding to these regions develop before 28 weeks of gestation [33], thus they should not be as affected by preterm birth as the prefrontal cortex and temporal lobe.

The human brain develops significantly during the last trimester of pregnancy (See Table 2.1). The development of the prefrontal cortex, as well as the temporal lobe, takes place mostly during this time period, later than the parietal and occipital cortices, making it possible to study their development in more detail using longitudinal data of infants aged between 30 and 40 weeks equivalent gestational age. Due to the developmental timing, both these regions may be more affected by preterm birth and thus finding feasible biomarkers (characteristics by which a particular pathology or disease can be identified) to predict future impairment is of great interest.

2.1.2 Structural and microstructural changes

From a microstructural point of view, the organisation and structure inside the brain also changes a lot during early development (Figure 2.2). The brain has two main components: white matter (WM) and grey matter (GM).

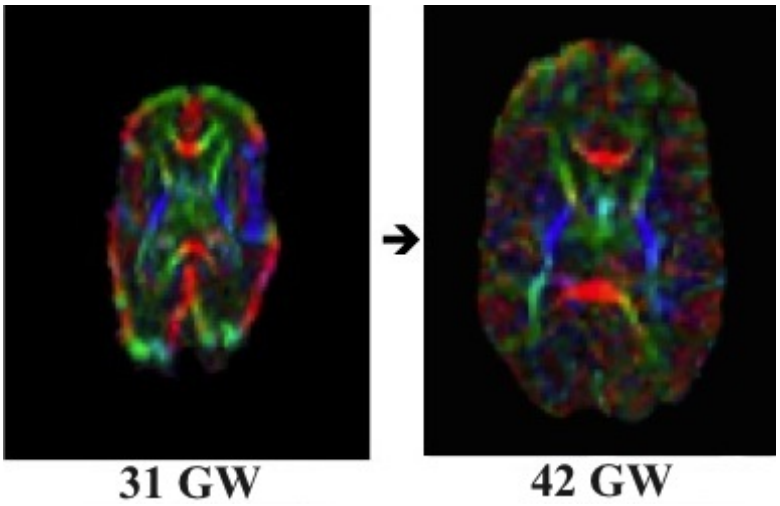

Figure 2.2: Example of longitudinal changes in microstructure, observed from the coloured fractional anisotropy maps of diffusion-weighted MRI, in an extremely preterm born infant, scanned twice: once shortly after birth and once around term time.

White matter is an important part of the brain, making about half of of the human brain. Its main role is acting as an electrical conductor of neural signalling, being essential to the development of human behaviour [78]. WM is composed of bundles of nerve cells or axons, which are long, myelinated and connect the different grey matter regions of the brain [52]. Myelin is the insulating lipid-layer wrapped around the axons of the WM and has an essential role in conducting impulses [46]. Another important component of the WM are the glial cells, which are responsible for maintaing myelin [46].

Grey matter, also a major component of the brain, consists mainly of neurons [52]. It can be found at the surface at the brain, known as cortical grey matter or cortex, as well as in the depths of the cerebrum, such as the thalamus, cerebellum and brainstem.

The maturation and development of WM is a prolonged process and development of different WM characteristics, such as the connectivity changes during different stages of life, are not entirely clear [78]. It is known that WM experiences rapid changes over the fetal period and during infancy [10] and its progressive organisation has been previously established from post-mortem studies. The neurons migrate and once in their final localisation, they develop with other neurons at both ends: a dendritic tree within the grey matter and axon formation running through the white matter [45]. Macroscopically, over the second half of pregnancy, the axons form bundles through a variety of processes such as neuronal and synaptic overproduction, cellular apoptosis, axonal retraction and synaptic pruning [45]. Establishing the timing of these processes and the of the neuron migration is essential for defining the cerebral organisation for

the cortex and the WM.

Furthermore, the organisation of WM, maturation and efficiency of the fibre connections is influenced by the myelination process, which favours the transmission nervous impulse conduction, optimising for velocity [45]. At a microscopic level, myelination causes changes in water molecule content and compartmentalisation and changes in lipid and protein content [45]. Myelination is the last stage of WM development and starts from the last trimester of pregnancy and continues until early adulthood, with its peak in the first postnatal year [46]. In the developing white matter, processes leading to myelination evolve in an organised spatial pattern, ascending into the corticospinal tracts starting around 30 weeks of gestation and evolving from this brain region into the anterior and posterior regions over the first months after birth [24].

Cortical maturation is considered to be associated with a dendritic arborisation and formation of synapses which increases from midgestation. Starting with midgestation, the neurons migrate from the subventricular region to the cortex by radial migration [94]. During this period, the radial formation arranged perpendicular to the cortical surface becomes a denser, complex structure with larger numbers of neural connections, which are parallel to the cortical surface [11]. It is also hypothesised that the increase in cellular complexity and density leads to a decrease in the tissue water content [11].

2.2 Impact of extreme prematurity on brain development

Premature birth implies that part of the structural development of the brain will take place under the altered conditions of the extrauterine environment rather then inside the mother's womb. Infants that were born extremely preterm are at a higher risk of developing cognitive and neurologic impairment, despite advances in neonatal intensive care [89]. During the last 10 weeks of pregnancy, major changes occur in the appearance and connectivity of the fetal brain. During this relatively short period of time, the cortex develops from lissencephalic to very folded and dramatically increases in volume and surface area [73].

Initially, most studies describing the outcome of prematurity were based on birth weight, thus associating the effects of extreme prematurity with those of intrauterine growth restriction [6]. Other studies looked into the effects of intrauterine or postnatal infections on premature birth and infant neurodevelopment [55], [31]. However, the prognosis of extremely preterm infants require reliable information based on gestational age and structural development, so that adequate treatment can be planned [165]. Because of this, there was a need of recruiting preterm cohorts for research purposes, with some known ones being the EPICure study of extreme prematurity (http://www.epicure.ac.uk/) and the Bavarian Longitudinal Study of very preterm infants [164].

Disability is common among surviving extremely premature subjects [165]. Studies have looked into the outcome of premature born subjects, finding an increased prevalence of cognitive impairment and poorer educational achievement in these subjects when compared to their term born peers. Significant developmental delay or learning difficulties have been found from the IQ analysis of very preterm or

very-low-birthweight infants [9]. Wood et al. (2000) found disabilities in mental and psychomotor development, neuromotor function, or sensory and communication function at 30 months corrected age in about 50% of the survivors of the EPICure cohort [165]. Marlow et al. (2005) found that cognitive impairment was prevalent among the EPICure extremely preterm children when compared to their classmates at age 6 [89]. Preterm children aged 6 from the Bavarian longitudinal study also scored significantly lower on measures of cognitive and language abilities, including general intelligence, language comprehension, expression, articulation and prereading skills when compared to their term peers [164]. These subjects were later more frequently diagnosed with attention-deficit-hyperactivity-disorder (ADHD) as they presented more attention problems and shorter attention span [20]

There are also sex differences in the preterm populations, with preterm males exhibiting higher rates of neonatal mortality and long-term morbidity [50]. Several gender differences have been identified in respiratory and circulatory parameters during the first days of life in very preterm individuals; males need to receive more care and be intubated faster than females [50]. It is also well-known that preterm males are more likely to experience neurological and developmental disabilities than preterm-born females [65], [89].

It seems clear that extreme prematurity has an impact on brain development, causing a delay in its development and leading frequently to neurological and cognitive impairment. However, the nature of the cerebral abnormalities that cause these common and serious developmental disabilities are not yet completely understood [70]. Researching how the brain develops in extremely preterm infants after birth will aid the understanding of these brain abnormalities and may enable the finding of feasible biomarkers to predict this future impairment and develop better treatments for this population. Developing computational tools to investigate development is thus crucial.

2.3 Overview of Magnetic Resonance Imaging (MRI)

Magnetic Resonance Imaging (MRI) is an advanced medical imaging method based mainly on the sensitivity to the presence and properties of water, which makes up about 70% to 90% of most body tissues [91]. MR imaging has evolved over the last 50 years and it is used widely for research and as a diagnostic technique, detecting subtle changes in the magnetism of the nucleus [91].

A variety of MR images are acquired and used. The most common ones are T1-weighted images, also known as 'anatomical scans', having excellent tissue contrast [91]. T2-weighted images also offer a good tissue contrast and are known as 'pathological scans' with abnormal fluid appearing brighter against the darker normal tissue types [91]. These scans are suitable for studying the anatomy, such as changes in volumes, surface areas, cortical folding, cortical thickness and myelination. The difference between T1- and T2-weighted scans is that they measure different relaxation times: hydrogen atoms in each tissue return to their equilibrium state after being excited by independent processes of T1 (spin-lattice) and T2 (spin-spin) relaxation [91]. T1-weighted images are created by allowing magnetisation to recover before measuring the MR signal, by changing the repetition time (TR) [91]. For T2-weighted images,

the magnetisation is allowed to decay before measuring the MR signal, by changing the echo time (TE) [91].

Diffusion weighted magnetic resonance imaging (DW-MRI) is a water diffusion imaging technique that provides insight into the white matter organisation of the human brain [175]. Depending on the local conditions, water can diffuse in different ways, so one needs to fit models to the diffusion signal in order to infer information about the microstructure. Several models have been developed for this purpose, with some popular ones being the diffusion tensor (DT) [12] and Neurite Orientation Dispersion and Density Imaging model (NODDI) [174].

DTI models the diffusion as ellipsoidal, with highly oblate ellipsoids or tensors in homogeneous regions such as the white matter and more sphere-like tensors in the cerebrospinal fluid [12]. The properties of the tensors are summarised through measures like the fractional anisotropy (FA) - how isotropic the distribution is (see example of FA maps in Figure 2.2), and mean diffusivity (MD) - average diffusivity of the tensor [12]. Despite the popularity of DTI, more complex models of the diffusion signal can give more insight into the morphology of neurites (dendrites and axons) and thus the brain structure [174]. An example is NODDI, which is a multi-compartment microstructural model for diffusion data [174]. NODDI divides the diffusion signal coming from different compartments with volume fractions of v_{iso} - for the isotropic compartment, v_i - for the intra-neurite space, and v_e - for the extra-neurite compartment, and has been previously applied to a cohort of extremely preterm neonates [49].

2.4 Imaging of the early brain using MRI

Brain development can now be examined in detail using imaging. MRI is currently the method of choice to evaluate brain maturation, since it is non-invasive, uses non-ionising radiation, safe and provides good quality images of soft tissue. In the late 90s, an MRI scanner specifically designed for neonates was set up, with shorter acquisition time than in adults [153]. As a result, brain MRI in neonates has spread widely during the last decade, thanks to the development of the technology, such as improvement in the hardware (faster and quieter MR acquisition and MR-compatible neonate incubators) and specifically designed software to process the neonatal brain data. Although an ultrasonography scan is still the most rapid and preferred imaging technique, especially in the case of evaluating the health of an early fetus in the womb, MRI provides better soft tissue contrast and thus improved anatomical details. It also provides an accurate depiction of morphological and signal changes of normal brain development and of its disorders [57]. MRI is thus the preferred imaging technique in brain development research.

Monitoring brain development during the fetal and early neonatal periods can be done by studying three main subject cohorts: 1) in vivo studies of fetuses; 2) post-mortem studies of fetuses; 3) extremely preterm and preterm born neonates.

In vivo studies of fetuses are probably the ideal way of studying normal brain since this development takes place under normal conditions, inside the mother's womb. Hence, imaging fetuses provides an unique opportunity for the *in vivo* investigation of the human brain development at this very early stages,

development which is still not understood. For the developing fetus, ultrasound is usually the modality of choice for evaluation. However, ultrasound has very low soft tissue contrast and MRI can provide a better alternative with better contrast [131]. Fetal MRI is usually challenging because of motion artefacts and difficulty in optimally positioning the coils. Most in-vivo fetal studies will acquire 2D MRI images and reconstruct 3D volumes, which can sometimes be a lengthy and not straightforward process. Although fetal ultrasound is still the preferred modality, being the cheap and real-time imagining technique in clinical practice, fetal MRI does have its advantages for research and diagnosis, having superior contrast and field of view [26]. Fetal MRI can be used to provide a more detailed insight into fetal anatomy and development [23], however the main issue that still remains is that of fetal motion.

Post-mortem studies of fetuses are another way of investigating brain development, which can be considered normal if the cause of death was not brain related. However, it is usually difficult to segment tissue types of the postmortem brain because of the small differences in T1-weighted postmortem contrast in grey and white matter.

Studies of extremely preterm and preterm infants are also one option for studying normal brain development, in the case where no major brain abnormalities are present. In the case of these infants, however, normal development of the brain is disrupted by their early birth, and the development has to take place outside the mother's womb.

2.4.1 Post-mortem Fetal MRI

Fetal deaths, involuntary losses of fetuses during pregnancy, outnumber infant deaths [66]. The risk of fetal loss can be due to both maternal and fetal characteristics, and cause of fetal death can provide additional insight into the reason. The majority of fetal deaths occur early in pregnancy and in most cases reported (29.7%), the cause is unspecified, as stated in a fetal date report from 2014 in the US [66]. In 28.4% of the cases from the same report, the reason for death was that the fetus was affected by complications of placenta, cord and/or membranes, while in 14.2% the reason was maternal complications [66]. Congenital malformations, deformations and chromosomal abnormalities were the cause in only 10.2%, and in 7.8% of the cases, the fetus is affected by maternal conditions unrelated to present pregnancies [66].

The loss of a fetus, a baby or a child is traumatising and devastating for a parent. Knowing the exact reason why their child died and if there is any risk for further pregnancies or existing children is comforting and can help parents cope with their loss. Performing autopsy is important for establishing the cause of death and for progress in medicine and research. In about 14-46% of perinatal and infant postmortem examinations, information is found beyond what was known prior to the examination, affecting the counselling and estimate of recurrence risk [151]. Many studies have previously shown that there is low concordance between the pre-mortem and post-mortem diagnosis ([118], [38]), showing the need for autopsies to be performed. Over the past decade, the consent rate for autopsy in newborns has been less than 20% and in stillborns less than 50% in the United Kingdom [30]. The main reasons of parental

refusal are religion, the invasive nature of the autopsy and delays to the funeral. The usual brain autopsy practice consists of the removal and fixation of the brain before dissection, a process that can take up to three weeks [151]. Even when adequately fixated, the high water content of the immature brain makes its handling difficult [68]. Parents usually request that all organs are replaced before the funeral, which means that the brain tissue has to be examined following a suboptimal fixation period, making the detailed structural analysis of the developing brain even more challenging [68].

MRI is a powerful tool that can be used as a post-mortem imaging technique with high accuracy and high level of performance for depicting soft-tissue lesions [130]. MRI has proved to be a credible alternative to invasive autopsy mostly in the case of non-suspicious death, with a diagnosis agreement of 87%. Griffiths et al. (2003) examined the neuropathology in fetuses and deceased neonates and found a good agreement of the reasons leading to death between MRI and autopsy in 28 out of 32 cases, concluding that MR provides detailed information about all organ systems, except the heart [60]. Cohen et al. (2007) also found a good correlation for detecting brain and spine anomalies, but concluded that it should be combined with autopsy results in most cases for a precise result [36]. Breeze et al. (2006) determined kappa values (statistical measures of inter-rater agreement) in order to assess agreement between autopsy and MRI for different organs and found a very high value for the brain (0.83) [21].

Thayyil et al. (2013) suggested the need for a minimally invasive autopsy procedure, using MRI coupled with blood sampling via needle puncture [150]. To the best of our knowledge, this research presents the most extensive database up to now, containing over 400 post-mortem T1, T2 and/or diffusion MRI scans of fetuses and newborns[150]. Specialists in nervous, cardiovascular, pulmonary and abdominal fields were summoned to study the MRI results for a diagnosis of the cause of death in 400 cases, which was also established from conventional autopsy. The agreement between the minimally invasive autopsy and conventional autopsy was of 89.3%, whilst using MRI alone had an agreement of 55.5%.

2.4.2 MRI of extreme prematurity

2.4.2.1 Prematurity in infants

Recently, there has been much interest in understanding changes in altered brain development during the preterm period [160]. Changes in brain volume and cortical folding can be investigated from conventional MRI such as T1- and T2-weighted images. Kapellou et al. (2006) analysed the brain growth of the preterm brain from 113 infants, scanned between 23 to 48 weeks of gestation, and found that cortical surface area was related to the volume growth by a scaling law with an exponent of 1.29 [73]. Furthermore, they found that increasing prematurity and the male gender were associated with a lower scaling exponent [73]. Xue et al. (2007) found the same surface area and volume growth scaling ratio of approximately 1.29 in 25 preterm neonates scanned between 27 and 45 weeks, as well as an overall increase in cortical thickness [169]. Boardman et al. (2010) identified a common phenotype in 66 out of 80 preterm infants scanned at term equivalent age, consisting of diffuse white matter injury and focal tissue loss localised in several brain regions [18]. Ball et al. (2012) acquired T1-, T2-weighted and

diffusion MRI from 71 preterm infants scanned at term equivalent age and combined deformation-based morphometry, Tract-Based Spatial Statistics and tissue segmentation to study the effect of prematurity on regional tissue volume and microstructure [10]. After controlling for prematurity, they concluded that reduced volume of the thalamus implied lower cortical volume and decreased volume in the frontal and temporal lobes. Ball et al. (2012) concluded that prematurity significantly affects the development of the thalamus, related to abnormalities in other brain structures [10]. Melbourne et al. (2014) scanned 92 infants at term equivalent age and demonstrated that the cortical sulcation ratio and fractional anisotropy of local white matter regions are significantly correlated with the gestational age at birth in these infants [95]. Furthermore, they found that the cortical sulcation ratio varies spatially over the cortical surface, while the fractional anisotropy of white matter regions varies according to location; connectivity measurements from tractography were shown to be correlated significantly and specifically with the sulcation ratio of the overlying cortical surface at term equivalent age in a subgroup of 20 infants. Moeskops et al. (2015) investigated the cortical development in a cohort of 85 preterm infants scanned at 30 and 40 weeks postmenstrual age, by looking at the longitudinal global changes such as volume, surface area, global mean curvature, thickness and gyrification index [102]. They proved that there were larger global changes in the occipital lobes and that the gyrification index and global mean curvature decrease with abnormality score, while thickness increases.

Developmental changes at the cellular level such as neural afferents and radial migration of the neurons cannot be observed using conventional structural MRI yet diffusion weighted MRI (DW-MRI) can be used instead. DTI parameters may allow us to observe and quantify developmental changes during the preterm period, providing additional information about the microstructural change of brain structures, information that cannot be revealed by T1-weighted or T2-weighted MR images [69]. DTI parameters seem to have the same developmental patterns [46]: fractional anisotropy (FA) increases in the perinatal period in white matter regions [124], related to a general increase in complexity [11]. DTI measures were correlated with disabilities associated with preterm birth [99].

NODDI parameters were also used to investigate changes over the preterm period in grey matter, in the cortex and thalamus [49]. Increased Orientation Dispersion Index, increased v_i and a decrease in v_{iso} were found over the preterm period in the grey matter, associated with the myelination process and major changes in microstructure [49]. Furthermore, water diffusion measures could be correlated with the cortical changes that take place during this period, since tension along axons in white matter is one of the hypotheses for cortical folding [156].

These developmental changes observed from MRI have also been correlated with the neurological outcome of extremely and very preterm infants. Abnormal gyrification patterns, such as increased temporal lobe gyrification, have been identified in preterm children and have been associated with cognitive-behavioural deficits among subjects with developmental language disorder, autism or dyslexia [75]. Volume reduction in the cortical and deep nuclear grey matter at term equivalent age were shown to be an indicator for disability at 1 year of age in premature subjects [70].

All these mentioned studies demonstrate that preterm birth has a large impact on cortical development and on the structural and microstructural changes and affect the neurological outcome of the infants. However, it is not known exactly how gyrification or microstructure in the preterm brain changes over time [75] and accurate measurements of the brain during this early post-natal period may yield predictive biomarkers of neurological outcome [18].

2.4.2.2 The long term effects of prematurity

Although there is an increasing number of studies that look at differences between extremely preterm born infants and their term peers, not as many studies follow these infants into adolescence and adulthood and investigate the long term impact of preterm birth. There are studies looking into the differences in function between preterm and term children, adolescents and adults, that found that preterm cohorts perform worse their term peers [89].

Fraello et al. (2011) evaluated 49 preterm and 20 term subjects, all aged 12, using both neuropsychological measures and MRI and concluded that there is evidence of learning difficulties in former preterm infants [54]. Dingwall et al. (2016) compared brain volumes and T2 values between a cohort of 46 extremely preterm adolescents and 20 adolescent controls, finding a volume deficit in the preterm group, as well as a volume deficit in preterm males when compared to preterm females [43]. Several studies investigate neuroanatomical changes in extremely preterm born adolescents, like volumes of different structures, and their correlation to cognitive performance. Gimenez et al. (2006) used voxel-based morphometry (VBM) and investigated white matter (WM) region abnormalities by comparing 50 adolescents born preterm and 50 matched subjects born at term. The study identifies periventricular damage and a WM decrease in regions distant from the ventricular system, usually located at the beginning and end of long fascicles. Low WM integrity was significantly correlated with low gestational age at birth[56]. Soria-Pastor et al. (2008) studied 44 adolescents born before 32 weeks of gestation and 43 term-born adolescents, and concluded that the performance intelligence quotient correlated with the whole-brain white matter volume, but not with the grey matter volume [142]. Nosarti et al. (2008) also used VBM to investigate the distribution of white (WM) and grey matter (GM) in very preterm born adolescents compared to term born controls and found regions of reduced WM (brainstem, internal capsules, temporal and frontal lobes) and GM (temporal, frontal and occipital lobes, cerebellum, thalamus, insula), as well as regions of WM excess (temporal, parietal and frontal lobes) and GM excess (temporal and frontal lobes) [106]. The very preterm born subjects also obtained lower scores than controls on measures of language and executive function, and several areas of WM and GM decrease were linearly associated with gestational age at birth and cognitive impairment [106] .

2.5 Image processing techniques for early developmental data

2.5.1 Probabilistic atlases and tissue segmentation

Neuroanatomy requires anatomical atlases, that allow an accurate reference space for comparison within different studies [90]. One of the most important tools in the field of computational anatomy is the probabilistic atlas. However, these atlases cannot assume a single, constant reality. Initially, atlases of the human brain and other species have been derived from a single brain, or brains from a very small number of subjects, and used simple scaling factors in order to match another subject's brain with the atlas [90]. The result is rigid, often inaccurate and not aligned, since it disregards the variability between subjects. Anatomical atlases must deal with the fact that there are infinite numbers of physical realities that must be modelled to obtain an accurate, probabilistic representation of the entire population [90].

An age-specific atlas of the human brain can provide important insight into the variability between ages in a population and into development and maturation of the brain. Compared to the adult brain, fetal and preterm brains show a rapid growth over a short period of time and an atlas needs to cover the complexity of this abrupt development. Another role of probabilistic atlases is to use them as anatomical priors for tissue brain segmentation methods.

Probabilistic atlases for neonatal brain development have already been created and their application to tissue segmentation has been investigated. Knickmeyer et al. (2008) has developed a three-class (grey matter, white matter and cerebrospinal fluid) atlas based segmentation approach from birth to 2 years of age, analysing the changes among the population [77]. Habas et al. (2009) created a spatio-temporal atlas for the fetal brain between 20 and 24 gestational weeks of 10 fetal subjects with normal brain development [61]. Oishi et al. (2011) used the diffusion-weighted data to produce a multi-contrast neonatal brain atlas [107]. Kuklisova-Murgasova et al. (2011) created a publicly available and comprehensive probabilistic atlas covering the third trimester of pregnancy (29 to 44 gestational weeks) using 142 neonate subjects [79]. The atlas was generated from T2-weighted data with intensity classes for grey matter, white matter and cerebrospinal fluid, with spatial subclasses for sub-cortical grey mater, cerebellum and brainstem. Serag et al. (2012) also created a probabilistic atlas for 80 fetuses and neonates (23 to 37 GW), from T1 and T2-weighted data, representing the white matter, cortex, CSF and deep grey mater [135]. Schuh et al. (2014) proposed a diffeomorphic registration for atlas construction for neonates, which uses the Log-Euclidean mean of inverse consistent transformations to equally deform both images being registered, representing an average morphology [134].

Statistical maps can also be created to assess group effects like the differences between brain structures of healthy children and children with neuropsychiatric disorders like schizophrenia, bipolar illness, attention-deficit-hyperactivity disorder (ADHD) or genetic disorders like Williams syndrome [154]. Studying specific cohorts can give insight into certain pathologies.

Regions of interest in the brain such as the white matter and grey matter can be identified by means of

tissue segmentation. Tissue segmentation methods of MR images usually take into account the image intensity of different classes. In the case of the developing brain, automatic segmentation routines developed for the adult control population do not capture the poor contrast, low resolution and partial volume effects in the data. Several authors have proposed segmentation techniques specifically developed for the neonatal population, mainly by adapting well-known techniques in the adult brain. Prastawa et al. (2005) proposed a technique based on an expectation-maximisation process (EM) [157], but modelling additional white matter classes to account for myelination and tested it for normal subjects [127]. Anbeek et al. (2008) proposed a method based on a K nearest neighbour (KNN) classification techniques to segment the normal neonatal brain into four tissue classes: white matter, central grey matter, cortical grey matter and cerebrospinal fluid [5]. Xue et al. (2007) developed a neonatal segmentation specifically designed for the segmentation of the cortex by combining the brain extraction technique with grey matter structure removal, which was also applied to normal neonate subjects [169]. They brought up the issue of the mislabelled voxels due to partial volume effect (PVE) [169]. However, these neonate algorithms proposed above ([127], [5], [169]) do not take into consideration any tissue priors or subjects with abnormalities, like neonates born preterm or neonates with ventriculomegaly etc.

More complex and accurate tissue segmentation algorithms for the preterm population are initialised with anatomical tissue priors from already existing atlases of similar populations. Song et al. (2010) proposed a simple intensity based classification method using Gaussian mixture models. [141] and Yu et al. (2010) suggested a Parzen window based on a Markov random field algorithm, optimised by an Expectation-Maximisation (EM) process [172], both initialised by a population atlas. Cardoso and Melbourne et al. (2013) proposed an adaptive multi-modal maximum *a posteriori* EM segmentation algorithm (AdaPT) with prior relaxation, in which an intensity non-uniformity correction and a Markov random field for spatial homogeneity term are included [28]. This method was specifically developed and successfully applied for the segmentation of the preterm infant brain, including ventriculomegaly cases.

2.5.2 Infant brain registration

Image registration is an important image processing tool which defines a mapping between coordinates from one space to another, to achieve biological, anatomical or functional correspondence. Longitudinal changes over a time period can be investigated using a series of brain images of the same subject scanned at different time points. The spatial registration of this time series (longitudinal registration) provides us with a spatial transformation that describes the anatomical changes taking place over the time period.

Registration is also needed to define a groupwise space in which we can study parameter changes, hence for the registration of similar subjects, scanned at similar time points. Most popular registration techniques are either voxel-based or surface-based. While voxel-based techniques have been widely used for atlas creation (see Section 2.5.1), surface-based techniques are sometimes preferred when studying changes in folding patterns or morphology, since it offers a clearer view of the morphology of inter-

est.

2.5.2.1 Surface registration

Surface registration is often preferred over image registration to align cortical areas. To investigate folding and local cortical differences we need to examine the cortical surfaces of the subjects by using surface meshes. These meshes can be obtained from the binary segmentations of any tissue class or structure. In order to study the local cortical differences at different time points or between different subjects we need to have a spatially smooth and accurate correspondence has to be defined between the cortical surfaces. Matching of cortical surfaces is a challenging process and non-linear registration methods only take into account local deformations. In the case of the longitudinal cross-sectional preterm data, the surfaces have very different levels of folding, and we need a method that will consider the global changes that take place.

Most methods of cortical surface alignment are based on either optimising flows, such as Large Deformation Diffeomorphic Metric Mapping (LDDMM) [15], or require some surface preprocessing to produce a 2D parametrisation. The advantage of the latter is that we can obtain a more robust and smooth correspondence and reduce computation time. Van Essen and Drury (1997) made a series of surface cuts to reduce distortion before warping flat cortical maps to one another [156]. Other approaches are based on inflating surfaces such as FreeSurfer [53], Spherical Demons [170] or multi-modal surface matching [129]. By using inflation, a surface can become a sphere while minimising geometric distortion. Hence surfaces can be treated as 2D spherical images with scalar information defined at each vertex (e.g. sulcal depth) to guide registration. The disadvantage of these methods is that they are usually computationally expensive, because of the inflation step.

Spectral graph theory offers a fast alternative by matching shapes in the spectral domain (See Chapter 5), where two near-isometric shapes, with identical geodesic distances between points, have identical spectral representations [85], [139]. Spectral graph theory uses eigenvalues and eigenvectors of the graph Laplacian matrix. These eigenvalues can be interpreted as natural oscillating frequencies of a physical shape. The eigenvectors, each associated with one eigenvalue, represent normal modes of the shape or eigenmodes. A surface can then be matched in the spectral domain by matching its spectral coordinates or eigenmodes.

Lombaert et al. (2013) [87], proposed a spectral matching method for surface mapping in which a preliminary point correspondence is defined from the spectral representation of the surfaces [85] and additional information like sulcal depth, followed by the construction of a dual-layered graph, which links corresponding vertices across the two graphs. The final spectral decomposition of the dual-layered graph gives an orthonormal basis where accurate correspondences can be established between two surfaces. This method gives registration results comparable with those from FreeSurfer [53] and Spherical Demons [170] and has a considerable speed advantage. Furthermore, in the case of atlas construction, spectral methods provide more consistent results when different templates for the alignment were

used.

This methodology was successfully adapted and used to analyse cortical development over the preterm period [115], [109] (see Chapter 6 of this thesis) and for the construction of a spatio-temporal surface atlas of the developing cortex from 80 healthy fetuses with gestational age between 21.7 and 38.9 weeks [167]. This method thus represents a promising tool for matching shapes with different levels of folding, but similar representations in the spectral domain.

Another way of registering surface information is through the matching of the level set representation of the surfaces. Vemuri et al. (2003) proposed an image registration technique based on a novel curve evolution approach in the level-set framework, that was computationally very fast, could cope with small and very large deformations and provided a unique solution for the intensity evolution model [158]. Dedner et al. (2007) established a correspondence between level set representations by finding a displacement field that minimised the sum of squared difference between the level set function values and their mean curvatures [42]. Level-set registration could replace surface registration if one needs to define a correspondence in the image space.

2.5.2.2 Tensor registration

For an accurate study of longitudinal changes in the white matter during the preterm period, we need a spatial transformation that defines the voxel-wise correspondence between the diffusion weighted images at different time points, which can be done by means of diffusion tensor registration. Registration of diffusion tensor images is challenging because of both the multi-dimensionality of the data and the fact that one must ensure that the tensor orientation is consistent with the anatomy after the registration ([2]). Several diffusion tensor image registration techniques have been proposed based on different matching criteria, and can be divided into two main groups.

The first group of algorithms uses scalar information derived from diffusion tensor images to drive classic image registration frameworks (affine registration of fractional anisotropy maps or non-linear registration like the diffeomorphic demons ([159])). This group of algorithms is the most commonly used due to its easy implementation, however it does not take into account the tensor orientation, i.e. the multi-dimensionality of diffusion data.

The second group of algorithms optimises specific tensor image features and account for tensor orientation through the Preservation of their Principal Directions (PPD) within a diffeomorphic registration framework ([2], [27]) or by explicit optimisation of a transformation based on tensor similarity using the Finite Strain reorientation strategy ([175], [171]).

In the case of scalar images, the registration is usually based on minimising the sum of squares difference similarity between two images at each given point. Similarly, in the case of diffusion tensor registration, one can define and minimise a tensor similarity metric. For example, several authors ([171], [145]) proposed the use of the log-Euclidean similarity metric as introduced by [7] in a diffeomorphic demons registration framework.

Spatial correspondence in standard non-linear registration algorithms is usually defined in order to optimise the similarity between *local* image features. However, when there are complex anatomical changes such as during the preterm period, an algorithm to cope with the very large spatial deformations is needed to provide a reliable description of the underlying growth. For this purpose, we require a registration algorithm accounting for *global* anatomical descriptors, as provided, for example, by the Laplacian eigenmodes associated with an image.

2.5.2.3 Multimodal registration

Folding-based surface registration is, however, limited. Firstly, it is based on matching surface patterns, like gyri and sulci, but there are several regions of wide inter-subject variability even in the control group, where an appropriate mapping is not possible. Secondly, there is a variable and complex relationship between functional areas and cortical folding patterns and matching cortical folds do not always match the underlying microstructure or function [88]. Because of this, registration of cortical surfaces could be improved by using additional information, such as microstructure or functional data, to drive the alignment. However in some cases it is not guaranteed that additional information could aid the registration process. For example, a functional alignment does not necessarily match the alignment of anatomical or shape information, and one needs to decide which of them is more important for the alignment and the further analysis.

Micro-architectural features of the cortex, such as density, size, shape and orientation of myelin sheaths can be used as additional information for driving surface registration since they are strongly correlated with cortical function [4]. Recent studies have mapped individual and group average T1 maps [14], [136], T2* maps [37] and T1-weighted/T2-weighted ratios [58] onto cortical surfaces. These measures have been shown to be a representation of functional locations of specialised areas on the cortex using functional MRI mapping [136]. Tardif et al.(2015) then proposed to use T1 maps, an indicator of myelination, to drive surface registration (MMSR) [88].

Other registration techniques have also been proposed that use brain functions derived from functional MRI surface alignment. Sabuncu et al. (2010) used correlations of the functional response to a movie-watching task to guide the alignment of brain regions [133]. Conroy et al. (2013) similarly proposed the alignment of global functional connectivity matrices [39]. Both of these methods, however, need a folding based alignment as initialisation and including information from other MRI modalities can improve this. Robinson et al. (2014) proposed a Multimodal Surface Matching (MSM) using a discrete Markov Random Field (MRF) registration method of surface alignment. The surface alignment is based on univariate multimodal descriptors of surface curvature and myelination, and multivariate feature sets derived from resting state fMRI [129].

Multimodal registration of surfaces can be extremely useful when dealing with early preterm data, especially for lissencephalic brains to drive a folding-based surface registration, but it also requires the acquisition of more types of MRI. fMRI is not usually acquired for preterm infants. Furthermore, T1

maps or the T1-weighted/T2-weighted might be inappropriate to use for the young cortex which is still undergoing myelination, so different subjects will have different levels of myelination. Other modalities like diffusion weighted MRI are an appealing alternative to use for multi-modal registration.

2.6 Summary

The field of neonatal preterm imaging is growing in popularity, since it contributes information to early brain development and pathological processes. However, there is still much to be developed in terms of specific MR scanners, coils and image processing methods to accurately investigate the brain development in this population. Popular tools that have been used for the adult or child population may face difficulty with the neonatal data, where there are rapid changes in size, shape, contrast, folding and structure. Hence, there is a need for tools specifically developed to investigate this population, such as image and surface registration and tissue segmentation.

Furthermore, because of the difficulty of acquiring MRI data at multiple time points for infants born very or extremely preterm because of the fragility of the infant, there are not many longitudinal studies of these infants. There is still a lot of unknown information about how the human brain develops especially in the early life stages. Studying data from preterm infants could answer clinical questions and questions regarding human ontogeny.

Chapter 3

Data and Image Preprocessing

This chapter describes the three data sets used for the project: the post-mortem fetal cohort (Section 3.1), used for designing the segmentation pipeline since it is a similar cohort to the preterm infant one, with brains that are not fully developed, so volumes, cortical folding patterns should be similar; the extremely preterm infant neonate scans cohort (Section 3.2), which is the main dataset used throughout this thesis; and the EPICure cohort, which contains young adults born extremely preterm and term-born controls, age and socio-economically matched (Section 3.3), used to investigate the long term impact of prematurity. For each data set we describe the population scanned, the recruitment process, MR acquisition, as well as the basic image preprocessing performed.

3.1 Post-mortem Fetal Data: MaRIAS

3.1.1 Subjects

Pre-autopsy post-mortem cerebral MRI was performed on fetuses (scanned ex utero) and newborns, as a part of the Magnetic Resonance Imaging Autopsy Study (MaRIAS) [150]. MaRIAS aims to investigate the use of a less invasive autopsy method instead of the common autopsy: using MRI for post-mortem scans [149]. This dataset is unique and it is the only existing post-mortem fetal MRI of the brain to date, to the best of our knowledge.

MaRIAS consists of 425 datasets acquired between 2007 and 2012, however for this study only post-mortem data from 38 newborns and 39 fetuses was provided. In this study we used the data from 17 fetuses and 17 newborns. The selection of these particular subjects was based on the fact that they presented no major lesions or cerebral hemorrhage and that their scans had higher resolution, better contrast, and no major artifacts, resulting in the exclusion of 21 newborn subjects and 22 fetal subjects.

The 17 newborns used in this study were mostly term-born and aged between 35 and 46 weeks (gestational age (GA) added with age after birth). The 17 fetuses used in this study had GA between 29 and 44 gestational weeks (GW), all calculated based on the mothers last menstruation date.

3.1.2 Recruitment

The study was approved by GOSH and Institute of Child Health (ICH) research ethics committee (04/Q0508/41) [151]. The standard National Health Service (NHS) consent form (produced by Department of Health) that includes consenting for the use of post-mortem imaging for research was used [151]. Research nurses approached the parents by telephone and if verbal consent was gained for MR, a pre-paid envelope with consent form and information leaflet was sent to the parents before post-mortem MRI was performed (the consenting process has been previously described) [148]. Conventional autopsy was performed according to the guidelines set down by the Royal College of Pathologists (UK) [151], during which the cerebrum weight was measured.

3.1.3 MR Acquisition

The scans were acquired at Great Ormond Street Hospital for Children (GOSH) and University College London Hospital (both in London, United Kingdom) between March 1st 2007 and September 30th, 2011 [150] using a 1.5 Tesla Siemens Avanto MR scanner. The total scan time for each subject varied between 90 and 120 minutes [151]. Scans were done as soon as possible, usually between 1 to 7 days after death [150].

For this study, we used the 3D T2-weighted Constructive Interference in Steady State (CISS) MR images which have a voxel size of $0.6 \times 0.6 \times 0.6$ mm^3, acquisition time of 13.5 min, relaxation time (TR) 9.2 ms, echo time (TE) 4.6 ms, flip angle of 70° with 4 signal averages. Other data was also acquired, but it was not used for the purposes of the work presented here [151].

3.1.4 Image Preprocessing

All images underwent bias field correction using the N3 algorithm of FreeSurfer [140]. This was necessary to minimise the registration error induced by intensity non-uniformity as a result of the MR acquisition. Masks of the intracranial volume for both cohorts were resampled from a publicly available neonate brain atlas [79] after a non-rigid registration between each image and the atlas template. All masks were checked and manually corrected to exclude any non-brain tissue that can generate mislabeled voxels in the subsequent segmentation using ITK-SNAP [173] [1].

3.2 Preterm Infant Data: Preterm Development Project

3.2.1 Subjects

Subjects were recruited for this study as part of the University College Hospital (UCH) Preterm Development Project. The study was approved by the local research ethics committee and informed parental consent was obtained for all infants. Imaging was acquired for 42 extremely preterm infants with an average gestational age at birth of 26.27 ± 2.1. For this thesis, we had very strict inclusion criteria. We

[1] http://www.itksnap.org/pmwiki/pmwiki.php

Table 3.1: Preterm Infant Subjects used in this study. Quality control was qualitatively established during preprocessing by visual inspection.

Subject identifier	Estimated Gestational Age at Birth (weeks+days)	EGA at scan 1 (weeks+days)	Quality Control (QC) of scan 1	EGA at scan 2 (weeks+days)	QC of scan 2
a	26+1	33+1	Slight T1 motion	40+1	Good
b	25+1	31+3	Good	42	Good
c	25+1	31	Good	42	Good
d	27+1	30+6	Slight T1 motion	46+2	Good
e	27+1	29+6	Good	46+2	Good
f	26+2	31+6	Good	40+2	Good
g	29+1	31+1	Good	38+3	Good
h	29+2	32+4	Slight T1 motion	38+6	Good
i	26	33	Good	41	Good

excluded infants that presented abnormal cerebral ultrasound (2 infants), had low quality MR images with motion in either the structural or diffusion imaging (5 infants) and infants that did not undergo both scans (25 infants), since we are looking into the longitudinal development. The wider cohort, including the current subjects and the ones that did not undergo both scans but had good quality MR scans, have been used for other studies [49], [93].

We used nine infants with mean gestational age at birth (GAB) of 26.8 ± 1.5 weeks. The infants were scanned first shortly after birth, at average EGA of 31.6 ± 1.1 weeks and then at term equivalent age, at average EGA of 41.7 ± 2.9 weeks. None of the infants were growth restricted. All mothers were on prenatal steroids, but none of the infants were given post-natal steroids. Characteristics of these infants are summarised in Table 3.1.

3.2.2 MR Acquisition

The data was acquired on a Philips Achieva 3T MRI machine. The infants were imaged in an MR-compatible neonate incubator after feeding [122], when spontaneously asleep, without any sedation. Total scanning time was of maximum an hour and included the acquisition of T1-weighted, T2-weighted, NODDI, T2 relaxometry and specstroscopy data [98]. T1-weighted and T2-weighted were repeated if there was motion.

The T1-weighted data used a 3D MP-RAGE at a resolution of 0.82 mm $\times 0.82$ mm $\times 0.5$ mm at TR/TE = $17/4.6$ ms, acquisition duration 462 s. For the diffusion weighted imaging, we acquired six volumes at $b = 0$ s/mm^2, 16 directions at $b = 750$ s/mm^2 and 32 at $b = 2000$ s/mm^2 with TR/TE = $9s/60$ ms.

Other imaging data was also acquired, but it was not used in this thesis. Whole-brain 32-echo multi-component quantitative T2 imaging was acquired using a 2D GraSE acquisition at TE of 12 ms and 1.2 mm $\times$1.2 mm $\times$3 mm resolution [98]. Proton MR spectroscopy was acquired using water suppressed Point Resolved Spectroscopy (PRESS), with TR/TE = $2,288/288$ ms with a 14 mm $\times$13 mm $\times$11 mm voxel in the left posterior white matter [98].

3.2.3 Image Preprocessing

The T1-weighted images underwent bias field correction using the N3 algorithm of FreeSurfer [140], a process that was necessary in order to minimise the registration error induced by intensity non-uniformity as a result of the MR acquisition. Brain masks of the intracranial volume of the later scans were resampled from a publicly available neonate brain atlas described in [79] after a non-rigid registration between each image and the atlas template. Brain masks for the early scans were resampled from their corresponding 40 week EGA mask after affine alignment. All masks were checked and manually corrected to exclude any non-brain tissue that can generate mislabelled voxels [169] in the subsequent segmentation using ITK-SNAP [173].

The diffusion-weighted images were corrected for Eddy currents and motion artefacts. Bulk motion during the acquisition protocol is very common in the neonatal population, and this creates a displacement in the images [49]. Firstly, we manually identified and removed volumes affected by their signal dropout caused by subject's motion [49]. Secondly, we registered each volume to the groupwise average of all of the b = 0 images [49]. Thirdly, we fit the diffusion tensor model using NiftyFit [98] to produce synthetic images, for each b-values and gradient direction. Each raw image is then affinely registered to its 'synthetic' reference image, which we generated in order to register to a target with similar contrast [49]. We then rotated the b-vectors and modulated the image intensities using the Jacobian determinant obtained from the affine transformations [71], assuming that the largest part of the rotation in the affine transformation was due to bulk motion [81]. All registrations are carried out using NiftyReg[2]. From the diffusion tensor images (DTIs) we obtained fractional anisotropy (FA) and mean diffusivity (MD) maps.

We registered the T1 images to the FA maps rigidly in order to propagate the brain masks and segmentations from T1 to diffusion space. Furthermore, we used this registration to bring the DT images into T1 space before performing a proper multi-modal registration (Chapter 9).

3.3 Preterm Young Adult Data: EPICure Study

3.3.1 Subjects

Data was acquired for a cohort of 143 adolescents at 19 years of age, all born in 1995, as part of the EPICure study (`http://www.epicure.ac.uk/epicure-1995/`). The data acquisition was approved by the local research ethics committee. The EPICure study comprises data for 89 extremely

[2]https://sourceforge.net/projects/niftyreg/

preterm adolescents (F/M = 52/37, mean birth gestation $= 25.0 \pm 0.8$ weeks) and 54 (F/M = 32/22) term-born socio-economically matched peers.

The extremely preterm subjects were recruited in 276 maternity units across the United Kingdom and the Republic of Ireland in 1995 [40] and were followed up throughout their life, at one, two and a half, six, 11, 16 and 19 years, with a variety of health and psychological checkups. At the last checkup at 19 years, in 2014, the subjects were scanned at University College Hospital. The controls were recruited as classmates in childhood at either 6 or 11 years [43].

For this thesis, we included only subjects which had motion-free T1-weighted images, no ventriculomegaly and no particular abnormality. We used 60 extremely preterm born young adults (F/M = 38/22) and 48 controls (F/M = 29/19).

3.3.2 MR Acquisition

Images were acquired on a 3T Phillips Achieva. We acquired 3D T1-weighted (TR/TE = $6.93/3.14$ ms) volume at 1 mm isotropic resolution and a acquired 3D T2-weighted (TR/TE = $2500/211$ ms) volume at 1 mm isotropic resolution. Diffusion weighted data was acquired across four b-values at $b = 0, 300, 700, 2000$ s/mm^2 with n $= \{4, 8, 16, 32\}$ directions respectively at TE = 70 ms (2.5 mm $\times 2.5$ mm $\times 3.0$ mm). B0 and B1 field maps were acquired to correct for EPI-based distortions and signal inhomogeneity in the imaging volumes.

Other data was also acquired but not used for the purpose of this study, such as T2-weighted data with ten echo times at TE $= \{13, 16, 20, 25, 30, 40, 50, 85, 100, 150\}$ ms with a resolution of 2.5 mm $\times 2.5$ mm $\times 3.0$ mm. BOLD-weighted fMRI was acquired with TR 3000 ms, TE 30 ms, flip angle 80°, voxel size $2.5 \times 2.5 \times 3$ mm ^{3}, field of view (FoV) 240 mm^2, 50 oblique transverse slices, slice order descending. Pulse oximetry records were available for each individual subject of this cohort but not synchronised to the MR data acquisition. Pseudo-Continuous ASL (PCASL) was acquired for 30 control-label pairs with PLD= 1800 ms $+41$ ms/slice, label duration $\tau = 1650$ ms (resolution $3 \times 3 \times 5$ mm^3) [3]. Acquisition was carried out using 2D echo-planar imaging in the same geometry as the diffusion-weighted data ensuring similar levels of distortion.

3.3.3 Brain Segmentation

Brain segmentation and labelling was performed using the GIF framework [29]. An example subjects with GIF segmentation of the entire brain, as well as particular structures such as the thalamus, cerebellum and white matter segmentations, is showed in Figure 3.1.

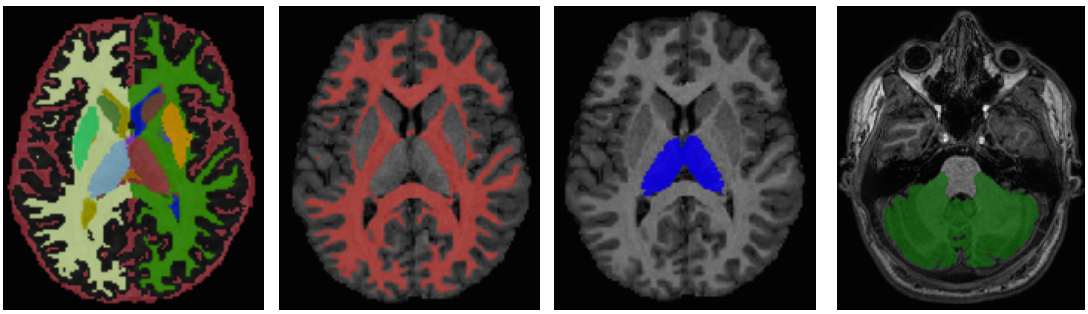

(a) GIF Labels (b) White matter (c) Thalamus (d) Cerebellum

Figure 3.1: Example of T1-weighted image of EPICure subject with tissue and region labelling after GIF segmentation and white matter, thalamus and cerebellum segmentations

Chapter 4

Voxel-wise Image Analysis: Application to Post-mortem Fetal MRI

The data used in this section is described in Chapter 3, Section 3.1 (post-mortem fetal data). The aims of this chapter are to: 1) Compare a new semi-automatic post-mortem voxel-based segmentation with the manual segmentation for newborns (35-46 weeks equivalent gestational age); 2) Create a new post-mortem brain atlas for newborns (35-46 weeks equivalent gestational age); 3) Compare the results of the fetal cohort post-mortem brain segmentation (29-44 GW) using the new post-mortem brain atlas for newborns versus a publicly available neonatal atlas; 4) Compare the estimated brain weights obtained from semi-automatic segmentation with post-mortem conventional autopsy ones in both newborns and fetuses; 5) Compute growth rates for these cohorts and compare them with other in vivo studies. This was the first time, to the best of our knowledge, to segment both fetal and neonate post-mortem brain MRI using semi-automatic techniques.

Accurate estimation of brain weight is an integral part of autopsy, since any deviation from the normal ranges could be an indicator of pathological change in the organ and therefore helps in establishing the cause of death. Rapid prototyping of organs may be useful also in explaining the pathologies to parents and to the jury in forensic cases [1]. During conventional autopsy, the cerebellum and brainstem are usually separated from the cerebrum and are weighed separately. Similarly then, it is useful to segment the cerebrum, cerebellum and brainstem from the brain MR images. Manual segmentation of organ volumes on MRI is labor intensive [21] and unsuitable for routine clinical practice.

Derived publications:

- **Orasanu, E.**, Melbourne, A., Cardoso, M.J., Modat, M., Taylor, A.M., Thayyil, S., Ourselin, S., Brain volume estimation from post-mortem newborn and fetal MRI. Neuroimage: Clinical, 2014
- **Orasanu, E.**, Melbourne, A., Cardoso, M.J., Modat, M., Taylor, A.M., Thayyil, S., Ourselin, S., Fully automated estimation of brain volumes in post-mortem newborn and stillborn infants. ISMRM, 2014
- **Orasanu, E.**, Melbourne, A., Cardoso, M.J., Modat, M., Taylor, A.M., Thayyil, S., Ourselin,

S., Average probabilistic brain atlases for post-mortem newborn and stillborn populations and application to tissue segmentation. ISMRM, 2014

4.1 Methods

4.1.1 Newborn Brain Segmentation

The segmentation pipeline for the newborn brain consisted of two main stages. In the first stage, we carried out a non-rigid registration of the masked brain images to the template of the publicly available atlas which was closest to the age of each subject (in gestational weeks) [79]. The obtained transformation was then used to resample, from this atlas, the corresponding anatomical priors for 4 different areas of the brain: cerebrum, cerebellum, brainstem and cerebrospinal fluid (CSF). The cerebrum class contained both white and grey matter, as it was not possible to segment them separately likely due to the difference between their T1 and T2 values decreasing significantly after death due to brain decay [147]. Using the derived anatomical priors and a neonate specific Expectation-Maximization (EM) segmentation algorithm with prior relaxation and a Markov Random Field to enforce spatial smoothness (AdaPT) [28], available in NiftySeg[1], we segmented the brain into the 4 tissue classes/areas mentioned above.

The second stage consisted of combining together the cerebrum and CSF classes. This was necessary since, because of the aforementioned T1 and T2 increasing values post-mortem, the CSF and cerebrum were difficult to separate mainly in the parietal and frontal lobes. However, having this class at the beginning was necessary in order to get a robust segmentation of the cerebellum and brainstem, which, in newborns and fetuses, are surrounded by fluid.

After this pipeline, the newborn brains are segmented into three regions: 1. cerebrum plus CSF (including extra axial spaces and ventricles), 2. cerebellum and 3. brainstem.

4.1.2 Post-mortem Newborn Average Atlas

An average image and an average segmentation were created for the newborn cohort using the available 17 images [112]. A groupwise average was created using NiftyReg by performing a sequence of registrations with increasing number of degrees of freedom, each time registering the images to a new average space. We performed one rigid, four affine [121] and four non-rigid (free-form deformation model based on cubic B-splines) [132], [101] registration steps. For all of the registration steps mentioned we used the default parameters. The number of registration steps in a groupwise registration typically depends on the diversity of the images. Note that after four non-linear registration steps the transformations from the native image spaces to the average image space did not change significantly. The obtained transformations from each native space to the average space were used to propagate the individual segmentation and create an average segmentation for all brain regions mentioned, as well as an average mask.

[1] https://sourceforge.net/projects/niftyseg/

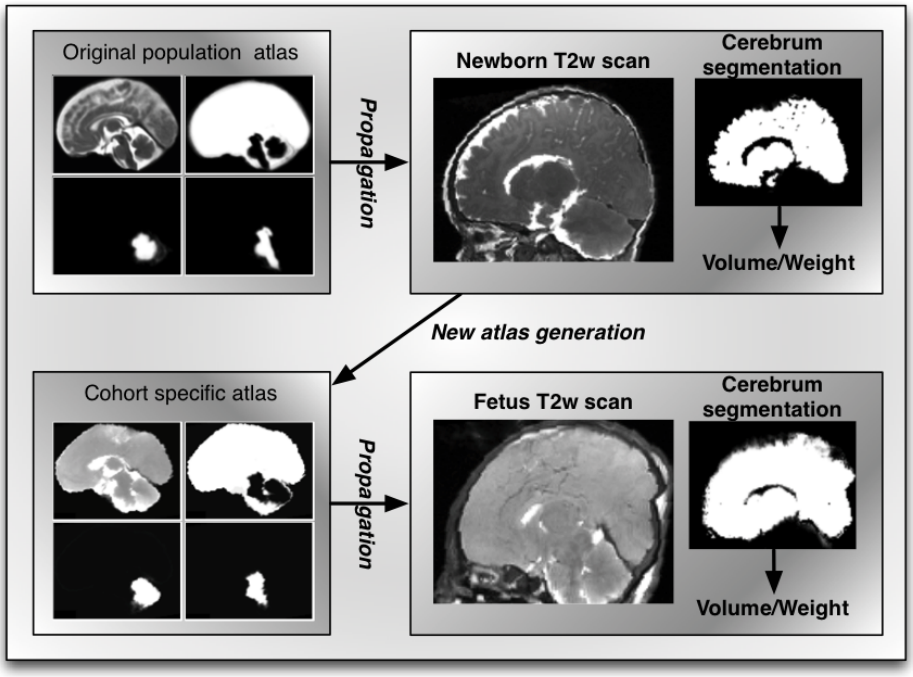

Figure 4.1: Processing pipeline: A publicly available atlas was used to create the priors for AdaPT segmentation of the newborn cohort. A new atlas was generated from the newborn cohort segmentations and used to create the priors for AdaPT segmentation of the fetus cohort. The cerebrum volumes/weights were computed from the thresholded cerebrum segmentation.

4.1.3 Fetal Brain Segmentation

We segmented the fetus cohort into cerebrum plus cerebrospinal fluid, cerebellum and brainstem using the same two-stage segmentation pipeline, but by using different anatomical priors in the first stage [110]. In this case, the fetal brain images were non-rigidly registered to the newly created post-mortem newborn atlas and the transformation obtained was used to resample the anatomical priors from this atlas. We compared qualitatively (by visual inspection) and quantitatively (Dice score comparison) the segmentation using this prior [110] to the ones obtained using the template of the publicly available atlas which was closest to the age of each subject (in gestational weeks) [79]. Using the newly created atlas, rather than the publicly available one, is expected to give a more accurate and precise segmentations because the post-mortem fetus MR images are more similar to the post-mortem newborn ones as a results of undergoing the same changes in tissue contrast that appear after death. The algorithm pipeline describing the segmentation propagation is shown in Figure 4.1.

4.1.4 Validation

To perform quantitative evaluation of the automatic segmentations, we manually segmented the MR images from 8 randomly selected subjects using ITK-SNAP [173] from each cohort into the three regions of interest: cerebrum and CSF, cerebellum and brainstem. The investigator was blinded to the semi-automatic segmentation results and has substantial image analysis expertise but limited neuroanatomical

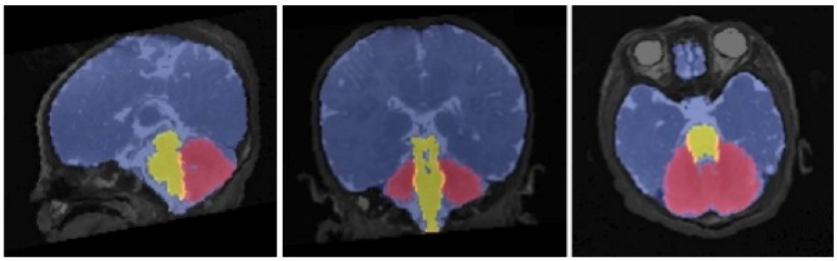

(a) Sagittal view (b) Coronal view (c) Axial view

Figure 4.2: Example segmentation of a MaRIAS Newborn (44 week gestation)

expertise. We then computed the Dice score overlap (defined here as the number of voxel labels that agree between two images, divided by the average number of voxels with that label in those images), between the automatic and manual segmentations.

4.1.5 Eliminating Cerebral Fluid

The segmentation region of interest for both cohorts is composed of cerebrum and CSF, since they could not be separated because of lack of prior information. We manually thresholded the segmentation to properly eliminate any fluids that do not contribute to the cerebrum weight obtained during autopsy [16]. The fluid threshold values were taken individually for each patient from the bias field corrected images and voxels with higher values than the threshold were excluded from the volume.

4.1.6 Post-mortem Cerebrum Weights

We computed the volume of the cerebrum as the binary sum of all pixels in the region of interest segmentation multiplied by the voxel dimension (provided by the scanner). The cerebrum weight can be estimated by multiplying this volume with a literature-derived density value of the brain of 1.08 g/ml [22]. We compared the estimated weights with the autopsy weights, which are available for 15 newborn and 13 fetus subjects.

4.2 Results

4.2.1 Atlas-based Brain Segmentation

An example segmentation is shown in Figure 4.2. The average Dice overlap between the automatic and manual segmentations are included in Table 4.1 .

When compared with the manual segmentation, the fetus segmentation obtained using priors derived from the public atlas had lower Dice score values than the ones obtained using the newly created newborn atlas for all three structures. Improvement of the segmentation by using the newly created atlas as template can also be observed in Figure 4.3.

Table 4.1: Dice overlap of automatic segmentation with manual segmentation for each structure amongst each cohort

	Cerebrum + CSF	Cerebellum	Brainstem
Newborn	0.991 ± 0.002	0.873 ± 0.028	0.819 ± 0.031
Fetus	0.992 ± 0.002	0.888 ± 0.016	0.815 ± 0.035
Fetus (*public atlas*) [79]	0.984 ± 0.012	0.756 ± 0.185	0.676 ± 0.262

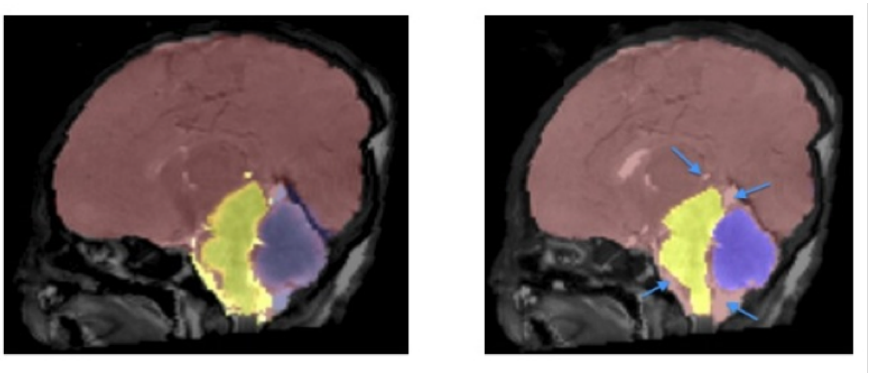

Figure 4.3: Brain segmentation of MaRIAS Fetus of 38 GW using the public atlas (left) and using the MaRIAS Newborn atlas (right).

4.2.2 Post-mortem Cerebrum Volumes

We estimated the cerebrum volumes and weights from the segmentation of the MR images for the newborn (4.2) and fetus (4.3) cohorts after thresholding to remove CSF. We compared the estimated cerebrum weight for the newborn and fetus cohorts with the available autopsy weights (15 newborns and 13 fetuses). The Bland-Altman plot comparing the MRI weight and autopsy weight are shown for the newborn cohort in Figure 4.4 and for the fetal cohort in Figure 4.5.

For the newborn cohort, the mean weight estimate by MRI and conventional autopsy was 418 g versus 434 g. The mean absolute difference (mean of all the absolute differences between the MRI and conventional autopsy weights) was 20 g and the 95% confidence interval (CI) is $[-32, 65]$ g. For the fetus cohort, the mean weight estimate by MRI and conventional autopsy was 310 versus 312 g. The mean absolute difference was 5 g and the 95% CI is $[-7, 12]$ g.

4.2.3 Brain Growth Rates of Normal Development from Post-mortem MRI

We plotted the volumes of the three segmented regions as a function of gestational age for the two cohorts (Figure 4.6). Assuming a linear increase ($R^2 > 0.85$ for all structures), we then computed the growth rates per week for the cerebrum, cerebellum and brainstem. The rates are summarised in *Table* 4.4.

Table 4.2: Comparison between MRI weights, MRI manual weights and autopsy weights of the cerebrum for newborns. Density for cerebrum used to compute the weight from the MR volume: 1.08 g/mL. The threshold values used to remove the CSF from the MR segmentation are also included. The subjects for which manual segmentation was performed are indicated with *.

MaRIAS No.	Gestational Age (weeks)	Postnatal Age (days)	CSF Threshold Value	MRI Volume (mL)	MRI Weight (grams)	MRI Manual Weight (grams)	Autopsy Weight (grams)
193*	40	21	600	418.15	451.61	446.08	457.0
194*	39	1	600	418.56	452.05	446.46	462.5
256	38	1	800	360.43	389.27	N/A	433.0
259*	29	120	400	413.45	446.52	442.92	456.7
262	37	3	500	338.13	365.18	N/A	368.0
274	40	2	600	430.50	481.29	N/A	N/A
276	41	1	600	333.32	359.99	N/A	367.0
293*	35	10	600	329.07	355.40	350.62	360.0
300	40	1	400	388.61	419.70	N/A	420.0
306*	37	1	500	287.15	345.49	309.86	N/A
313	37	3	800	310.26	335.08	N/A	360.0
315*	40	3	900	321.41	347.13	347.30	409.0
318	40	2	400	313.07	338.12	N/A	368.0
325*	40	30	500	586.24	633.14	627.79	635.0
356	40	1	600	428.28	462.54	N/A	445.9
368	35	5	600	345.69	373.35	N/A	363.8
386*	40	30	700	501.73	541.87	534.37	609.0

Table 4.3: Comparison between MRI weights, MRI manual weights and autopsy weights of the cerebrum for fetuses. Density for cerebrum used to compute the weight from the MR volume: 1.08 g/mL. The threshold values used to remove the CSF from the MR segmentation are also included. The subjects for which manual segmentation was performed are indicated with *.

MaRIAS No.	Gestational (weeks)	Age (days)	CSF Threshold Value	MRI Volume (mL)	MRI Weight (grams)	MRI Manual Weight (grams)	Autopsy Weight (grams)
121*	39	0	700	361.74	390.67	390.40	388.00
149	34	2	700	267.79	289.22	N/A	N/A
196*	32	2	800	160.66	173.52	172.59	181.00
210	38	6	600	354.74	383.12	N/A	391.00
214	37	2	550	298.07	321.92	N/A	328.00
230	41	6	450	370.73	400.39	N/A	401.00
246*	32	6	530	208.06	224.70	225.54	223.70
282	30	5	500	146.96	158.72	N/A	N/A
299*	44	0	300	408.43	441.11	438.00	447.00
330	35	6	800	264.72	285.90	N/A	292.00
339*	36	2	800	339.31	366.45	365.05	N/A
343	34	1	350	247.69	267.50	N/A	275.00
379	38	5	290	357.13	385.70	N/A	386.13
384	39	4	300	366.63	395.96	N/A	389.80
388*	38	0	390	439.41	474.56	469.56	N/A
391*	33	0	550	213.39	230.46	231.59	226.00
396*	29	0	700	113.70	122.80	122.22	128.00

Table 4.4: Brain growth rates from post-mortem infant MRI

	Age Range [weeks]	Cerebrum Rate [mL/week]	Cerebellum Rate [mL/week]	Brainstem Rate [mL/week]
Newborn	35 - 46	21.27 ± 6.75	2.32 ± 0.58	0.23 ± 0.09
Fetus	29 - 44	21.87 ± 6.23	1.51 ± 0.42	0.22 ± 0.10

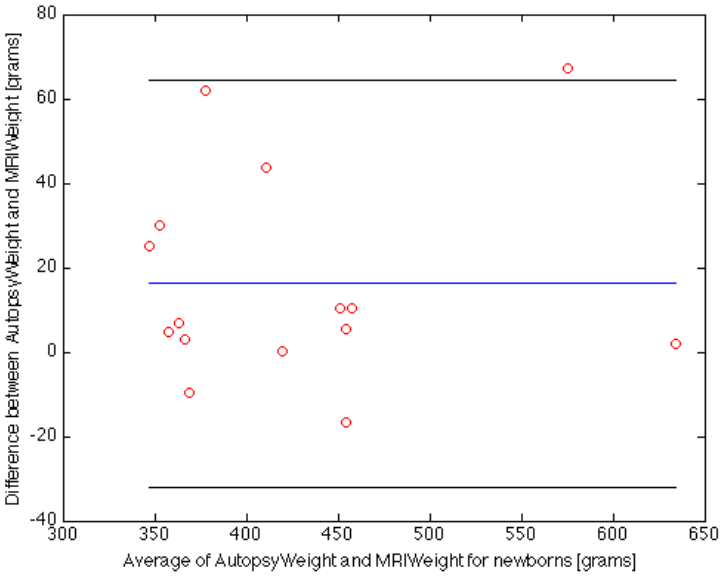

Figure 4.4: Bland-Altman plot for the MaRIAS newborn cohort showing differences between the conventional autopsy weights of the brain (cerebrum only, no fluid) and the automatic segmented ones from the MR images. The blue line corresponds to the average difference between the Autopsy and MRI weight, while the black lines indicate the 95% limits of agreement (average difference ± 1.96 standard deviation of the difference).

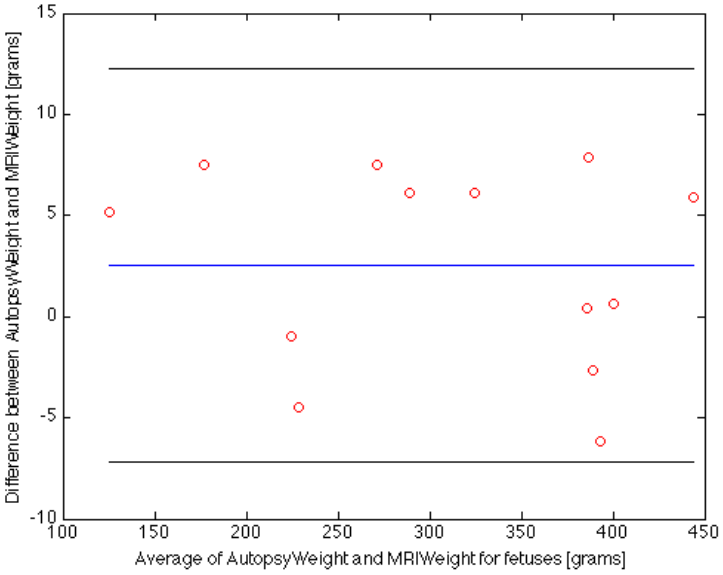

Figure 4.5: Bland-Altman plot for the MaRIAS fetal cohort showing differences between the conventional autopsy weights of the brain (cerebrum only, no fluid) and the automatically segmented ones from the MR images. The blue line corresponds to the average difference between the Autopsy and MRI weight, while the black lines indicate the 95% limits of agreement (average difference ± 1.96 standard deviation of the difference).

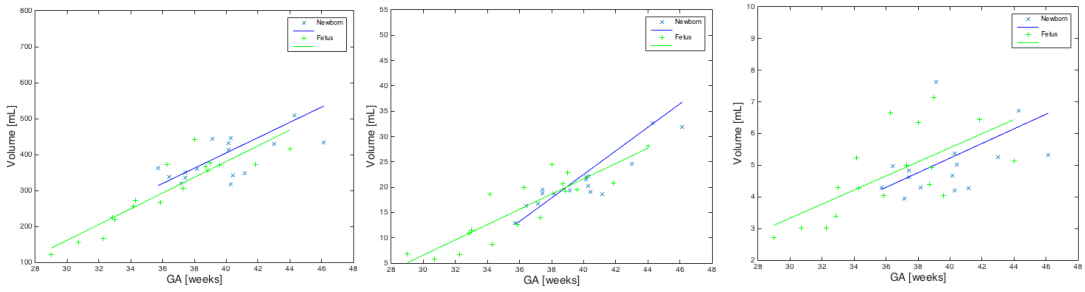

(a) Cerebrum (b) Cerebellum (c) Brainstem

Figure 4.6: Volumes of the cerebrum, cerebellum and brainstem plotted as a function of equivalent gestational age for post-mortem newborn and fetuses. The slope represents the growth rates.

4.3 Discussion

We semi-automatically segmented the cerebrum and CSF, cerebellum and brainstem from the T2-weighted MR images (CISS) of 17 newborn and 17 fetal subjects part of the MaRIAS study using an algorithm based on an Expectation-Maximization process combined with a prior relaxation scheme (AdaPT) [28].

The average Dice overlap between the semi-automatic and manual segmentations showed good average agreement for all structures. The Dice score is affected by structure size, thus explaining the lower Dice scores in cerebellum and brainstem when compared to the cerebrum and CSF. In tissue segmentation, the choice of the atlas is extremely important. Having an atlas based on subjects that undergo similar post-mortem processes will improve the results. When compared with the manual segmentation, the fetus segmentation obtained using priors derived from the public atlas had lower Dice score values than those obtained using the newly created newborn atlas (Table 4.1 and Figure 4.3). Although the contrast between the fetal brain and the newborn one, part of the same study, might be larger, the contrast between grey matter, white matter and CSF is much lower in both cohorts. This low difference could potentially explain the better fetal segmentation when using the created atlas over the publicly available one.

There are several limitations to the current study. Firstly, we used a relatively small subset of the MaRIAS cohort, which may restrict the generalisability of our conclusion. Secondly, the subjects included in the study also had good resolution and contrast and no major imaging artifact. Although the estimation was not tested on post-mortem brains that present different pathologies or have lower quality images, the AdaPT segmentation algorithm might be able to successfully segment brain lesions because it has been shown to segment highly variable cases in neonates [28]. Thirdly, as mentioned, the brain is separated into three parts during conventional autopsy: cerebrum, cerebellum and brainstem, but we were only provided with the cerebrum weights. If cerebellum or brainstem weights were also available we could further validate whether a good estimation can be made for all brain structures. Lastly, the main limitation of our study is that we were not able to separate the CSF from the cerebrum automatically, because of the brain decay after death and the relaxation rates, T1 and T2, increasing and converging to free water

values [147]. We attempted to separate the cerebrum/CSF by manually choosing thresholds. We report all CSF threshold values to ensure reproducibility and guidance for future studies. This issue might be solved in the future by using a post-mortem neonatal atlas, which should include a CSF class, created from manual segmentations of MR images of such subjects. Another solution to make the choice of the CSF threshold automatic might be creating an intensity histogram of the cerebrum-CSF segmentation. With sufficient further information, like post-mortem T2 relaxometry [80], brain maceration in fetuses and newborns could also be modelled and thus included as part of the segmentation process.

4.3.1 Post-mortem MRI as an alternative to conventional autopsy

We compared the estimated cerebrum weight for the newborn and fetal cohorts with the available autopsy weights. Both cohorts showed that MRI-derived brain weights were accurate. However, the results of the fetus cohort appeared more accurate, probably due to smaller variation among the subjects resulting from their smaller differences in age, shape, size or structure [111].

Disagreement between the MRI-derived and autopsy weights could be due to fluid loss at autopsy. In the computation of the MRI brain weight, we attempted to exclude the contribution of the fluid based on the assumption that it partially leaks in the autopsy process and therefore is lost before weighing. However, some fluid might remain in the tissue, contributing to the autopsy weights. The fixation process of the brain can also introduce errors in the conventional autopsy brain weight and cause disagreement with the MRI brain weight. Further disagreement between the two values could also come from the cerebrum density value used from the literature, which may not be accurate for our subjects. By plotting the autopsy volumes as a function of volume computed from the MR images with 0 intercept, the new cerebrum densities obtained are $1.120 \pm 0.095 g/cm^3$ for newborns and $1.087 \pm 0.018 g/cm^3$ for fetuses. The values are similar to the literature value of $1.08 g/cm^3$ determined from post-mortem fetus subjects [22], however the cerebrum density of the newborn is slightly bigger and thus using this value can decrease the error between the autopsy cerebrum weight and MR cerebrum weight. Using the Fisher r-to-z transformation $z = 4.18, p < 0.001$, we can also conclude that the cerebrum densities for newborn and fetuses are different. It appears that the density increases for the newborn, which could be explained by the water decrease in the newborn brain.

Nevertheless, post-mortem MRI can give a good estimation of the cerebrum weight for neonatal subjects, which is an important part of autopsy. The results of this section are notable, since they strengthen the idea of using MRI as an alternative to conventional autopsy, an alternative that can be more acceptable for parents and society at large. It also does not delay the funeral since it does not require a fixation process. To our knowledge this is the first paper to estimate brain weights from MR images of neonates and fetuses for the purpose of autopsy. The processing pipeline, which will also be made available, is reproducible since all the software used in this study is publicly available. We used the default registration parameters for all of the registration steps mentioned. Furthermore, the atlases used as prior information for segmentation are also freely available [79] and the newborn post-mortem atlas created will be made available. We speculate that this availability will allow further research of post-mortem MRI of neonates

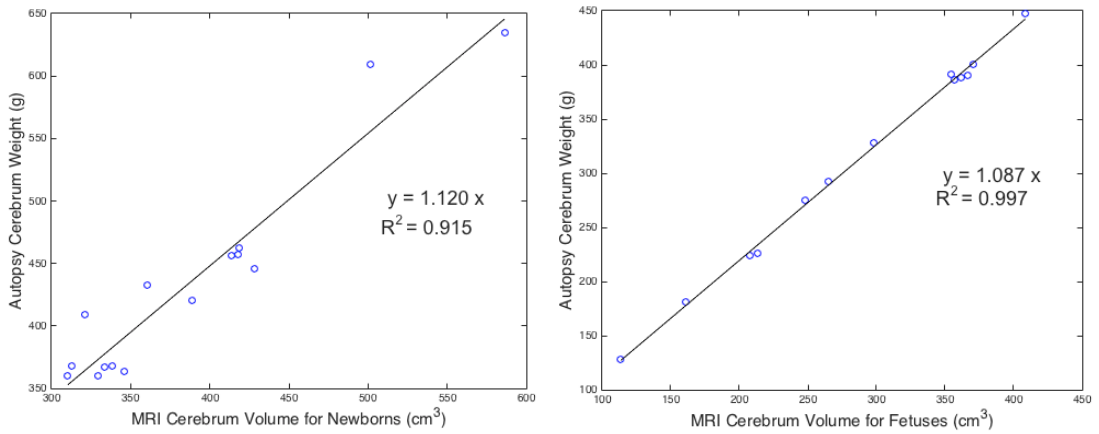

(a) Post-mortem Newborns

(b) Post-mortem Fetuses

Figure 4.7: Autopsy cerebrum weight of MaRIAS newborns and fetuses as a function of volume from the MR images. The slope represents the approximate actual density

and fetuses.

4.3.2 Brain growth rates from post-mortem MRI

When looking at the rates of change as a function of gestational age, we notice an increasing similar rate of change for both the post-mortem fetuses and newborns (Figure 4.6, a). The smaller rate of cerebrum increase for the newborns suggests that little growth is expected after 44 GW. The cerebellum shows a more sudden increase for the newborns (Figure 4.6, b). This abrupt rate for late GA is explained by the fact that the cerebellum doubles in size from 19 to 37 GW [155]. The brainstem shows an constant increase rate (Figure 4.6, c).

We calculated the rate of growth for each region and each cohort and then also computed the growth rates for the cerebrum, cerebellum and brainstem obtained by Kuklisova-Murgasova et al. (2011) in her study of preterm neonates aged between 29 and 44 GW. Since the gestational ages were similar, we compared our growth values to theirs. The growth rate of the cerebrum was about 21.6 mL/week, which is very close to the values obtained for the the two cohorts and within the error range. The cerebellum and brainstem had a growth rate of about 0.9 mL/week and 0.13 mL/week respectively, values that are lower than the ones obtained and outside error range. Limperopoulos et al. (2005) found a growth rate of the cerebellum of 1.57 mL/week for preterm infants aged between 28 and 40 GW [82], a similar value with the one obtain for the fetal population with similar gestational ages. Clouchoux et al. (2012) obtained a growth rate of 1.23 mL/week for the cerebellum and 0.22 mL/week for the brainstem for in utero fetuses aged 25-37 weeks [35]. The cerebellum and cerebrum values are lower than the one obtained for the fetuses or newborns but within the error range (except for the rate of the cerebellum increase for newborns), while the brainstem rate is in full agreement. The disagreement of the cerebellum rates can also be due to the fact that the our cohorts cover a later gestational age timeline than this study, in which the cerebellum continues to expand. We can conclude that growth rates obtained from post-mortem

fetal and neonate MRI are comparable with in vivo measurement in the case of normal developing brain.

4.3.3 Limitations of voxel-wise intensity-based methods

The are some limitations of voxel-wise methods, especially voxel-wise intensity-based registration. Firstly, voxel-wise registration methods rely on intensity information, not investigating the surface anatomical information. Secondly, voxel-wise registration techniques usually cannot cope with large deformations, like the ones that take place during the early developmental stages. Thirdly, voxel-wise methods are often computationally expensive, when compared to surface registration techniques. Surface-based registration techniques offer a faster approach and are usually preferred when studying changes in folding patterns and morphology.

Chapter 5

Spectral Graph Theory

In this chapter we introduce the basic spectral graph theory concepts and how these could be applied in medical image analysis.

5.1 Introduction to Graph Theory

Graphs are mathematical structures used to model relations between objects consisting of vertices or nodes connected by edges and can be represented by matrices[19]. Spectral graph theory studies the properties of graphs with respect to the properties of their associated matrices [34].

Spectral graph theory has been widely used in the last decade. Several new spectral techniques have been developed to deal with general graphs. A main goal of graph theory is to compute the principal properties and structure of a graph from its "spectrum", and to achieve this it makes use of the spectral decomposition of a graph. The eigenvalues obtained after the decomposition (called the "spectra") have the advantage of linking one extremal graph property to another and are closely related to most of the major invariants of the graph [34]. Thus, the eigenvalues play a crucial role in understanding graphs.

Spectral graph theory has applications in various fields: medical imaging, when describing the shape of an object; chemistry, where eigenvalues are associated with the molecule's stability; pure mathematics, such as its analogy with spectral Riemannian geometry; theoretical physics and quantum mechanics, for example minimising energies of Hamiltonian systems [34].

5.2 Matrices associated with a graph

Let $\mathcal{G} = \{V, E\}$ be a connected graph, with the nodes of the graph given by $V = (x_1, ..., x_N)$ and E the edges/connections between nodes [34].

The adjacency matrix W is the $N \times N$ matrix representation of the weighted graph, where N is the number of nodes in the graph. The weighted graph describes the local node similarities $Sim(x_i, x_j)$. For each pair of nodes x_i and x_j, $i \neq j$, we estimate the entry w_{ij} of the adjacency matrix W, based on

the node affinity defined by a similarity metrics of the two nodes $Sim(x_i, x_j)$.

$$w_{ij} = \begin{cases} Sim(x_i, x_j) & \text{if the nodes } i \text{ and } j \text{ are connected} \\ 0 & \text{otherwise} \end{cases} \tag{5.2.1}$$

The degree matrix D is the diagonal matrix whose entries D_{ii} are the sum of the weights of the graph edges associated with the voxels x_i:

$$D_{ii} = \sum_j W_{ij}. \tag{5.2.2}$$

G is the diagonal node weight matrix and in most cases is set to $G = D$.

We can further construct the graph Laplacian matrix $\mathcal{L}$ associated with the graph $\mathcal{G} = \{V, E\}$. The general or Random Walk graph Laplacian is computed as:

$$\mathcal{L} = G^{-1}(D - W), \tag{5.2.3}$$

A more general and common form is the symmetric normalised Laplacian, given by:

$$\mathcal{L} = D^{-1/2}(D - W)D^{-1/2}. \tag{5.2.4}$$

More details on the graph Laplacian and its properties are stated in Chung et al. (1997) [34].

5.3 Spectral Decomposition of a Graph Laplacian

The general graph Laplacian is a symmetric and positive definite matrix, hence we can look into its properties after eigen-decomposition, which gives the graph spectrum:

$$\mathcal{L} = \mathbf{U}\Lambda\mathbf{U}^{-1}, \tag{5.3.1}$$

and it is thus identified by the eigenvalues $\Lambda = (\lambda_0, \lambda_1, \ldots, \lambda_N)$, and by their associated *spectral components* $\mathbf{U} = (U_0, U_1, \ldots, U_k)$.

The eigenvectors, also known as spectral components, represent frequencies of vibration and provide information on the overall graph properties. The spectral components $(U_1, \ldots, U_k)$ represent the fundamental modes of vibrations and describe the increasing complexity of the geometric features of the graph, from coarse to fine scales [85]. Hence, the eigenvectors corresponding to the higher eigenvalues, the higher modes, are more informative at finer scale. Each eigenvector U_i is a column matrix with N values, where N is the number of nodes. Each eigenvector represents a different weighted harmonic on the graph, which corresponds to the inherent property of the graph's geometry [85], [84]. The eigenvalues provide the global shape properties of the graph.

An example of the entire spectral decomposition process is given in Figure 5.1.

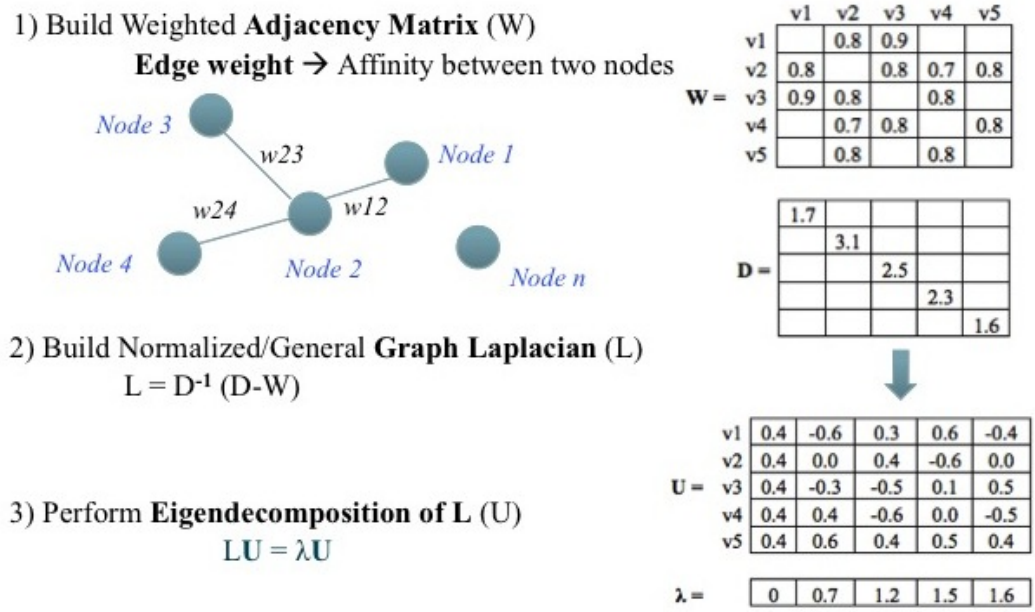

W	v1	v2	v3	v4	v5
v1		0.8	0.9		
v2	0.8		0.8	0.7	0.8
v3	0.9	0.8		0.8	
v4		0.7	0.8		0.8
v5		0.8		0.8	

D					
	1.7				
		3.1			
			2.5		
				2.3	
					1.6

U					
v1	0.4	-0.6	0.3	0.6	-0.4
v2	0.4	0.0	0.4	-0.6	0.0
v3	0.4	-0.3	-0.5	0.1	0.5
v4	0.4	0.4	-0.6	0.0	-0.5
v5	0.4	0.6	0.4	0.5	0.4

λ					
	0	0.7	1.2	1.5	1.6

Figure 5.1: Example spectral decomposition pipeline. After defining the weighted adjacency matrix, the diagonal degree matrix is computed by adding all values column-wise. We then compute the graph Laplacian which is decomposed to obtain the eigenvectors and eigenvalues.

An example of the first spectral components of a shape decomposition is shown below in Figure 5.2.

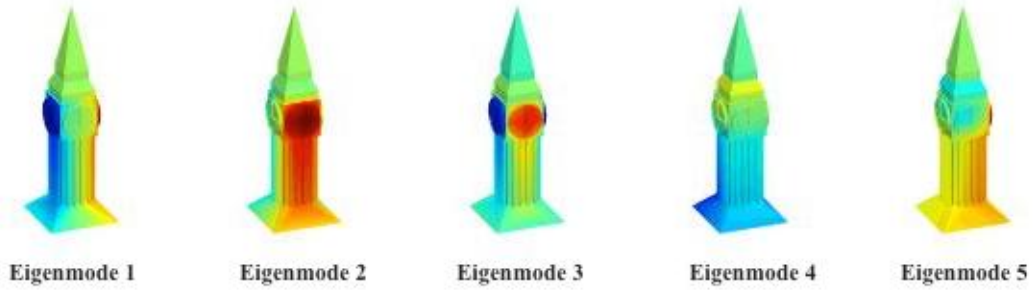

Figure 5.2: Example of the first 5 spectral modes of shape variation of the Big Ben.

The eigendecomposition is however unstable. Eigenvectors can change sign, shape and orientation, due to possible multiplicities of eigenvalues, ambiguities in shape symmetry, and to numerical instabilities [83]. For example, the Laplacian eigenvectors of a sphere have ambiguous orientations so the spectral embeddings are hardly comparable for near spherical shapes [83].

5.4 Spectral Graph Methods in Medical Imaging

In medical imaging, the image or shape is seen as a discrete set of measures at each voxel or vertex. We can construct the connected graph $\mathcal{G} = \{V, E\}$, associated with the image or shape, with the nodes of the graph $V = (x_1, ..., x_N)$ representing voxels in the image or vertices in a surface mesh, and the edges/connections between nodes E representing the relationship between the voxels or vertices expressed by local similarity [59].

The similarity (or affinity) of the nodes $Sim(x_i, x_j)$ (edges of the graph) is usually given by the Euclidean distance between the connected nodes in the case of shapes, where the nodes are vertices of a triangular mesh [59]. In the case of images when the nodes are image voxels, the similarity is based upon both Euclidean distance and difference of the image intensity [84].

Spectral components have been used in the field of medical imaging to describe the shape variation, or different surfaces and structures from the image. The key is to find the most suitable similarity term that describes the properties that one wants to present about the image or shape.

5.5 Matching of the Spectral Representations

If we want to define a matching of surfaces or images that are very different in cartesian coordinates, an easy way would be to take advantage of their spectral representation and match the spectra instead. Spectral matching methods have been used recently for several applications that involve finding correspondences between surfaces in the spectral domain [86], [167].

The k-dimensional embedding of the shape S [85] or image I [84] can be denoted by using the first k spectral components, where each node i has the spectral coordinates defined as $(U_{1i}, U_{2i}, ..., U_{ki})$, which is a row of the truncated matrix **U**. A point-wise correspondence map c can then be established with pairs of closest points, defined by the shortest Euclidean distance between the spectral representation of the surfaces S_1 and S_2 or two images I_1 and I_2, respectively. Notably, the advantage of spectral matching is that the graphs being mapped do not need to have the same number of nodes as there is not a one-to-one mapping [85].

However, the spectral coordinates of two different graphs may not be directly comparable, due to sign ambiguity and ordering. In the former case, a sign ambiguity may exist when computing the eigenvectors, hence it has to be checked that each corresponding eigenvector in the two meshes/images has the same sign. In the latter case, the ordering of the lowest eigenvectors or frequencies might be different as a result of eigenvalues multiplicity [85].

Complex geometries, such as cortical surfaces, become reduced embeddings that are isometry-invariant, i.e., two shapes having the same intrinsic geometry, with identical geodesic distances be- tween points, yield identical spectral embeddings, even if they have different extrinsic geometries. This is equivalent to comparing intrinsic vibration properties of shapes rather than their external configurations. However, a perturbation in shape isometry, such as expansion and compression of surfaces, changes the Laplacian

eigenvectors in the spectral embeddings. This limited the use of spectral methods to coarse align- ment [16] or global analysis [17, 18]. Attempts were made to correct the perturbed embeddings with rigid [19] and nonrigid transformations [20, 14], but all assume that Laplacian eigenvectors are compatible between shapes. These methods are in fact inherently flawed by the instability of the eigendecomposition. The underlying graph metric may also be adapted by an expensive conformal metric correction [21]

Another issue is the eigenvectors' instability, such as, for example, the decomposition of a graph describing a circular shape, for which it is hard to establish the main axes of symmetry [83]. A solution for this was proposed, by enabling a transfer of geometrical properties across each surface instead of being directly matched [83].

Furthermore, one has to choose how many eigenmodes k are going to be used when establishing a correspondence, because there is a trade-off between computational time and robustness of the correspondence. However, Lombaert et al. (2012) showed that graph correspondences obtained through spectral matching become stable when considering $k \geq 5$ spectral coordinates [85]. This is essentially due to the large contribution of the low frequency components, compared to the high-order ones which only provide information about finer spatial details.

5.6 Summary

Spectral matching methods offer a fast alternative for surface and image registration. It represents a promising tool for matching shapes that have different levels of folding, but similar spectral representations, and thus they could be applied to the preterm population. This is also extended to other type of data, such as diffusion tensors and level set representations of shape boundaries, thus extending the spectral matching to images, which has not been investigated in much depth.

Chapter 6

Surface Spectral Matching for Cortical Development during the Preterm Period

In this chapter we use Joint-Spectral Matching for Surfaces, initialised with a Coherent Point Drift algorithm, to find a longitudinal correspondence between preterm and term equivalent white-grey matter boundary of the brain of 9 extremely preterm-born infants, described in Chapter 3, Section 3.2. This is extremely challenging since the brain undergoes significant chances in cortical folding, shape, surface area and volume. We then investigate whether matching different brain regions independently from one another influences the matching result. Using the determined point correspondence, we look at which regions undergo more folding of the white-grey matter boundary during the preterm period by using well-known curvature measures. We performed Hotelling T^2 statistics to evaluate the significance of our findings. The purpose of this study was to demonstrate that spectral matching can be used in the challenging problem of matching brains with different levels of folding, as in the case of the preterm infants, and to use this result to look at regions of gyrification.

Derived publications:

- **Orasanu, E.**, Melbourne, A., Cardoso, M.J., Lombaert, H., Kendall, G.S., Robertson, N.J., Marlow, N., Ourselin, S., Cortical folding of the preterm brain: a longitudinal analysis of extremely-preterm born neonates using spectral matching. Brain and Behaviour, 2016
- Melbourne, A.; Eaton-Rosen, Z.; **Orasanu, E.**; Price, D.; Bainbridge, A.; Cardoso, M. J.; Kendall, G. S.; Robertson, N. J.; Marlow, N., Ourselin, S. Longitudinal development in the preterm thalamus and posterior white matter; MRI correlations between Diffusion Weighted Imaging and T2 relaxometry. Human Brain Mapping: 37(7), 2479-2492, 2016
- **Orasanu, E.**, Melbourne, A., Lombaert, H., Cardoso, M.J., Kendall, G.S., Robertson, N.J., Marlow, N., Ourselin, S., Cortical folding of the preterm brain: a longitudinal analysis using spectral matching. Mind, Brain and Body Symposium, 2016
- Eaton-Rosen, Z., Melbourne, A., **Orasanu, E.**, Cardoso, M.J., Bainbridge, A., Kendall, G.S., Robertson, N.J., Marlow, N., Ourselin, S., Longitudinal measurement of the developing grey mat-

ter in preterm subjects using multi-modal MRI. Neuroimage, 111, 580-589, 2015

- **Orasanu, E.**, Melbourne, A., Lombaert, H., Cardoso, M.J., Johnsen, S., Kendall, G.S., Robertson, N.J., Marlow, N., Ourselin, S., Pre-frontal cortical folding of the preterm brain: a longitudinal analysis of preterm-born neonates. STIA Workshop (MICCAI), 2014

- Eaton-Rosen, Z., Melbourne, A., **Orasanu, E.**, Modat, M., Bainbridge, A., Cardoso, M.J., Kendall, G.S., Robertson, N.J., Marlow, N., Ourselin, S., Longitudinal measurement of the developing thalamus in the very-preterm brain using multi-modal MRI. In Medical Image Computing and Computer-Assistance Intervention (MICCAI) Conference, 2014. LNCS, 2014.

6.1 Methods

6.1.1 Infant Brain Segmentation and Parcellation

We segmented the structural T1-weighted brain scans of each infant into six different tissue classes: grey matter, white matter, cerebrospinal fluid (CSF), deep grey matter, cerebellum and brainstem, using a preterm specific Expectation-Maximization (EM) segmentation with prior relaxation, AdaPT, available in NiftySeg and described by Cardoso et al. (2013) [28]. Anatomical priors were first resampled in the same way as the brain masks from the same publicly available neonate brain atlas [79] after affine alignment with brain mask. Any segmentation errors were corrected by morphological operations (largest connected component and filling of the holes), as well as manual corrections when needed.

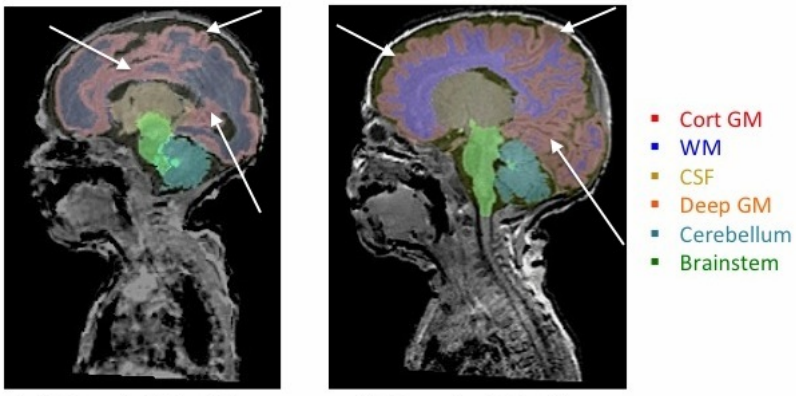

Figure 6.1: Original brain segmentation using publicly available anatomical priors and AdaPT. White arrows point to some regions that exhibit segmentation errors, mainly a confusion between white and grey matter, especially in areas with a higher degree of folding.

Using the priors from [79] (closest in age, in gestational weeks, to each individual subject) did not provide optimal results 6.1, so we bootstrapped the creation of a new atlas by using segmentation subsets. We initially manually corrected the resulting segmentations for three first timepoint scans and three second timepoint scans, each taking about 2-3 hours. We used these segmentations to create a database for the first and second timepoints. The two databases were then inputed into a Geodesic Information

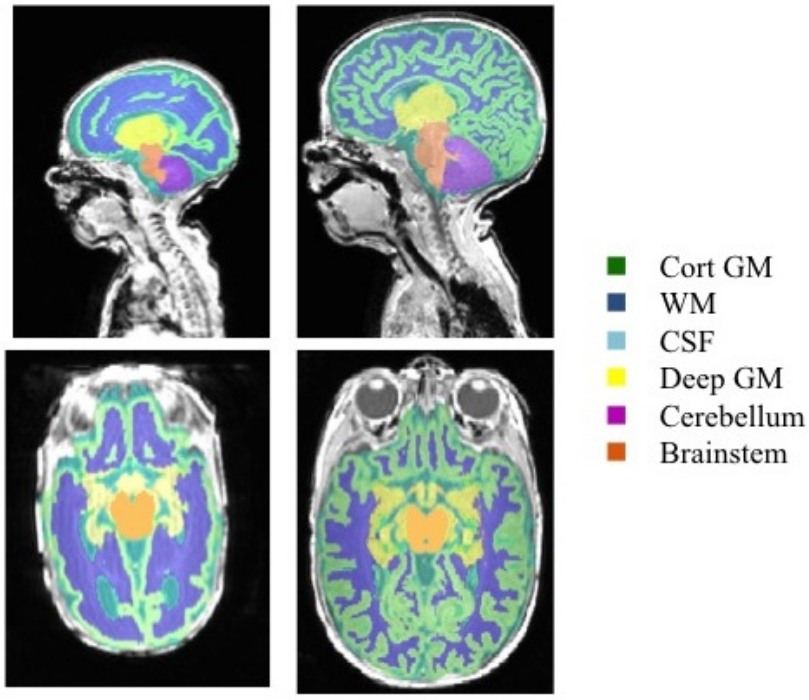

(a) 31 weeks EGA subject (b) 42 weeks EGA subject

Figure 6.2: Brain segmentation into grey matter (GM), white matter (WM), cerebrospinal fluid (CSF), deep grey matter, cerebellum and brainstem of infant ***c*** for the two different time points: 31 and 42 weeks EGA respectively.

Flow (GIF) scheme [29]. GIF contains two main steps: the first step included the creation of an atlas template from the database and used a weighted voting to get better anatomical priors, more similar to the subjects to be segmented; in the second step, it uses the newly created anatomical priors and AdaPT [28] to segment the new subjects. Each time a new subject segmentation was obtained, it was manually corrected again and added to its corresponding database (early or late timepoint). Each time a subject was added to the databases, less manual corrections were needed for new segmentations. Currently, each database contains about 30 subjects for each time point (some which did not have longitudinal information and are not part of the studies presented here), and currently only require minor manual corrections, taking about 2-3 minutes.

An example of the final brain segmentation for subject *c* is shown in Figure 6.2. The tissue segmentations obtained using the databases were also used in several other studies from others in our group (Eaton-Rosen et al. 2015 [49], Melbourne et al. 2016 [98], Eaton-Rosen et al. 2016 [47]).

To separate the the brain into different lobes and regions, we used a multi-contrast human neonatal brain atlas [107] registered to the space of the first and second scans of the infants, with brain masks, using non-rigid registration [101]. The multi-contrast human neonatal brain atlas [107] contains a total of 122 labels (Figure 6.3), and we grouped the labels corresponding to each region of interest: prefrontal cortex, temporal lobe, occipital lobe and parietal lobe. The corresponding regions were also then grouped by hemisphere: left and right.

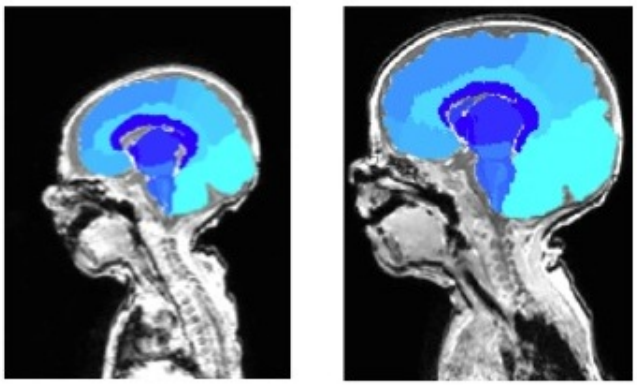

(a) 31 weeks EGA subject (b) 42 weeks EGA subject

Figure 6.3: Brain parcellation into different brain regions of infant $\boldsymbol{c}$ for the two different time points: 31 and 42 weeks EGA respectively.

6.1.2 Triangular-based meshes

Since in this study we are looking at the cortical folding, of particular interest is the white-grey matter boundary, which is typically used to study folding. Thus, the white matter segmentation was combined with the region parcellations to investigate this boundary (description of how this segmentations and labels are obtained is included in Section 6.1.1). Any segmentation errors were corrected by morphological operations (largest connected component and filling), as well as manual corrections when needed, to ensure a topologically correct surface. The processed left and right white matter region segmentations were used to create smooth triangle-based meshes of each surface using ITK-SNAP [173].

6.1.3 Longitudinal Joint-Spectral Matching of Cortical Surfaces

A rigid Coherent Point Drift (CPD) algorithm at the centre of the mesh is used to find an initial correspondence for the two surfaces to be matched [104]. CPD is preferable to the Feature Oriented Correspondence using Spectral Regularisation (FOCUSR) used by [85], since we optimise for a rigid transformation, rather than a non-rigid one, resulting in a simpler and more efficient optimisation. Furthermore, CPD is more stable regarding the ordering of the eigenvectors [115]. An example of improvement in the spectral matching of the prefrontal cortex by using a CPD initialisation is shown in Figure 6.4.

After an initial correspondence was computed, Joint-Spectral Matching (JSM) [87] was used to find the correspondence for the two surfaces. JSM builds a dual-layered graph, where layers correspond to the cortical surface of each subject, and correspondence links, found from the initial intra-subject matching, connect both layers. This joint approach of connected surfaces produces a set of shared eigenmodes and, thus, a shared parameterisation of the surfaces. A final correspondence is then defined using a nearest-neighbour search on the spectral representations.

The meshes we want to match are very different in size, shape and morphology, and classical non-linear registration approaches fail in accounting for the large deformations taking place. However their representations in the spectral domain have a less complex topology, with the low frequency eigenvectors

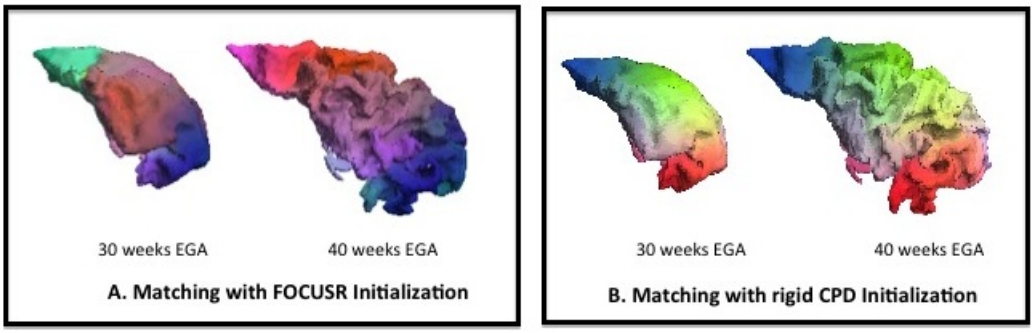

Figure 6.4: Initialisation using FOCUSR with a wrong eigenvector ordering gives a poor PFC correspondence (A). We use a method not prone to such issues, such as a rigid CPD (B).

of the surface at term resembling the low frequency eigenvectors of the preterm cortical surface, making the two surfaces comparable and easier to map a correspondence between them using a nearest-neighbour search ([87]).

The algorithm process is summarised in Figure 6.5.

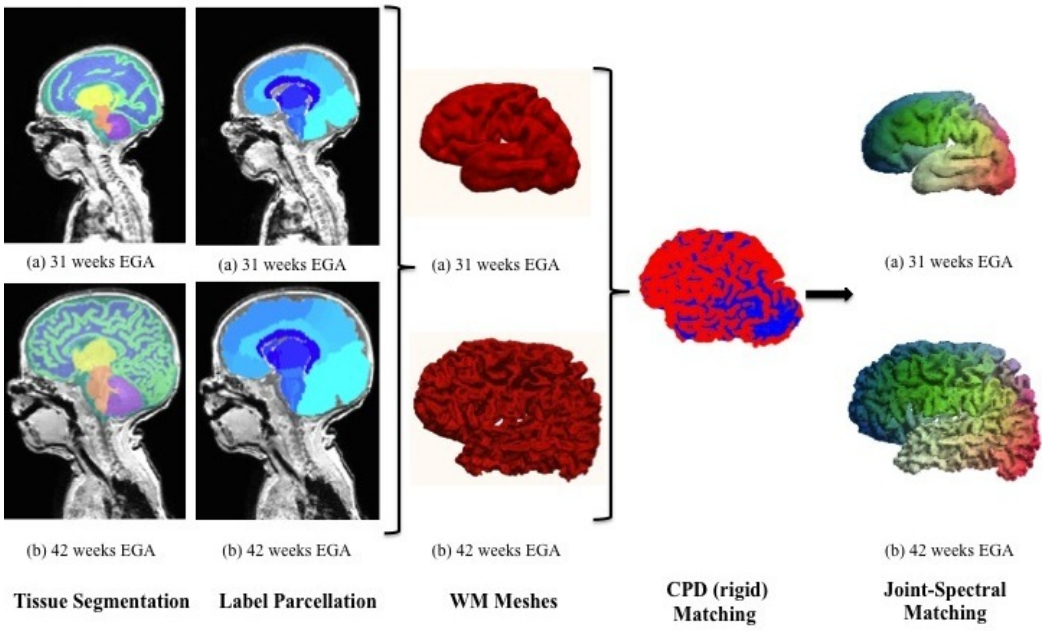

Figure 6.5: The spectral matching algorithm. After preterm-specific segmentation, meshes of the left hemispheres are defined for the 31 and 42 week time points of infant *c*. After a rigid alignment at the centre of the mesh using Coherent Point Drift initialisation is performed, a mesh correspondence is defined by Joint-Spectral Matching (spectral matching colour-coded anterior-posterior).

6.1.4 Consistency of surface matching

We compared the obtained correspondence of the intra-subject PFC, temporal, occipital and parietal meshes, respectively, with a whole-brain white matter intra-subject correspondence in all subjects, in order to check the cortical surface matching consistency and how it is influenced by the quality of the meshes. For each vertex that existed in both the whole brain and regional meshes at scan 1, the mismatch

was computed by calculating the Euclidean distance of the corresponding vertices, defined by the spectral matching, in the regional and whole brain mesh at scan 2.

6.1.5 Measurement of longitudinal development

To quantify the early cortical folding, we looked into measures of surface curvature, which intrinsically describe the local shape of the respective surface [32]. We computed the principal curvatures κ_1 and κ_2 for each vertex of the surface mesh, by using the Meusnier and the Euler theorem [32], [44] (see Figure 6.6). From the principal curvatures we derived several measures of surface curvature: mean curvature (M), Gaussian curvature (G), shape index (S) and curvedness (C), given by the equations below.

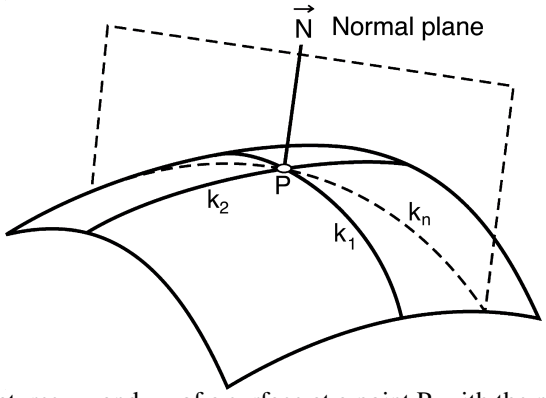

Figure 6.6: Principal curvatures κ_1 and κ_2 of a surface at a point P, with the normal plane to the surface at point P.

$$\text{Mean Curvature:} \qquad M = \frac{1}{2}(\kappa_1 + \kappa_2) \tag{6.1.1}$$

$$\text{Gaussian Curvature:} \qquad G = \kappa_1 \cdot \kappa_2 \tag{6.1.2}$$

$$\text{Shape index:} \qquad S = \frac{2}{\pi} \cdot \arctan(\frac{\kappa_1 + \kappa_2}{\kappa_1 - \kappa_2}) \tag{6.1.3}$$

$$\text{Curvedness:} \qquad C = \sqrt{\kappa_1^2 + \kappa_2^2} \tag{6.1.4}$$

Additionally, we computed the bending energy E ([72]), which is intuitively dependent on the local surface area change. The change in the bending energy, over time and over area, describes the energy needed to deform that area, which may be able to provide localised information about the mechanical properties of the underlying tissue:

$$\frac{\partial E}{\partial t} = \frac{\partial}{\partial t} \int ({\kappa_1}^2 + {\kappa_2}^2) dA \tag{6.1.5}$$

To investigate the longitudinal brain development for each subject, we mapped the 40 weeks surfaces to the 30 weeks surfaces using JSM and computed the change of the surface parameters at each vertex of the mesh. The longitudinal change in the parameters (M, G, E) can be computed by measuring the change between the parameter value at any given point on one surface and its corresponding point on the other surface, while correcting for volume and surface area differences.

To have comparable measures of curvature for all brain meshes at different EGA, the values have to be corrected for enclosed mesh volume. The volume of each white matter mesh was computed as the sum of all voxels from each segmentation, which was then multiplied by the voxel dimension provided by the scanner. The values for the mean and Gaussian curvatures were then corrected for brain volume by dividing each value by the cube root of the ratio of the subject's white matter mesh volume and mean white mesh matter volume of the 30 and 40 week EGA [8].

The difference in total curvature (sum of squared principal curvatures) was corrected by taking into account the local area change between the 30 and 40 weeks subjects used to obtain the bending energy. We estimated the surface area of the meshes by calculating the sum of the triangles areas. By using the correspondence between the areas, a local measurement of surface area change can be defined [115]. Then the total curvature value at each vertex in the 40 week mesh was divided by the local area change at that vertex and then mapped into the space of the 30 week mesh, where it was multiplied by the local area change in the 30 week mesh.

6.1.6 Longitudinal Differences: Group Analysis

We performed a group analysis to look at the significance of the folding changes during the preterm period. We selected one reference infant and for each time point and hemisphere we mapped, using JSM initialised by CPD, all other infants, by time point and hemisphere [138]. The mappings were used to create mean shapes for the two time points. Morphological changes between the two time points were investigated after another step of JSM with a CPD initialisation. Differences in shape represent differences in cortical folding: the more different two shapes are, the more difference there is in the degree of folding. We used the Hotelling T^2 two sample metric to derive a local group shape difference metric and local statistical p-values for all corresponding points [144]. Groupwise shape analysis using spectral matching has previously been shown to give reliable results [138].

6.2 Results

6.2.1 Joint-Spectral Matching Correspondence

We found a good qualitative point correspondence for all 9 subjects between 30 and 40 week white-grey matter boundary meshes of both left and right hemisphere, PFC, temporal, occipital and parietal lobe of all subjects. The first 5 spectral modes (Figure 6.7) for infant c are shown below and describe variation of shape in the spectral domain, features that were optimised in order to find a surface correspondence. We notice that although the two shapes are different in Cartesian coordinates, they are very similar in

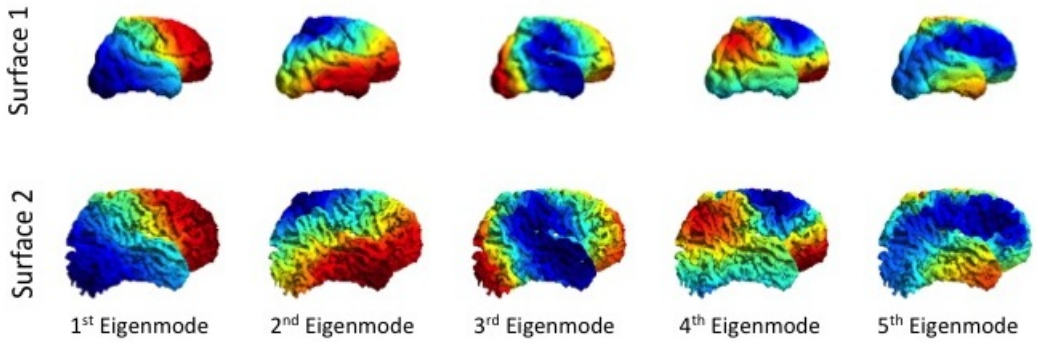

Figure 6.7: The first 5 spectral modes of infant c for two different time points: 31 and 42 weeks EGA respectively. Although the meshes are quite different in cartesian space, they have similar representations in the spectral domain.

the spectral domain, since low-frequency spatial features between infants at different time-points are similar and advanced secondary and tertiary gyrification is represented by high frequency information [146].

6.2.2 Consistency of surface matching

The surface matching obtained by individually matching the prefrontal cortex and temporal lobe and matching the entire brain did not have significant variations. The PFC mean average distance mismatch for all infants was $1.46 \pm 0.96mm$ for the left hemisphere and $1.91 \pm 1.28mm$ for the right hemisphere. The temporal lobe mean average distance mismatch among all infants was $2.63 \pm 1.40mm$ and $2.78 \pm 1.34mm$ for the left and right hemispheres, respectively. Furthermore, the occipital lobe had a mean average distance mismatch among all infants of $2.54 \pm 1.52mm$ and $2.47 \pm 1.52mm$ for the left and right hemispheres, respectively, while for the parietal lobes the values were $2.63 \pm 1.53mm$ and $2.85 \pm 1.59mm$ for the left and right hemispheres, respectively.

Example maps of these variations in all regions are shown in Figure 6.8.

6.2.3 Longitudinal brain development over the preterm period

Whole-Brain Figure 6.9 shows an example of maps of mean curvature for the white-grey matter boundary of subject c scanned at 31 weeks and 42 weeks EGA. The maps of mean curvature change in 31 weeks space (Figure 6.9 (d)) show the apparent locations where the secondary and tertiary sulci and gyri will be formed, as well as how the primary sulci and gyri, will develop. The regions that indeed exhibit the most folding are the prefrontal cortex and the temporal lobes.

Prefrontal cortex Figure 6.11 shows an example of maps of mean curvature for the prefrontal cortex white-grey matter boundary of subject c scanned at 31 weeks and 42 weeks EGA. The maps of mean curvature change in 31 week space (Figure 6.11 (d)) show the apparent locations where the secondary and tertiary sulci and gyri will be formed especially in the middle and inferior region. Furthermore, we notice the development of the already existing primary sulci and gyri, like the middle frontal gyrus.

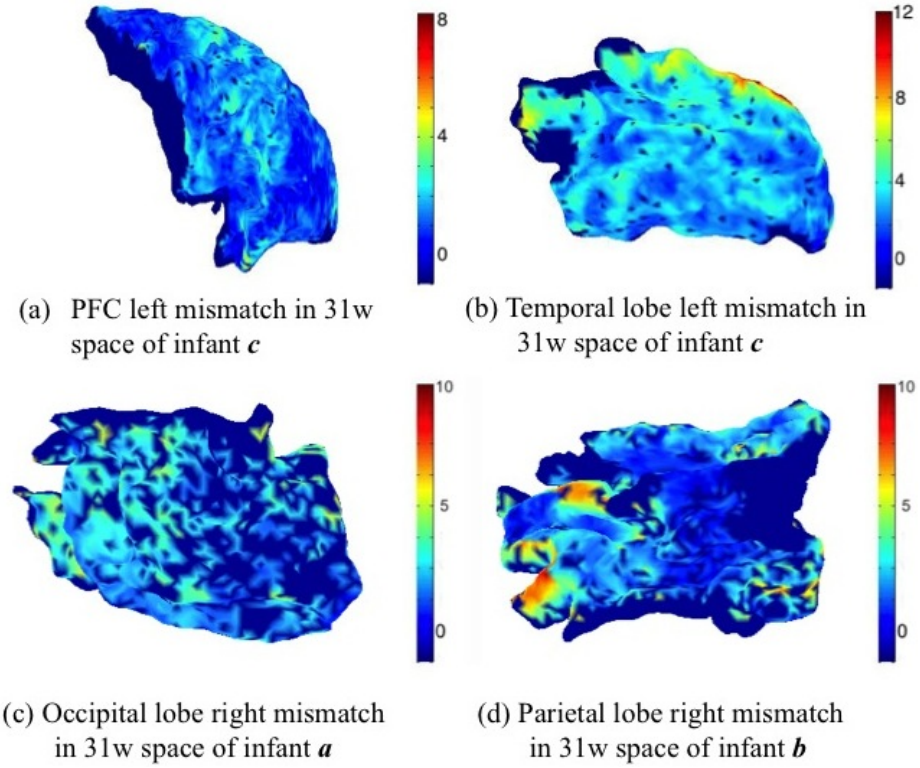

(a) PFC left mismatch in 31w space of infant ***c***

(b) Temporal lobe left mismatch in 31w space of infant ***c***

(c) Occipital lobe right mismatch in 31w space of infant ***a***

(d) Parietal lobe right mismatch in 31w space of infant ***b***

Figure 6.8: Example maps of mismatching variation between the whole brain matching and regional spectral matching correspondences (units are in mm). Vertices that are not represented in both individual and whole brain meshes were attributed a value of -1 (represented with dark blue).

These changes are commensurate with [33]. We note that the Gaussian curvature is very sensitive to the geometric errors on the white-grey matter interface and thus not as reliable and useful a feature for cortical surface analysis as the mean curvature (Figure 6.12).

As described above in 6.1.5, the bending energy depends on both the total curvature difference and the change in local surface area. The inferior prefrontal cortex undergoes more local surface area change compared to the superior prefrontal cortex, which undergoes almost no change (Figure 6.13 (c)). This is consistent with the observation that superior PFC development and folding is largely complete before 31 weeks [33].

Temporal lobe Similarly, Figure 6.14 shows an example of maps of mean curvature for the left temporal lobe white-grey matter boundary for the same subject *c* scanned at 31 weeks and 42 weeks EGA. The maps of mean curvature change in 31 weeks space indicate the likely further development of the primary gyri and sulci and emergence of most of the secondary and tertiary gyri and sulci. Probably the most striking is the evolution of gyri and sulci around the transverse temporal gyrus, situated across the 'middle' part of the temporal lobe, since this gyrus becomes definite much later than other primary gyri, around 31 weeks of gestation. Although this gyrus is visible in the early scan, all secondary and tertiary gyri surrounding it emerge during the preterm period. These changes are, again, commensurate with [33].

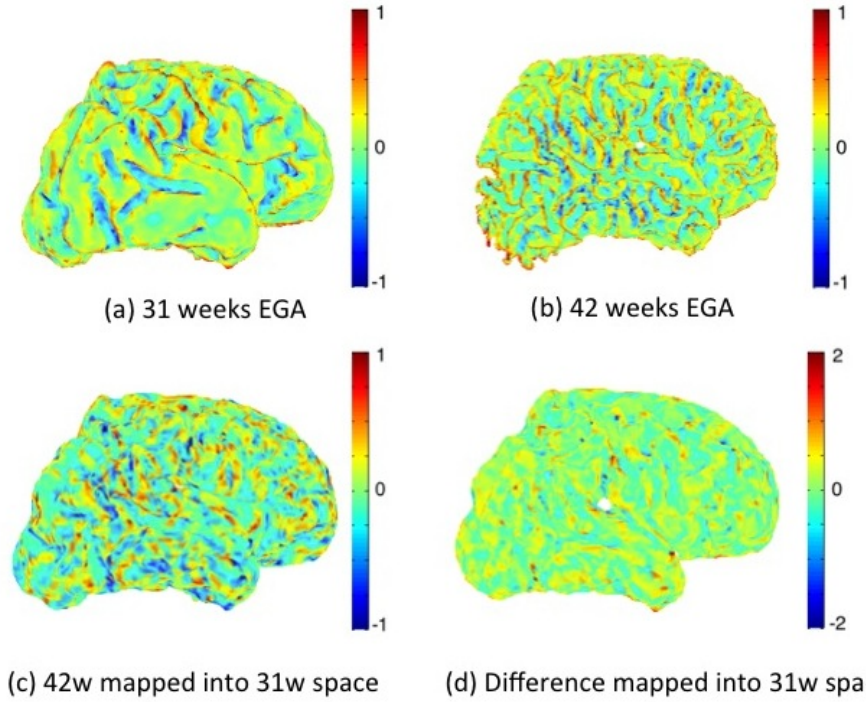

Figure 6.9: Maps of mean curvature of whole brain white-grey matter boundary (left) for infant *c* scanned at 31 weeks (a) and 42 weeks (b) EGA. Positive values (red/yellow) represent gyri (convex structures) and negative values (blue) represent sulci (concave structures). The Joint-Spectral Matching correspondence allows us to map mean curvatures from 42 week to 31 week space (c) and compute the changes in mean curvature between these two time points in 31 weeks space (d).

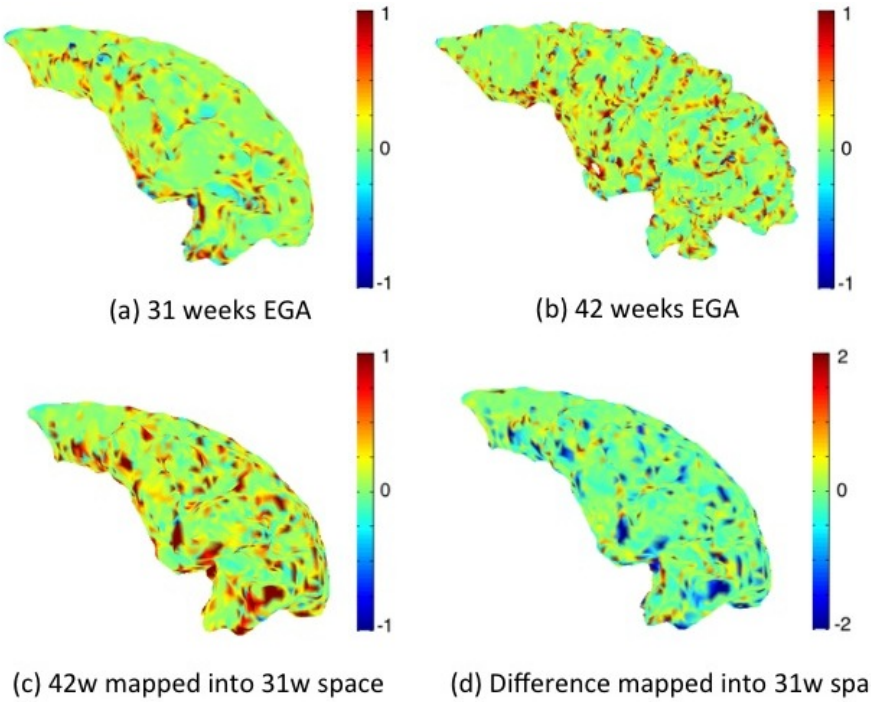

Figure 6.10: Maps of Gaussian curvature of the grey-white matter boundary of the prefrontal cortex (left) for infant *c* scanned at 31 weeks (a) and 42 weeks (b) EGA. It can be seen that the Gaussian curvature is more sensitive to geometric erros of the meshes and noisier than the mean curvature maps.

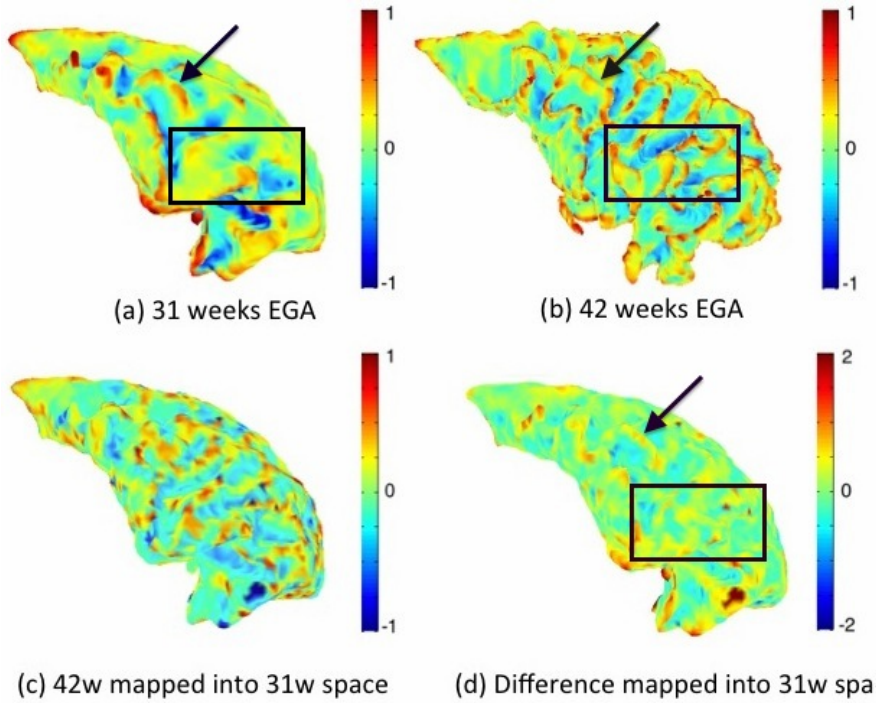

Figure 6.11: Maps of mean curvature of the grey-white matter boundary of the prefrontal cortex (left) for infant *c* scanned at 31 weeks (a) and 42 weeks (b) EGA. Positive values (red/yellow) represent gyri (convex structures) and negative values (blue) represent sulci (concave structures). The Joint-Spectral Matching correspondence allows us to map mean curvatures from 42 week to 31 week space (c) and compute the changes in mean curvature between these two time points in 31 weeks space (d). The difference map of the mean curvature over the preterm period indicates the further development of several primary gyri and sulci, like the middle frontal gyrus (indicated by the black arrow), as well as regions where secondary and tertiary sulci will emerge (black square).

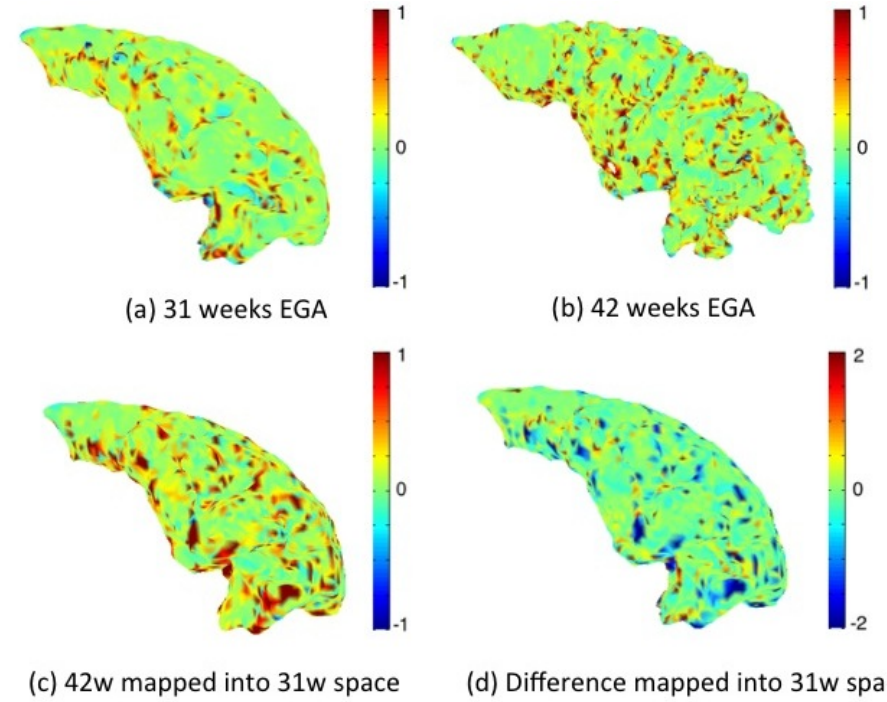

Figure 6.12: Maps of Gaussian curvature of the grey-white matter boundary of the prefrontal cortex (left) for infant *c* scanned at 31 weeks (a) and 42 weeks (b) EGA. It can be seen that the Gaussian curvature is more sensitive to geometric erros of the meshes and noisier than the mean curvature maps.

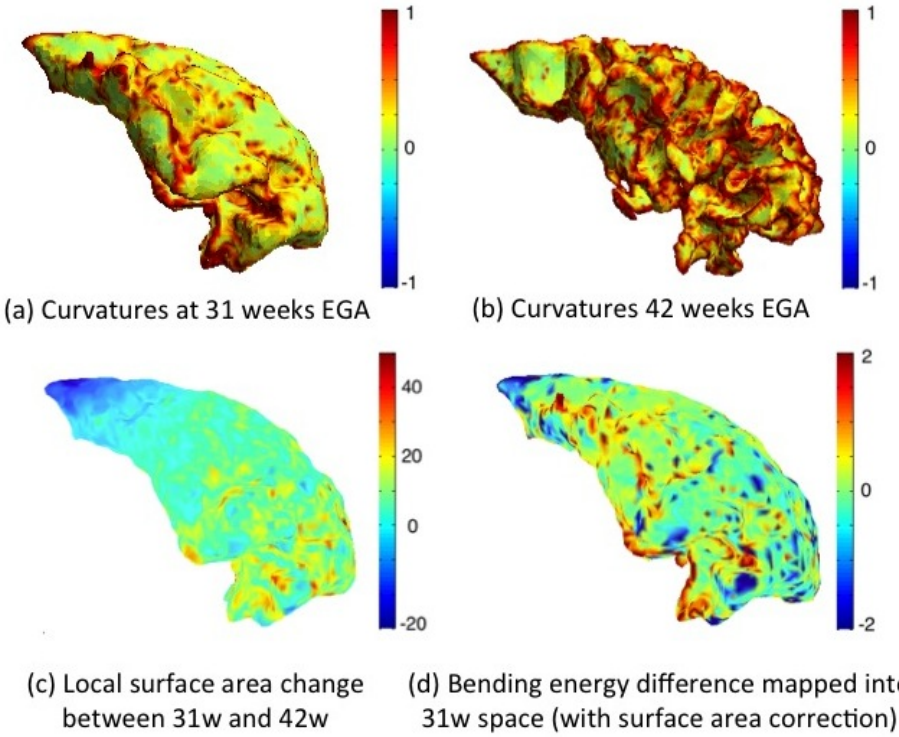

Figure 6.13: Total curvature of the white-grey matter boundary of the prefrontal cortex (left) shown for infant *c* at 31 weeks (a) and 42 weeks (b) EGA, local surface area change between the two time points (c) and computed bending energy (d). Positive values (red) in the bending energy represent regions of gyrification and negative values (blue) represent regions of sulcation.

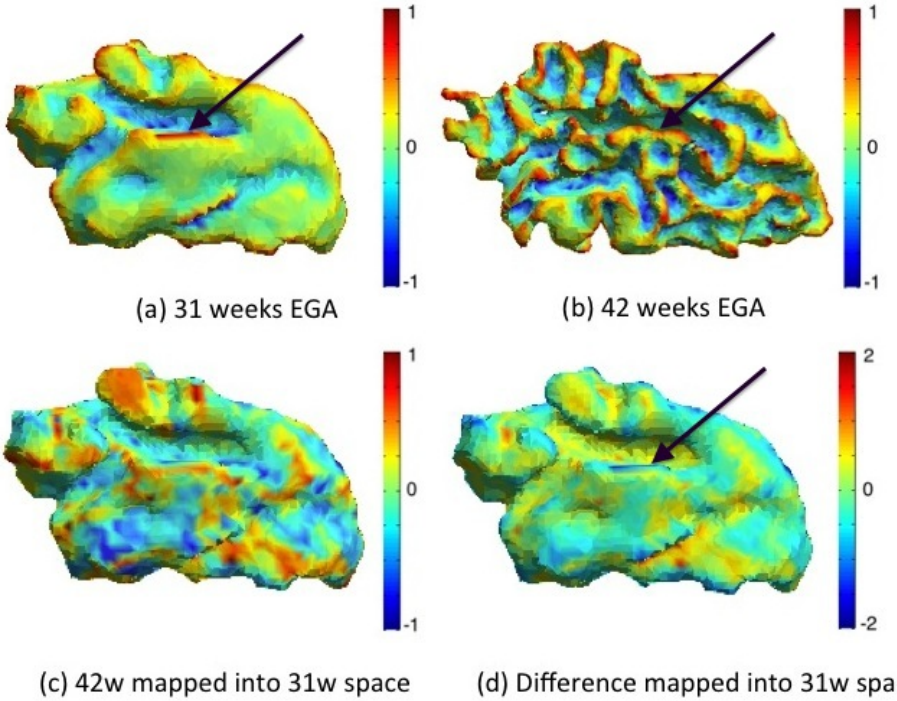

Figure 6.14: Maps of mean curvature of the grey-white matter boundary of the temporal lobe (left) for infant *c* scanned at 31 weeks (a) and 42 weeks (b) EGA. Positive values (red/yellow) represent gyri (convex structures) and negative values (blue) represent sulci (concave structures). The Joint-Spectral Matching correspondence allows us to map mean curvatures from 42 week to 31 week space (c) and compute the changes in mean curvature between these two time points in 31 weeks space (d). The black arrow indicates the transverse temporal gyrus, which becomes definite around 31 weeks of gestation and therefore all other secondary and tertiary gyri surrounding it will emerge during the preterm period.

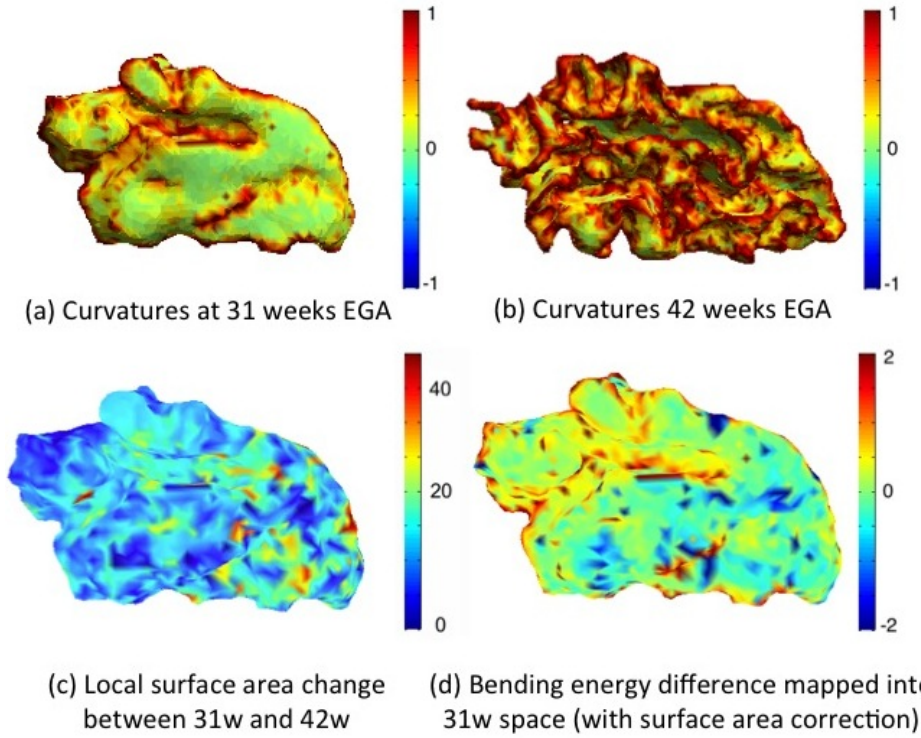

Figure 6.15: Total curvature of the white-grey matter boundary of the temporal lobe (left) shown for infant *c* at 31 weeks (a) and 42 weeks (b) EGA, local surface area change between the two time points (c) and computed bending energy (d). Positive values (red) in the bending energy represent regions of gyrification and negative values (blue) represent regions of sulcation.

The map of local surface area change (Figure 6.15 (c)) shows that the frontal region of the temporal lobe, especially around the transversal gyrus expands the most. The maps describing the bending energy required for the cortical folding development of the temporal lobe in the preterm period may be linked to the mechanical deformation required for the folding of the cortex.

Occipital and Parietal Lobes Similarly, Figure 6.16 shows an example of maps of mean curvature for the occipital and parietal lobes white-grey matter boundary for the same subject *c* scanned at 31 weeks and 42 weeks EGA. The maps of mean curvature change in 31 weeks space (Figure 6.16 c and f) do show that there does not seem to be any appearance of new gyri or sulci during the preterm period for these regions and only the existing features continue to develop, as described by [33].

Longitudinal brain development over the preterm period in all infants We investigated the change in surface area as function of equivalent gestational age. Across all infants, the surface area for all individual regions and both hemisphere increases linearly with equivalent gestational age ($R^2 > 0.88$). The rates of change in surface area per week for each region, by hemisphere, are summarised in Table 6.1. We also report that the volume increase as a function of GA is not linear ($R^2 > 0.85$).

The mean curvature maps appeared to be the most reliable curvature measure, since gyrification and sulcation patterns can be clearly observed in each subject for both prefrontal cortex and temporal lobe. Therefore, to examine the variation in developmental pattern between 30 and 40 GW, we show the change

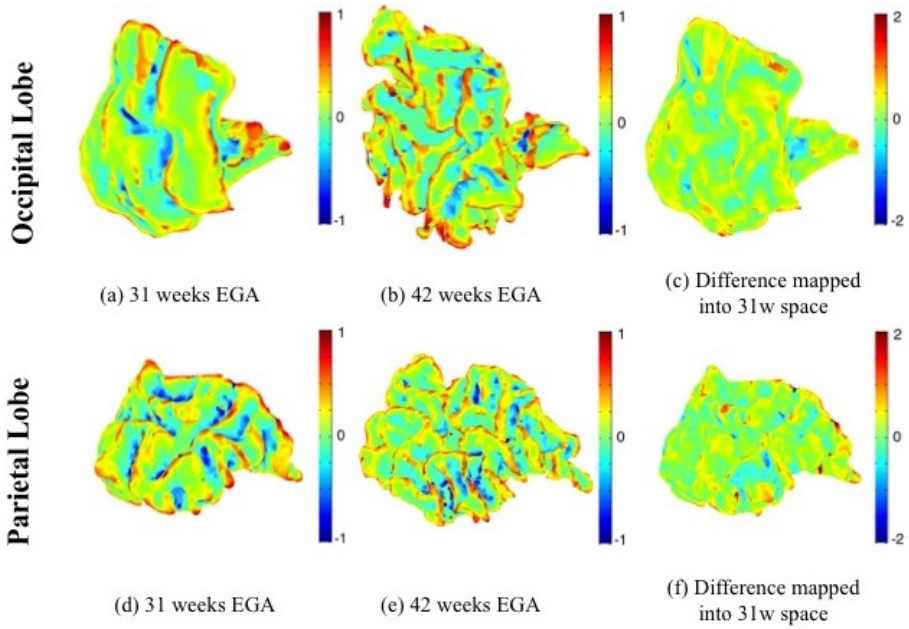

Figure 6.16: Maps of mean curvature of the grey-white matter boundary of the left occipital lobe (upper row) and left parietal lobe (bottom row) for infant *c* scanned at 31 weeks (a and d) and 42 weeks (b and e) EGA. Positive values (red/yellow) represent gyri (convex structures) and negative values (blue) represent sulci (concave structures). The Joint-Spectral Matching correspondence allows us to map mean curvatures from 42 week to 31 week space and compute the changes in mean curvature between these two time points in 31 weeks space (c and f). It can be noticed that most differences (c and f) appear on already existing gyri and sulci since most of them are already formed by the time of the first scan.

Table 6.1: Surface area increase as a function of equivalent gestational age in 9 preterm born infants, scanned both at early (31.6 weeks EGA) and term-equivalent age timepoints (41.7 weeks EGA)

	Linear Increase in Left Hemisphere White Matter (cm^2/week)	Linear Increase in Right Hemisphere White Matter (cm^2/week)
Whole Brain	$26.23(R^2 = 0.96)$	$25.79(R^2 = 0.97)$
Prefrontal Cortex	$6.00(R^2 = 0.98)$	$6.21(R^2 = 0.94)$
Temporal Lobe	$3.44(R^2 = 0.97)$	$3.20(R^2 = 0.94)$
Occipital Lobe	$3.86(R^2 = 0.90)$	$3.77(R^2 = 0.88)$
Parietal Lobe	$5.80(R^2 = 0.97)$	$5.59(R^2 = 0.96)$

in mean curvature maps for all seven infants across all regions investigated.

Figure 6.17 shows development of primary sulci and gyri and the emergence of secondary and tertiary gyri and sulci mapped onto the meshes from the early scan of each infant. Results are consistent with infant c. Variation in these images is introduced by three main factors: 1. inter-subject variability; 2. the gestational age of the infant; and 3. the temporal gap between the two scans (the infants were not scanned at the exact same two time points). For example, it is noticeable how infant e (scanned around 29 weeks and 46 weeks EGA) shows more changes in mean curvature in both prefrontal cortex and temporal lobe than infant g (scanned around 31 weeks and 38 weeks EGA). There seems to be an asymmetry between the left and right hemisphere in both prefrontal cortex and temporal lobes, the latter one showing less change during the preterm period, consistent with other observations [33].

The developmental changes in all infants of the mean curvature of the parietal and occipital lobe are shown in Figure 6.18. It can be seen, as expected, that there are less changes in these two lobes than in the prefrontal cortex or temporal lobe, and that most of these changes occur on already existent gyri and sulci, with almost no appearances of new secondary and tertiary gyri and sulci.

Longitudinal Differences: Groupwise Analysis Figure 6.19 shows the corresponding p-values of the differences in cortical folding between the two time points for each vertex, mapped on the mean early scan. We noticed that the regions with statistically significant difference between the two time points (p-value< 0.05) are the left and right prefrontal cortex (the middle and lower regions) and the left temporal lobe (the region surrounding the transversal temporal gyrus), the same regions where we noticed differences in the longitudinal data for individual infants.

6.3 Discussion

We used joint-spectral matching techniques to find an intra-subject correspondence between the white-grey matter boundary of 9 extremely preterm infants scanned shortly after birth, around 30 weeks EGA, and at term equivalent age, around 40 weeks EGA. We then verified if using smaller meshes for individual regions rather than the whole brain returns consistent correspondences. Finally, we investigated the change in well-known measures of surface curvature such as the mean curvature to look at the regions that undergo the most cortical folding during this crucial period, as well as the significance of these changes.

The intra-subject white matter meshes are very different in size, shape and cortical folding, resulting in the failure of non-linear registration techniques. The spectral shape representations however, denoted by their first 5 spectral components or modes of vibration, are very similar (see Figure 6.7) thus JSM provides a very good qualitative correspondence. JSM was initialised using a rigid CPD correspondence, since it provides a more robust alignment for meshes that are so different, compared to FOCUSR. This novel method has much potential for the assessment of development in the preterm brain [115], [167], [109].

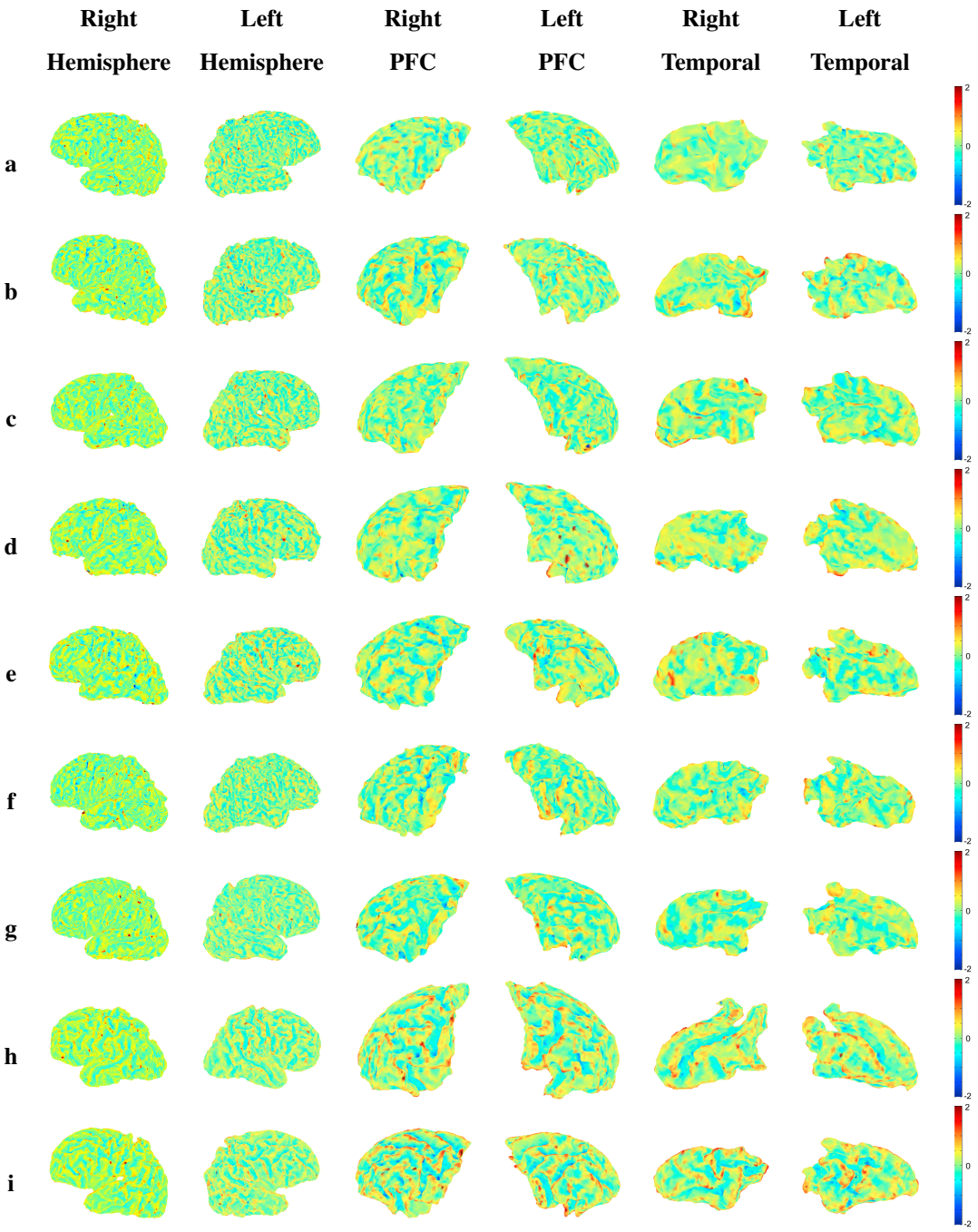

Figure 6.17: Changes of the intra-subject mean curvature mapped into the earlier scan using Joint-Spectral Matching for all 9 infants. For each infant (a-i) we show the mean curvature changes of the regions we looked at: right hemisphere (first column), left hemisphere (second column), prefrontal cortex right hemisphere (third column), prefrontal cortex left hemisphere (fourth column), temporal lobe right hemisphere (fifth column) and temporal lobe left hemisphere (sixth column). Positive values (red/yellow) represent gyri (convex structures) and negative values (blue) represent sulci (concave structures).

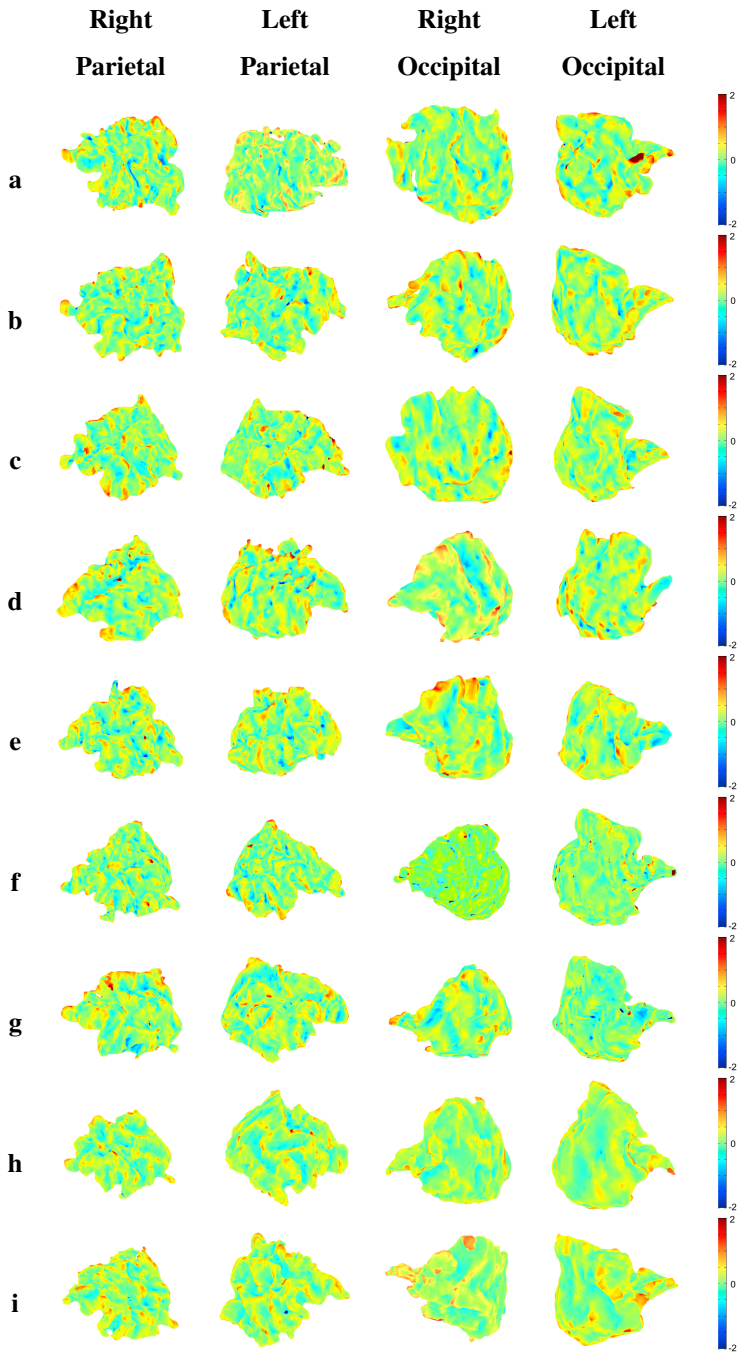

Figure 6.18: Changes of the intra-subject mean curvature mapped into the earlier scan using Joint-Spectral Matching for all 9 infants. For each infant (a-i) we show the mean curvature changes of the regions we looked at: right parietal lobe (first column), left parietal lobe (second column), right occipital lobe (third column), left occipital lobe (fourth column). Positive values (red/yellow) represent gyri (convex structures) and negative values (blue) represent sulci (concave structures).

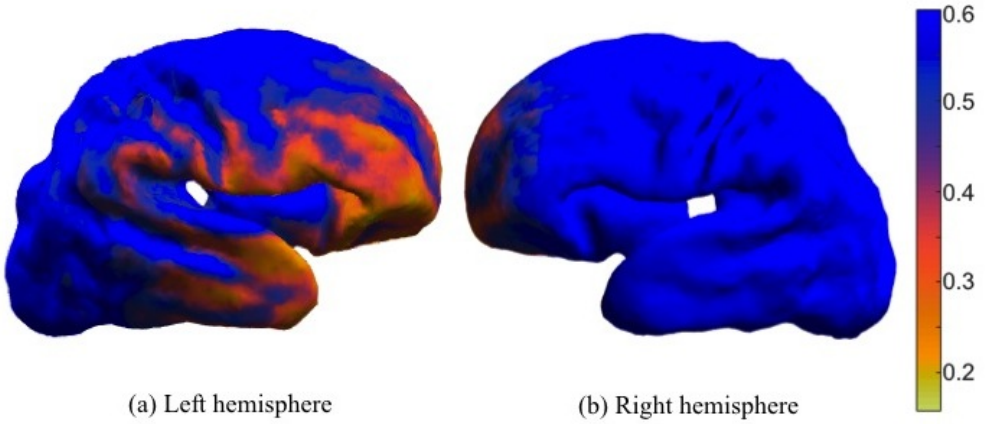

Figure 6.19: Statistical maps of longitudinal differences during the preterm period in 9 infants of the left and right hemisphere. The p-values are described by the colour bar.

The maps of surface matching variation as well as the average inconsistency between the different spectral matches of the same regions show that the correspondences determined from the spectral matching are quite consistent. The variations of the prefrontal cortex matching are smaller than those of the other lobes. The larger matching inconsistencies are usually situated at the boundaries of the region's mesh, since, when finding a correspondence for a smaller region of the brain, there is no additional information about the shape of the surrounding neighbouring regions to further guide the matching.

We investigated the cortical folding by looking at the change in mean curvature in the prefrontal cortex, temporal, occipital and parietal lobe. The uniqueness of the application motivated us to choose well-known measures of curvature and cast these as measures of longitudinal change in the individual. We also examined the bending energy because it may provide information about the underlying tissue deformation and can be interpreted directly as a measurement of change in the infant folding pattern. Looking at the maps of changes in mean curvature for all selected regions in all infants, we did notice how the prefrontal cortex and temporal lobe develop more new gyri and sulci than the occipital and parietal lobe during this preterm period.

Finally, we performed a groupwise analysis where we created a mean shape of the early and late time point of all infants. By performing Hotelling T^2 statistics, we noticed that regions of significant shape difference and gyrification, and thus folding differences, are the left temporal lobe, especially the regions around the transverse temporal gyrus, and the left and right prefrontal cortex, the inferior and middle regions (p-value< 0.5). These results are consistent with our initial expectations that these regions develop mostly in the third trimester of pregnancy; hence they might be affected by preterm birth. Furthermore, we noticed a left-right asymmetry, with the left hemisphere undergoing more changes than the right hemisphere. The right temporal lobe does not show statistically significant changes during this time period. The right temporal lobe is also known to develop two weeks earlier than the left temporal lobe, hence it may not be affected by preterm birth. Dubois et al. (2008) also found a right-before-left development of the superior temporal sulcus during the preterm period [46]. Previous studies have also found abnormalities in the white and grey matter of temporal and frontal lobes, in other preterm cohorts,

such as volume reduction [51], [54], usually correlated with neurological deficits, poor executive function and language deficits.These results are consistent with our findings, thus further confirming that the prefrontal cortex and temporal lobe are affected by preterm birth, and functions correlated with these two lobes are likely to be affected. Future work will look into the neurological outcome of the infants, more specifically in the outcome related to these two regions (language, executive function) and correlations with the shape analysis presented here.

The main limitation of our study is that, although qualitatively we obtained a very good correspondence for the intra-subject prefrontal cortex and temporal lobe, it is very difficult to validate this cortical matching, since the data is novel and there is no proper way of establishing a ground truth. Manual validation by a trained neuroanatomist could be used for validation, but it would be restricted to the most obvious anatomical landmarks. Another limitation can also be the age range of our subjects, however, the size of our meshes were corrected for when looking at the changes, as described in section 6.1.5.

Generating accurate correspondences between the intra-subject brain white matter at multiple time points enables us to measure the longitudinal changes that take place in this region in preterm infants. These measures may contribute to developing early biomarkers for predicting executive and motor development. This type of research might begin to illuminate the debate on the mechanical role of tissue growth on the observed cortical folding pattern, information that is only measurable in fetal and neonatal cohorts of this type.

Due to the success of spectral techniques on matching cortical surface with different morphology, they could be also used to study shape differences between cohorts with any type of pathology (e.g. dementia subjects, subjects with ADHD, preterm subjects) and matched controls. Furthermore, spectral representations could be extended to describe image data such as surface boundaries or diffusion to develop further spectral-based registration techniques for longitudinal data when large changes are taking place, like in the case of the preterm population.

Chapter 7

Surface Spectral Matching for Shape Analysis in the Epicure Data

In this chapter, we use JSM to investigate the structural group differences between young adults born extremely preterm and their term-born peers, described in Chapter 3, Section 3.3. In particular, we look at thalamic and cerebellar shape and cerebral folding differences between the two groups. Shape analysis of brain structures is of increasing interest to the neuroimaging community, as it can precisely locate morphological changes between healthy and pathological structures. Local differences in the thalamus and folding might increase the understanding of the psychological outcome in this type of cohort. Furthermore, they can give us information on the long-term structural impact of extreme prematurity. To the best of our knowledge, this is the first study to investigate the long term impact of prematurity on the thalamic and cortical shapes.

Abnormal gyrification patterns have been associated with cognitive-behavioural deficits among preterm born subjects [75]. Previous studies have shown differences in cortical folding between preterm and term born infants [51], [10]). The thalamus is an important part of the brain, and alterations of the thalamic structure are likely to cause disruption in the thalamic-cortical-thalamic circuitry that can negatively affect cognitive performance. It has been shown that the size and structure of the thalamus are affected by preterm birth [18],[10]. Atrophy of the thalamus has been seen in association with damage of the white matter [125], [105]. The thalamus is particularly vulnerable after preterm birth, especially in association with white matter pathology, as seen from deformation-based morphometry studies [17]. The cerebellum is responsible for motor coordination, but recently cerebellar disorders have been shown to be correlated also with poor planning abilities, deficits in shifting attention, verbal fluency, memory and learning [137]. There has been much interest into how the cerebellum is affected by prematurity. Shah et al. (2006) found a correlation between reduced cerebellar volume and presence of white matter injury in preterm infants scanned at term, although there was no evidence for a correlation between prematurity and primary impairment in cerebellar development [137]. Parker et al. (2008) found a reduction in cerebellar volumes in very preterm individuals between adolescence (15 years old) and young adulthood (19 years old), correlated with self-reported wellbeing [123].

We hypothesise that the thalamic, cerebellar and white matter abnormalities due to preterm birth may persist into adulthood, and thus motivating the work done in this chapter.

Derived publications:

- **Orasanu, E.**, Melbourne, Atkinson, D., Beckmann, J., Marlow, N., Ourselin, S., Shape analysis of the thalamus and cortical folding patterns in extremely preterm born young adults. *Submitted to Human Brain Mapping*, 2017
- **Orasanu, E.**, Melbourne, A., Eaton-Rosen, Z., Atkinson, D., Lawan, J., Beckmann, J., Marlow, N., Ourselin, S., Local shape analysis of the thalamus in extremely preterm born young adults. ISMRM, 2016
- **Orasanu, E.**, Melbourne, A., Eaton-Rosen, Z., Atkinson, D., Saborowska, A., Beckmann, J., Marlow, N., Ourselin, S., Cortical folding patterns in extremely preterm born young adults. ISMRM, 2016
- Eaton-Rosen, Z., Melbourne, A., **Orasanu, E.**, Beckmann, J., Stevens, N., Atkinson, D., Marlow, N., Ourselin, S., White matter alterations in young adults born extremely preterm: a microstructural point of view. ISMRM, 2016
- Melbourne, A., **Orasanu, E.**, Eaton-Rosen, Z., Manuel J Cardoso, Beckmann, J., Smith, L., Atkinson, D., Marlow, N., Ourselin, S., Analysis of brain volume in a 19 year-old extremely- preterm born cohort. ISMRM, 2016
- Melbourne, A., Eaton-Rosen, Z., **Orasanu, E.**, Beckmann, J., Saborowska, A., Atkinson, D., Marlow, N., Ourselin, S., Perfusion and diffusion in the extremely preterm young adult thalamus. ISMRM, 2016
- Melbourne, A., **Orasanu, E.**, Eaton-Rosen, Z., Beckmann, J., Saborowska, A., Atkinson, D., Marlow, N., Ourselin, S., Characterizing microstructure and shape of the extremely preterm 19 year-old corpus callosum. ISMRM, 2016
- Dingwall, N., Chalk, A., Martin, T.I., Scott, C.J., Semedo, C., Le, Q., **Orasanu, E.**, Cardoso, J.M., Melbourne, A., Marlow, N., Ourselin, S., T2 relaxometry in the extremely-preterm brain at adolescence. MRI, 2016

7.1 Methods

7.1.1 Image Processing

To study cortical folding, we looked at the white-grey matter boundary. Specifically, we used the white matter segmentations obtained from GIF [29] to obtain smooth triangle-based meshes to study its outer boundary. The thalamus and cerebellum segmentation labels obtained from GIF [29] were used to obtain smooth triangle-based meshes of the thalamus and cerebellum respectively.

The volumes of the white matter, thalamus and cerebellum were obtained from mesh volume and their surface areas were calculated as the sum of all triangles.

7.1.2 Groupwise Analysis using Spectral Matching

As stated before, the groupwise analysis was performed on 60 extremely preterm for young adults (38 F + 22 M) and 48 matched controls (29 F + 19 F). For each cohort (preterm and control) we chose a random subject as a template to map all other surfaces using joint spectral matching with a CPD initialisation [115], as described in the previous section. This was done for the white matter, thalamus and cerebellum meshes, within each of the two groups. We obtain a mean shape of the thalamus, cerebellum and white matter for each of the two cohorts by averaging the 3D coordinates of the corresponding surface points across the group and structure. We note that the particular choice of template does not affect the result [138].

We then performed another step of CPD and joint spectral matching to find a correspondence between the preterm and control mean surfaces. Morphological changes between the groups were then investigated by computing the difference in vertex position (displacement maps) of the corresponding surface points across the mean thalamic shapes or WM/GM surfaces.

This pipeline was repeated to investigate gender differences within each cohort, since it is known that preterm males are prone to experience neurological and developmental disabilities compared to preterm females [65]. Groupwise shape analysis using spectral matching has previously been shown to give reliable results [138].

Three preterm subjects were excluded from the cerebellum analysis because they exhibited abnormally small cerebellar size (about half the mean size of the other preterm subjects).

7.1.3 Statistical Analysis

Statistical analysis was performed using the Matlab Toolbox SurfStat [166]. We used the Hotelling T^2 two sample metric to derive a local group difference metric and local p-values for all corresponding points [144]. The Hotelling T^2 two sample metric has the advantage of being invariant to the choice of the template used in each cohort. We fitted a multivariate general linear model to our data and corrected for thalamic/white matter volume and gender to asses the group differences. We then computed the vertex-wise T-statistics using a random field theory multiple-comparison correction to yield an equivalent p-value of 0.05 [144]. Finally, we generated a map of local group difference between the controls and extremely-preterm cohorts.

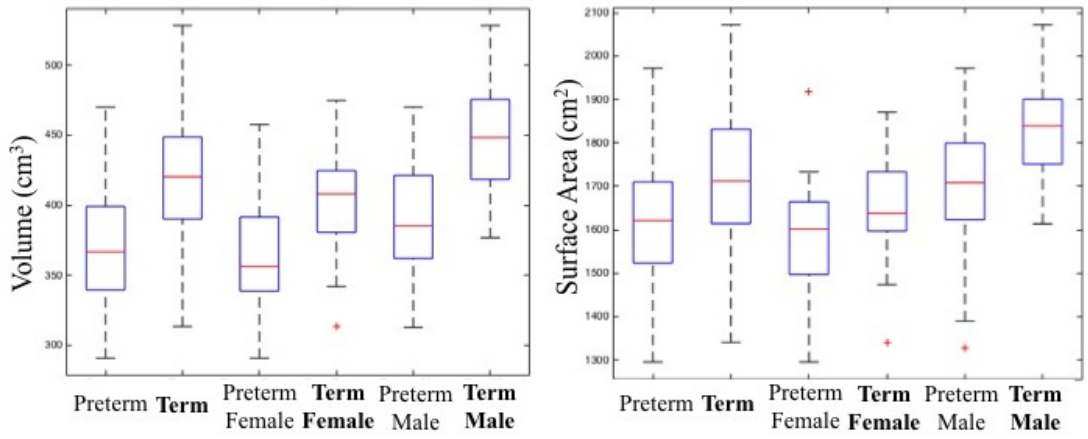

Figure 7.1: Volume and surface area of the white matter in the EPICure cohort

7.2 Results

7.2.1 Volume and surface area

The volume and surface area distributions for the white matter, thalamus and cerebellum are shown in Figures 7.1, 7.2 and 7.3.

7.2.1.1 White matter volume and surface area

The average white matter volume is smaller in preterm subjects ($371.62 \pm 44.12cm^3$) than in control subjects ($419.55 \pm 44.92cm^3$), $p = 2 \cdot 10^{-7}$, with larger variability in the preterm population. When we separate subjects by gender within each group (preterm and control), we notice that the average white matter volume is smaller in females than males in both groups ($360.83 \pm 40.38cm^3$ and $390.25 \pm 44.86cm^3$ in the preterm population for female and male, respectively and $400.15 \pm 38.02cm^3$ and $449.15 \pm 38.58cm^3$ for the control population for female and male, respectively). There is a significant difference between control and preterm cohorts in the average white matter volume for both female ($p = 0.00014$) and male ($p = 0.00007$).

The average white matter surface area is also larger in the control cohort than in preterm cohort ($1724.0 \pm 147.8cm^2$ vs. $1619.4 \pm 151.8cm^2$, $p = 1.3 \cdot 10^{-6}$) and when separating by gender: female preterm vs. control surface area are $1571.7 \pm 129.8cm^2$ vs. $1652.7 \pm 120.4cm^2$, $p = 0.0112$; male preterm vs. control surface area $1701.7 \pm 154.6cm^2$ vs. $1832.8 \pm 117.6cm^2$, $p = 0.0045$.

Melbourne et al. (2016) found similar results when investigating the white matter volumes in a subset of this cohort, but the volumes were computed from the tissue segmentations [97].

7.2.1.2 Thalamic volume and surface area

Consistent with previous findings, we firstly notice that the average thalamic volume is larger in control subjects ($12.94 \pm 1.18cm^3$) than in the preterm population ($11.15 \pm 1.23cm^3$), $p = 9.5 \cdot 10^{-12}$. When separating the subjects by gender, we notice that the average thalamic volume is smaller in females than

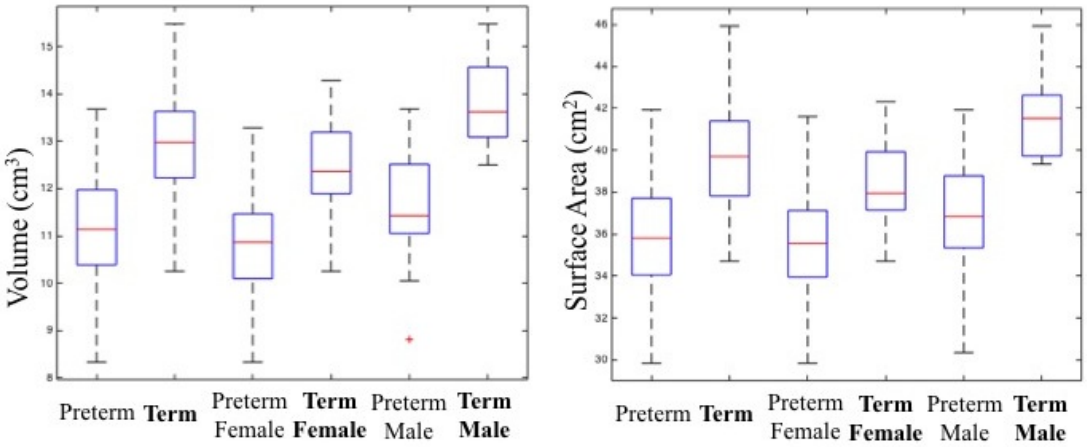

Figure 7.2: Volume and surface area of the thalamus in the EPICure cohort

males: $10.87 \pm 1.17 cm^3$ and $11.63 \pm 1.19 cm^3$ in the preterm population for female and male, respectively and $12.41 \pm 1.04 cm^3$ and $13.74 \pm 0.92 cm^3$ for the control population for female and male, respectively. There is significant difference between control and preterm cohorts in the average thalamic volume for both female ($p = 4.5 \cdot 10^{-7}$) and male ($p = 2.3 \cdot 10^{-7}$).

Similarly the average thalamic surface area is larger in control subjects than in preterm subjects ($39.61 \pm 2.48 cm^2$ vs. $35.93 \pm 2.72 cm^2$), $p = 7.3 \cdot 10^{-11}$, and regardless of gender: in female control vs. preterm surface area are $38.35 \pm 1.99 cm^2$ vs. $35.34 \pm 2.60 cm^2$ ($p = 2.5 \cdot 10^{-6}$), while in male control vs. preterm surface area $41.52 \pm 1.87 cm^2$ vs. $36.95 \pm 2.68 cm^2$ ($p = 2.4 \cdot 10^{-7}$).

7.2.1.3 Cerebellar volume and surface area

Similar patterns are observed for the cerebellum as well, with smaller cerebellum volume in preterm subjects ($115.63 \pm 15.47 cm^3$) than in control subjects ($129.01 \pm 11.92 cm^3$), $p = 3.6 \cdot 10^{-6}$. When we separate the groups by gender, average cerebellar volume is larger in the control control for both females and males: in female preterm vs. control cerebellar volume are $112.99 \pm 13.62 cm^3$ vs. $122.21 \pm 9.74 cm^3$ and in the male preterm and control cerebellar volume are $120.90 \pm 17.86 cm^3$ and $139.39 \pm 5.92 cm^3$, respectively. There is significant difference between control and preterm cohorts in the cerebellar volume for both female ($p = 0.0029$) and male ($p = 0.0002$), with larger differences in males than in females.

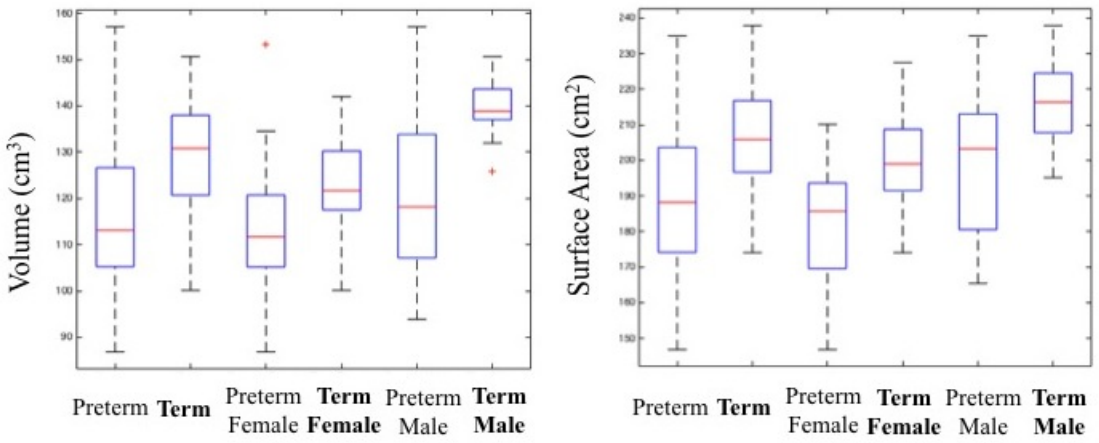

Figure 7.3: Volume and surface area of the cerebellum in the EPICure cohort

The surface area of the cerebellum is also smaller in the preterm population than in the control population for all subjects ($188.37 \pm 19.74 cm^2$ vs. $206.05 \pm 14.53 cm^2$, $p = 0.0005$), and when separating by gender: female preterm vs. control surface area are $183.15 \pm 17.17 cm^2$ vs. $199.87 \pm 12.92 cm^2$, $p = 4.4 \cdot 10^{-5}$; male preterm vs. control surface area $198.80 \pm 20.84 cm^2$ vs. $215.48 \pm 11.66 cm^2$, $p = 0.0043$.

7.2.2 Cortical folding patterns

The vertex displacement map shows that local shape differences in cortical folding between control and preterm groups fall mainly in the temporal lobe and frontal-parietal region, while there are only small variations in the prefrontal and occipital regions (Figure 7.4) [114]. There is no noticeable assymmetry.

The local shape differences between the preterm and term males are large, with more differences in the left hemisphere than in the right (Figure 7.5). Local shape differences between the preterm and term females are smaller, with no noticeable asymmetry (Figure 7.6). The differences are greater in the left hemisphere than in the right.

After correcting for volume and gender, the folding group shape significance maps show that the differences in the temporal lobe are statistically significant at a p=0.05 significance level between the preterm and control groups. The left-right asymmetry is not significant.

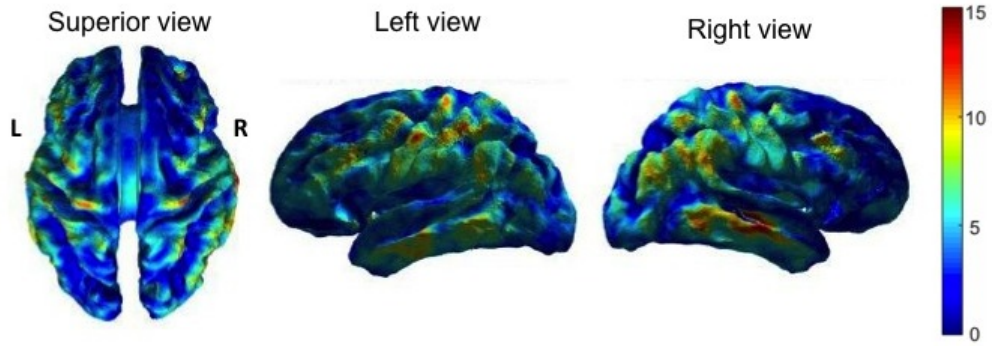

Figure 7.4: Local shape differences between the preterm and term mean white-grey matter boundary: superior aspect and lateral aspect (left and right). Units of scale are mm.

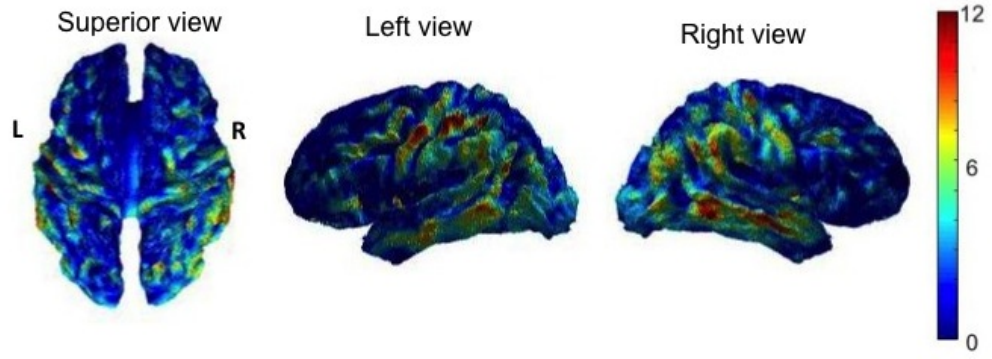

Figure 7.5: Local shape differences between the female preterm and female term mean white-grey matter boundary: superior aspect and lateral aspect (left and right). Units of scale are mm.

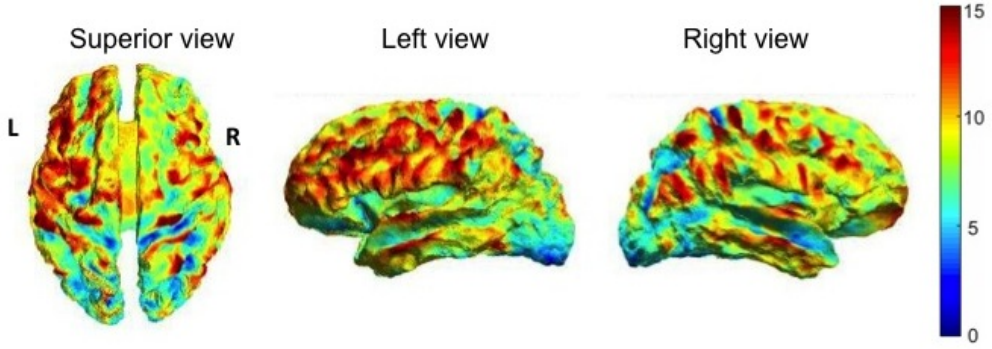

Figure 7.6: Local shape differences between the male preterm and male term mean white-grey matter boundary: superior aspect and lateral aspect (left and right). Units of scale are mm.

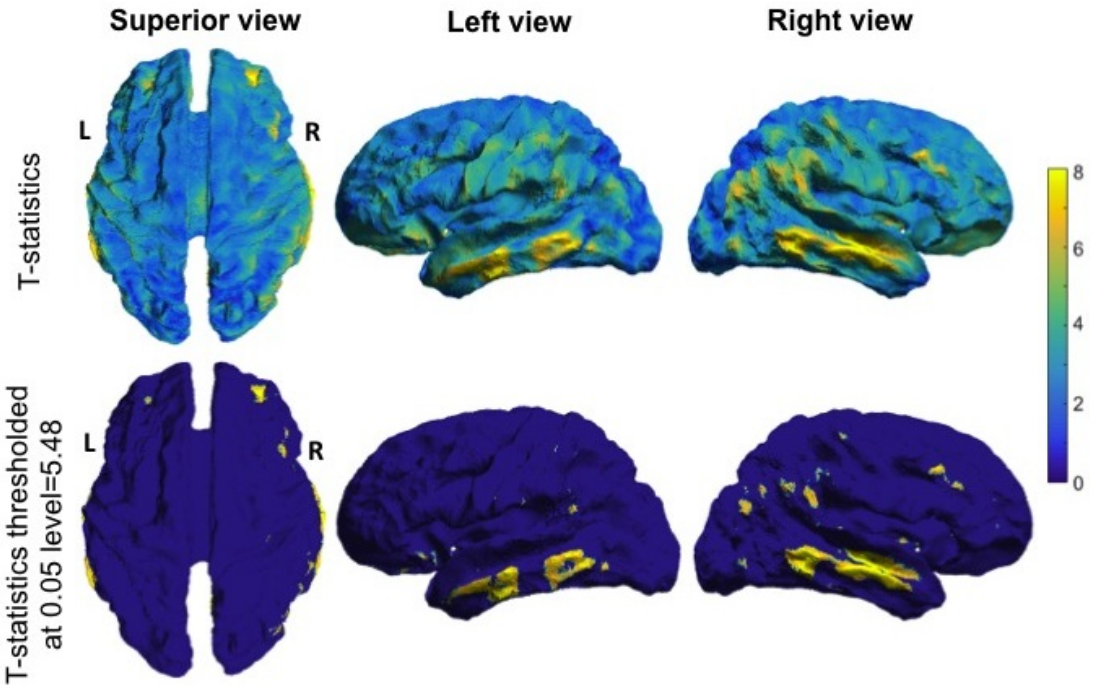

Figure 7.7: Significance maps of white-grey matter group difference controlling for white matter volume and gender. P-value of 0.05 corresponds to a T-stat of 5.48, hence regions with T-stat values greater than 5.48 will pass the random field theory based multiple comparison thresholding at 0.05 significance level.

7.2.3 Thalamus shape analysis

The local shape differences between control and preterm groups are larger in the anterior part of the thalamus than in the posterior part (Figure 7.8) [113]. These differences are larger in the left hemisphere than in the right.

Local shape differences between the preterm and term females are quite constant with no noticeable asymmetry (Figure 7.10). The local shape differences between the preterm and term males are large, especially in the anterior part of the thalamus (Figure 7.9). The differences are greater in the left hemisphere than in the right.

The group shape significance map, corrected for thalamic volume and gender (Figure 7.11), shows that the shape of the superior-lateral and inferior-lateral parts of the thalamus is significantly different between the preterm and control groups, with a slight non-significant left-right asymmetry.

7.2.4 Cerebellum Shape Analysis

The local shape differences between control and preterm groups are constant (Figure 7.12). These differences are slightly larger in the left hemisphere than in the right.

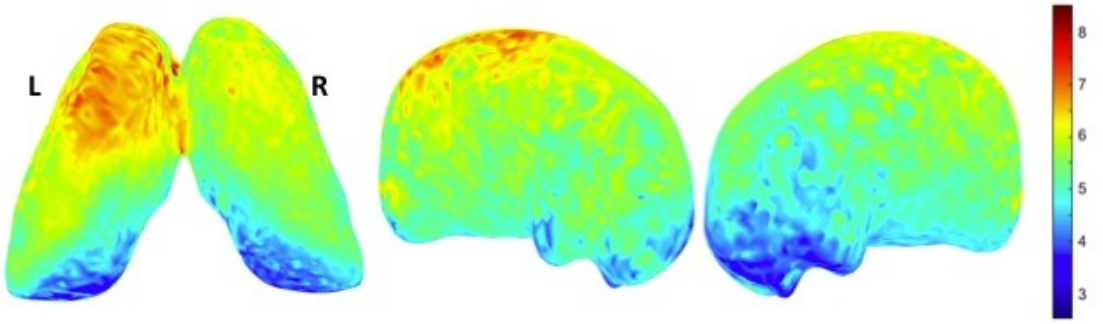

Figure 7.8: Local shape differences between the preterm and term mean thalamus: superior aspect and lateral aspect (left and right). Units of scale are mm.

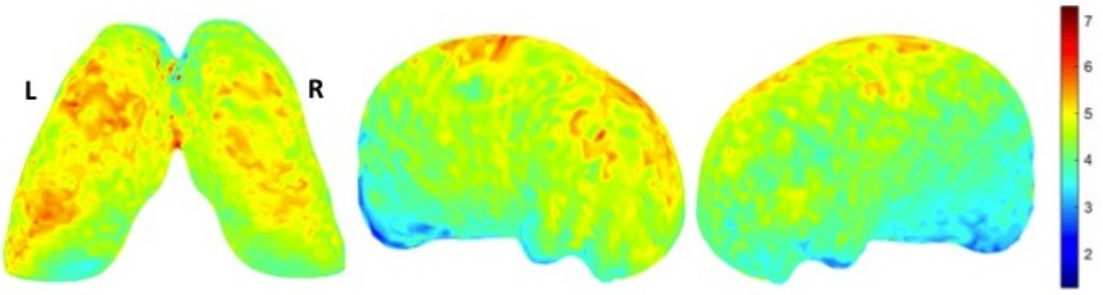

Figure 7.9: Local shape differences between the female preterm and female term mean thalamus: superior aspect and lateral aspect (left and right). Units of scale are mm.

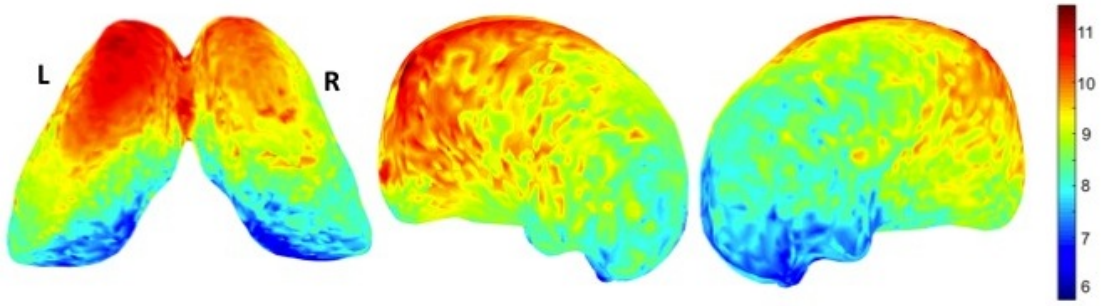

Figure 7.10: Local shape differences between the male preterm and male term mean thalamus: superior aspect and lateral aspect (left and right). Units of scale are mm.

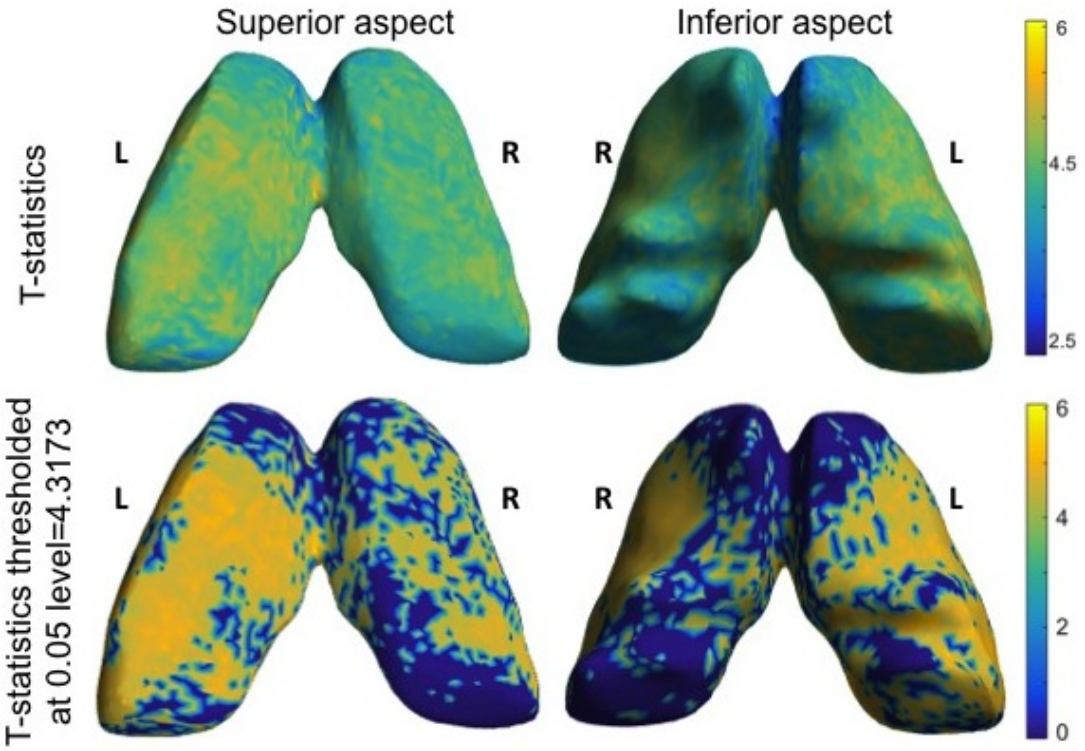

Figure 7.11: Significance maps of thalamus group difference controlling for thalamic volume and gender. P-value of 0.05 corresponds to a T-stat of 4.3173, hence regions with T-stat values greater than 4.3173 will pass the random field theory based multiple comparison thresholding at 0.05 significance level.

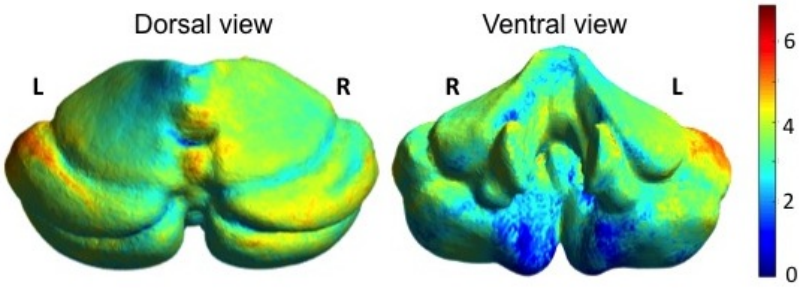

Figure 7.12: Local shape differences between the preterm and term mean cerebellum: dorsal and ventral view. Units of scale are mm.

We notice that there are larger shape differences in the male population between the control and preterm individuals, while the differences in females are smaller. The upper part of the cerebellum exhibits less difference between the preterm and control cohorts than the lower part in the female subjects, while the opposite is observed in male subjects. Furthermore, there is again a slight left-right asymmetry.

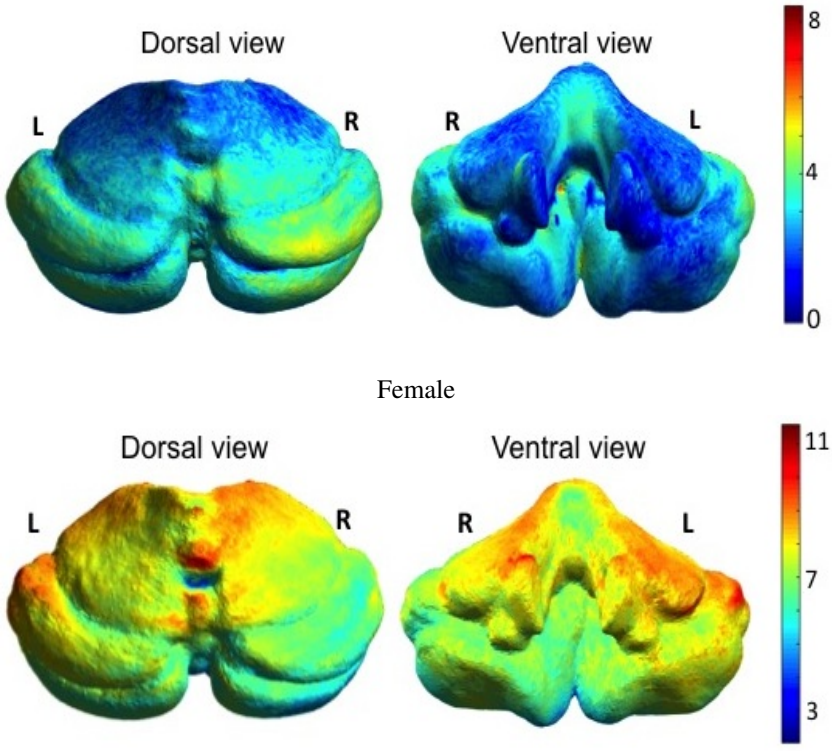

Figure 7.13: Local shape differences between the preterm and term mean cerebellum by gender: dorsal and ventral view. Units of scale are mm.

After correcting for volume and gender, the cerebellum shape significance maps show no statistically significant differences at a p=0.05 significance level between the preterm and control groups.

7.3 Discussion

In this study we investigated the differences in cerebral folding, thalamic and cerebellar shape between 60 extremely preterm and 48 term born adolescents by looking at the distance between corresponding vertices after matching the white-grey matter surfaces, thalamic and cerebellar surfaces, using joint spectral matching.

The thalamus was smaller in preterm-born individuals ($p = 9.5e^{-12}$) with differences mainly in the anterior thalamus and these differences were more pronounced in male subjects. The anterior thalamus connects to brain regions with roles in executive function, working memory, problem solving, mood and motivation [67]. Thalamic shape differences were more pronounced in the superior part, which has substantial connections to the temporal lobe [168], that has a role in language and verbal memory. Similar anterior and superior thalamic differences have been found in studies on ADHD subjects[7], and it may be interesting to explore the links further between thalamic shape, composition and the influence on an extreme prematurity-ADHD correlation [119]. Our future work will explore this possibility by making use of a neurocognitive assessment battery.

Vertex displacement differences are larger in the temporal and frontal-parietal regions. However, after correcting for gender and white matter volume, which is smaller in preterm born individuals ($p = 2e^{-7}$), only the differences in the temporal lobe remain statistically significant. This result is consistent with previous studies that found reduction in white and grey matter volumes of the temporal lobes in other preterm cohorts [51], [54], associated with neurological deficits, poor executive function and language deficits.

The cerebellum did not exhibit any significant shape differences between control and preterm young adults, although smaller volumes were still noticed in the preterm population.

The gender analysis showed that the differences between extremely preterms and controls in white matter, thalamic and cerebellar volumes are larger in males than in females. In the control population, the males usually have larger volumes of brain structures than females, however the opposite is true for the extremely preterm population. When looking at shape differences between the two groups by gender, again we notice how the differences are larger in males than in females for the white matter, thalamus and cerebellum. This is evidence that the brain development of males is more affected than that of females, if born extremely preterm. This is consistent with previous findings in preterm infants [89], children [74] and young adults [43], that found the male population to be more affected by prematurity in terms of brain development and/or neurological outcome.

Our future work will analyse the possible functional implications of the shape differences with cognitive and language performance, as well as investigating the inter-relationship between cortical white matter volume and shape and the specific physical links of the temporal lobe with regions to which it is connected including the basal ganglia. This can be done through tractography, by using the white matter tracts visible in diffusion data to parcellate the thalamus by its connections to the cortex [143].

Chapter 8

Tensor Spectral Matching

In this chapter we introduce spectral matching in the context of non-linear registration of diffusion tensor images. In the following Section 8.1 we described the proposed TSM-DTI-TK framework. We first extend the definition of the graph Laplacian of an image to DTIs, to provide a novel representation of the global geometrical properties of diffusion tensors via their spectral components. We then introduce Tensor Spectral Matching (TSM) registration of DTI images, to define spatial correspondences through the matching of the spectral components associated to the graph Laplacian. Finally, we combine TSM and one of the state-of-art algorithms for tensor registration, to provide a novel optimal registration framework (TSM-DTI-TK) accounting for both global and local tensor's properties. The experimental results show that TSM-DTI-TK outperforms standard registration approaches when applied to both adult data (Section 8.2) and preterm infant data (Section 8.3). In Section 8.4, we look at results obtained when applying this framework to the infant data. The proposed pipeline thus represents a promising tool to investigate brain development during the crucial preterm period, how it is affected by preterm birth and how it might influence neurological outcome. Additionally this type of research might start to illuminate the debate on the mechanical role of tissue growth on the observed cortical folding pattern, information that is only measurable in foetal and neonatal cohorts of this type.

Derived publications:

- **Orasanu, E.**, Melbourne, A., Lorenzi, M., Lombaert, H., Modat, M., Eaton-Rosen, Z., Kendall, G.S., Robertson, N.J., Marlow, N., Ourselin, S., Tensor Spectral Matching of Diffusion Weighted Images: Application on Extremely Preterm-Born Neonates. *Submitted*, 2016
- **Orasanu, E.**, Melbourne, A., Modat, M., Lorenzi, M., Lombaert, H., Eaton-Rosen, Z., Robertson, N.J., Kendall, G.S., Marlow, N., Ourselin, S., Mapping longitudinal white matter changes in extremely preterm born infants. ISMRM, 2016
- **Orasanu, E.**, Melbourne, A., Lorenzi, M., Modat, M., Lombaert, H., Eaton-Rosen, Z., Kendall, G.S., Robertson, N.J., Marlow, N., Ourselin, S., Tensor Spectral Matching of Diffusion Weighted Images. SAMI Workshop (MICCAI), 2015

8.1 Tensor Spectral Matching

The tensor spectral matching algorithm is based on two main processing steps: 1) computation of the tensor spectral components associated with diffusion weighted images, and 2) subsequent estimation of their spatial correspondences. These steps are detailed in the following sections.

8.1.1 Computation of Tensor Spectral Components

Let $\mathbf{R}$ be a diffusion tensor image associating at each voxel x a tensor defined as a semi-positive definite symmetric (SPD) 3-by-3 matrix: $\mathbf{R}(x) \in SPD(3)$. The estimation of the tensor spectral components requires the construction of the general Laplacian matrix $\mathcal{L}$ associated to the diffusion weighted image $\mathbf{R}$. In this case, the nodes of the graph are the image voxels, while the weights of edges are described by the local similarity with respect to the neighbouring locations (six immediate neighbouring voxels).

In the case of a DT image, we have to take into account that voxel locations are associated to tensors. For each pair of neighbouring voxels x_i and x_j, $x_i \neq x_j$, we estimate the entry W_{ij} of the adjacency matrix depending on both the Euclidean distance between the nodes (voxels) and on the similarity of the associated tensor information $\mathbf{R}(x_i)$ and $\mathbf{R}(x_j)$. This is quantified by the log-Euclidean distance of SPD matrices: $dist(\mathbf{R}(x_i), \mathbf{R}(x_j))_T = \|log(\mathbf{R}(x_i)) - log(\mathbf{R}(x_j))\|$, where $\|\cdot\|$ is the L_2 norm [7]. The proposed similarity measure is therefore computed as:

$$W_{ij} = \exp\left(\frac{-dist(\mathbf{R}(x_i), \mathbf{R}(x_j))_T^2}{\sigma^2}\right) / (\|x_i - x_j\|^2), \tag{8.1.1}$$

where σ is a measure of the tensor's variation across the image, and is here computed as the average tensor distance in the graph: $\sigma = mean_{i,j}(dist(\mathbf{R}(x_i), \mathbf{R}(x_j)))$.

8.1.2 Tensor Spectral Matching (TSM): Spatial Correspondence estimation of DTI through spectral matching

Given the reference and floating diffusion tensor images $\mathbf{R}$ and $\mathbf{F}$, let $\mathbf{U^R}$ and $\mathbf{U^F}$ be the correspondent tensor spectral components obtained with the decomposition detailed in the first part of this section. The spectral matching algorithm estimates the spatial correspondences between $\mathbf{R}$ and $\mathbf{F}$ by optimising the correspondences between the spectral coordinates defined by the first k components of $\mathbf{U^R}$ and $\mathbf{U^F}$, corrected for their sign ambiguity and multiplicity [87].

As inspired by [87], which used additional features like sulcal depth for the spectral matching of surfaces, we added extra features to be optimised on top of the first spectral modes, represented by the fractional anisotropy maps for the reference and floating DTI, $FA^{\mathbf{R}}$ and $FA^{\mathbf{F}}$, and the coordinate grid to enforce spatial coherence and geometry. Then, by using the corrected components and the extra features of each image, we create the *spectral representations* $\tilde{\mathbf{R}} = \left(U_1^{\mathbf{R}}, U_2^{\mathbf{R}}, \ldots, U_k^{\mathbf{R}}, FA^{\mathbf{R}}\right)$ and $\tilde{\mathbf{F}} = \left(U_1^{\mathbf{F}}, U_2^{\mathbf{F}}, \ldots, U_k^{\mathbf{F}}, FA^{\mathbf{F}}\right)$ of respectively reference and floating images.

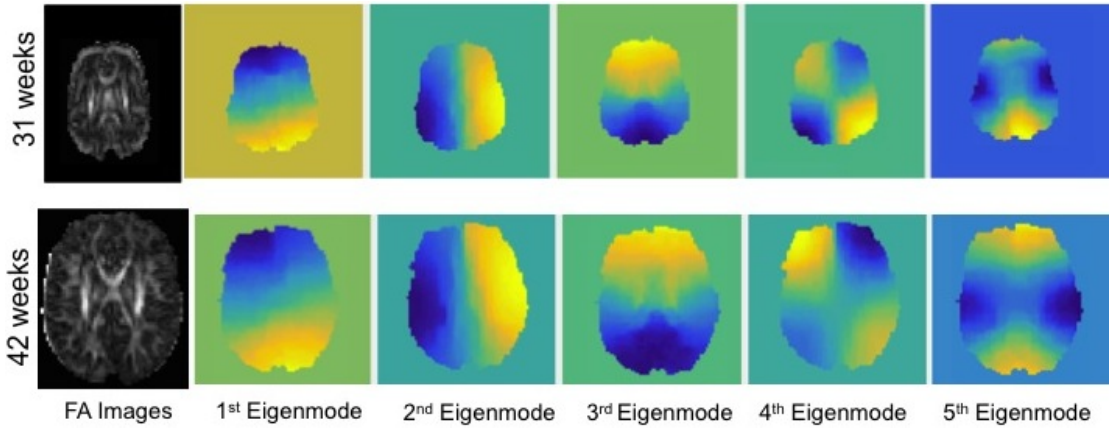

Figure 8.1: Fractional anisotropy maps and first 5 spectral modes of infant *c* at two different time points.

In the case of longitudinal preterm born-data, when large deformations are taking place, the first tensor spectral components describe similar patterns (Figure8.1).

We estimate the spatial transformation $\phi(x)$ by optimising the similarity between the spectral representations $\tilde{\mathbf{R}}$ and $\tilde{\mathbf{F}}$, through a nearest-neighbours search, by including a local regularisation term based on the minimisation of the harmonic energy associated to the transformation [85].

In what follows, the optimal parameter for the trade-off between similarities of the spectral representations and transformation regularity has been estimated by cross-validation: all experiments were repeated for several regularisation parameters and we selected the minimal one which guaranteed positive Jacobian determinant values for all the pair-wise registrations performed.

8.1.3 Combining global spectral features with local tensor information: TSM-DTI-TK

TSM optimises the correspondences based on global spectral information only. Therefore it does not account for local tensor properties, such as the local tensor orientation. On the contrary, standard tensor registration methods, such as DTI-TK[1] [175], optimise the local tensor similarity while explicitly account for tensor alignment or the preservation of the principal direction [2]. However, they might be suboptimal in modelling large displacement due to the local nature of the similarity measure.

We propose here a novel registration framework, TSM-DTI-TK, to account for both *global* spectral features and *local* tensor information. The proposed approach is based on defining the initial global tensor correspondences via TSM registration. The result of this initial alignment is then used to initialise DTI-TK[2] in order to optimise the tensor matching with respect to the local tensor properties. The proposed framework pipeline is described in Figure 8.2.

[1] http://www.nitrc.org/projects/dtitk

[2] http://dti-tk.sourceforge.net/pmwiki/pmwiki.php

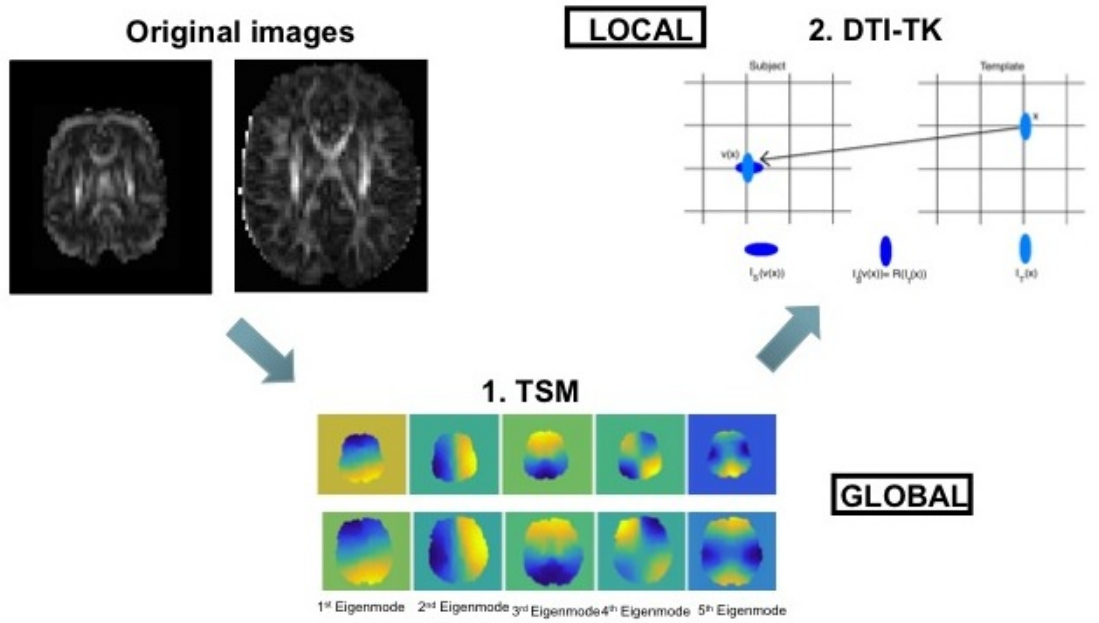

Figure 8.2: Proposed diffusion tensor registration framework (TSM-DTI-TK) with two steps: 1. TSM registration ensuring global alignment when large deformations are present; 2. DTI-TK tensor angle reorientation refinement ensuring local correspondences.

8.2 Experiment 1: Average Group Template of Adult Data

In this first experiment, we compare the tensor spectral matching (TSM) and TSM-DTI-TK to the DTI-TK tensor non-linear registration method [175], which is among the state-of-art registration methods for diffusion tensors [163]. The registration parameters used for DTI-TK were the default ones proposed by the developers [175]. The registration quality was measured by quantitative and qualitative assessment of the similarity between the FA maps computed from the resampled and template tensor images. Furthermore, we look at overall differences between the alignment of the principal directions of the tensors of the resampled diffusion tensor images and of the template.

8.2.1 Methods

The comparison of the three methods (TSM, DTI-TK and TSM-DTI-TK) was based on the group-wise registration of the diffusion weighted images from the 20 term control young adults, part of the EPICure study, described in Section 3.3, to a common anatomical template. The reference atlas chosen for this experiment is the freely-available one provided in the DTI-TK toolbox. All the 20 subjects' diffusion images were initially linearly registered to the atlas using a pairwise affine accounting for tensor orientation [175]. The linearly aligned images were subsequently non-linearly registered to the atlas with TSM, DTI-TK and TSM-DTI-TK, and resampled in the atlas space with respect to the tensor orientation using Finite Strain [2]. Fractional anisotropy maps of the resulting diffusion tensor images were finally estimated from the resulting resampled tensors using NiftyFit [98].

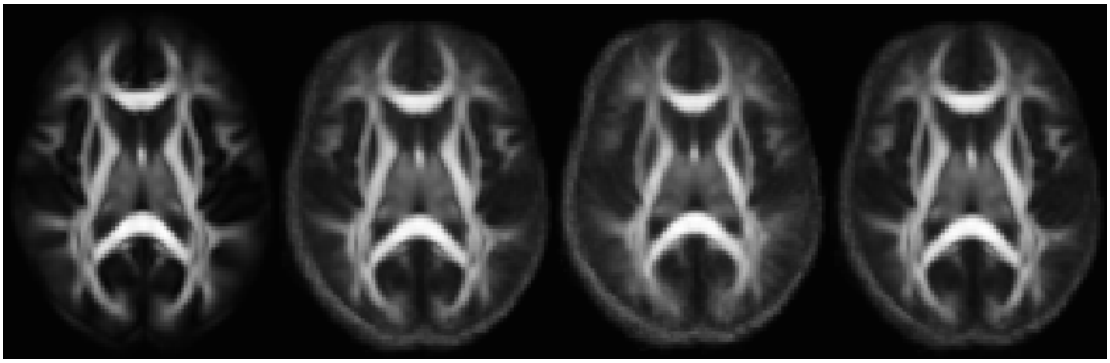

(a) Template FA

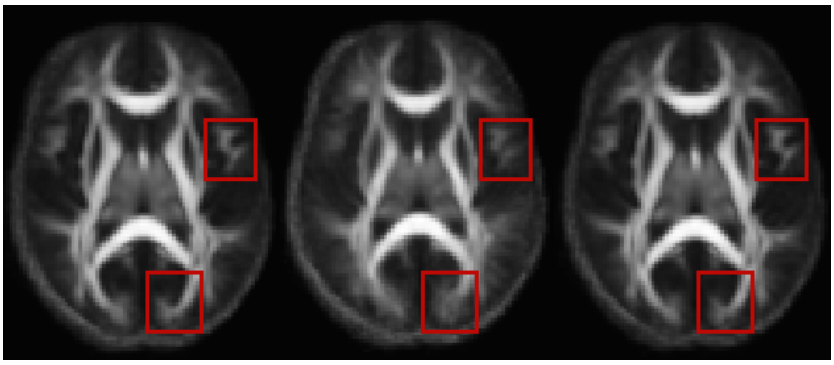

(b) Average FA TSM

(c) Average FA DTI-TK

(d) Average FA TSM-DTI-TK

Figure 8.3: Visual comparison of average registration results of TSM (b), DTI-TK (c) and TSM-DTI-TK (d) when registering adult data to template (a). When using TSM, global features look sharper, such as the forceps major and regions in the frontal lateral lobe

8.2.2 Results

Figure 8.3 shows the average estimated FA maps obtained after tensor registration using TSM, DTI-TK and TSM-DTI-TK. We note that the images look very similar after all three methods, indicating that the alignment performed by the different algorithms leads to visually similar anisotropy properties of the resulting resampled diffusion tensors. Furthermore, we notice that TSM and TSM-DTI-TK present sharper features than DTI-TK in some areas, such as the forceps major and the frontal-lateral lobe.

Figure 8.4 shows the mean absolute difference in FA and angle between the principal directions of the template and resampled tensors for all three methods in the entire brain. Looking at the differences in FA and performing a pairwise t-test between each two methods, we notice that the differences for TSM-DTI-TK are comparable with TSM ($p > 0.05$) and smaller and statistically significant different than DTI-TK ($p = 0.037$). When comparing the angle between the tensors from the original template and the resampled ones after registration, we notice how TSM is not as accurate on the local scale and is statistically significantly different than DTI-TK ($p = 2.5 \cdot 10{-}11$) and TSM-DTI-TK ($p = 1.4 \cdot 10^{-18}$), while TSM-DTI-TK provides marginally better results than DTI-TK alone but not statistically significant different ($p > 0.05$).

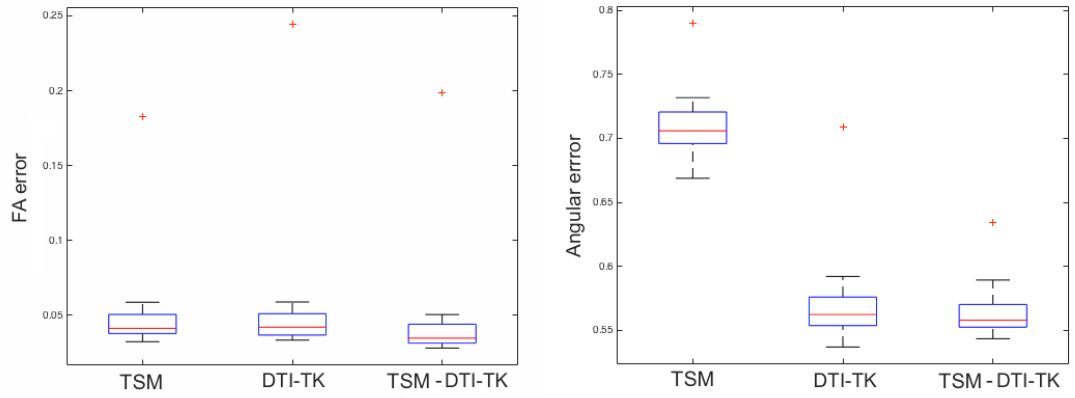

(a) Mean difference in FA

(b) Mean difference in angle [rad]

Figure 8.4: Boxplots of mean absolute differences in FA and angle between the principal directions of the original template tensors and resampled tensors on the adult data.

It can be observed that although TSM provides an accurate global registration, it underperforms DTI-TK when it comes to tensor alignment and reorientation. However, TSM-DTI-TK outperforms both methods, likely due to the optimisation of the log-Euclidean similarity measure between tensors as it is more sensitive to FA than to the principal directions. In addition to this initial anisotropy optimisation, DTI-TK explicitly optimises the rotation as a refinement step, providing a better result.

8.3 Experiment 2: Validation on Longitudinal Infant Data

In this experiment we evaluate the performance of TSM-DTI-TK with respect to other diffusion tensor registration techniques (DTI-TK, TSM, affine tensor registration) on longitudinal preterm infant data.

8.3.1 Methods

For the longitudinal infant data, described in Section 3.2, the comparison of the three methods (TSM, DTI-TK and TSM-DTI-TK) was based on the longitudinal registration of diffusion weighted images from of the two time points for all 9 infants. We aligned and scaled our images using a rigid followed by an affine transformation [175]. We then used TSM and DTI-TK to register the term scan to the preterm space for each individual infant, as well as the proposed framework TSM-DTI-TK.

8.3.2 Results

Figure 8.5 (a) and (b) show an example of the FA maps of a sample infant (subject *c* from Table 3.1) scanned preterm and at term equivalent age and its registration, from term to preterm, by using the TSM-DTI-TK (c). The WM shows aligned tracts, including for the frontal region. This is an important results since the frontal region of the brain is usually prone to susceptibility artefacts in diffusion MRI and large

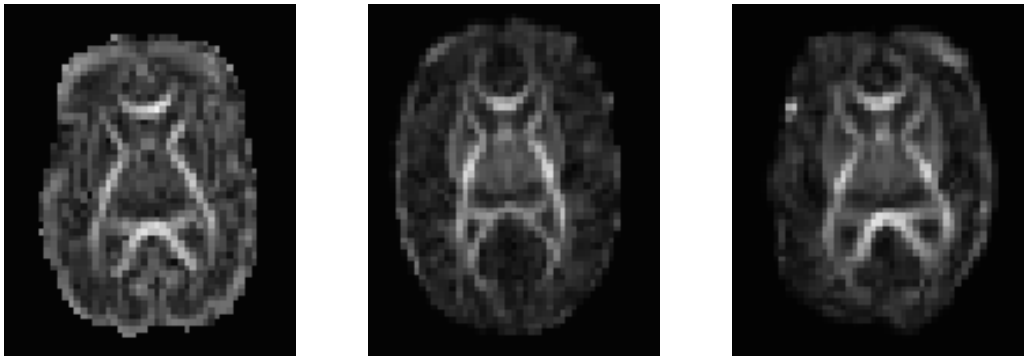

(a) Preterm Reference (b) Term Floating (Affine) (c) TSM-DTI-TK (ours)

Figure 8.5: Visual comparison of the FA maps of infant c at first time point, second time point (after affine registration) and after registration using the TSM-DTI-TK framework

FA grey matter changes, making it harder to register across subjects.

As shown by Figure 8.6: DTI-TK does not improve drastically the affine alignment; TSM improves the alignment and the FA difference is decreased, although the orientation is not improved; TSM-DTI-TK improves the tensor orientation significantly. After a t-test between each of the three registration methods and the affine only registration, the differences in FA of the WM are not statistically significant, but there is significant improvement in tensor orientation for TSM-DTI-TK when compared with any of the other methods ($p < 0.05$). While DTI-TK cannot cope with the large deformations that are taking place, TSM is able to capture this development. TSM-DTI-TK improves matching of shape, anisotropy and tensor orientation.

8.4 Experiment 3: Application of TSM-DTI-TK to Longitudinal Extremely Preterm-Born Infant Data

In this experiment we show that the TSM-DTI-TK can be successfully applied for the analysis of developmental changes in the white matter of preterm infants. We longitudinally register the diffusion tensor images of nine preterm infants. We perform a groupwise registration to obtain an average image at the early time point. We then quantify the obtained results by looking at the longitudinal changes of the deformation field brought into the same common space.

8.4.1 Methods

Using TSM-DTI-TK, we registered diffusion weighted images from the longitudinal time points for all 9 infants as described in Section 3.2. To investigate the longitudinal microstructural changes during the preterm period in each subject i, we looked at changes in the deformation field of the TSM-DTI-TK transformation, ϕ_i.

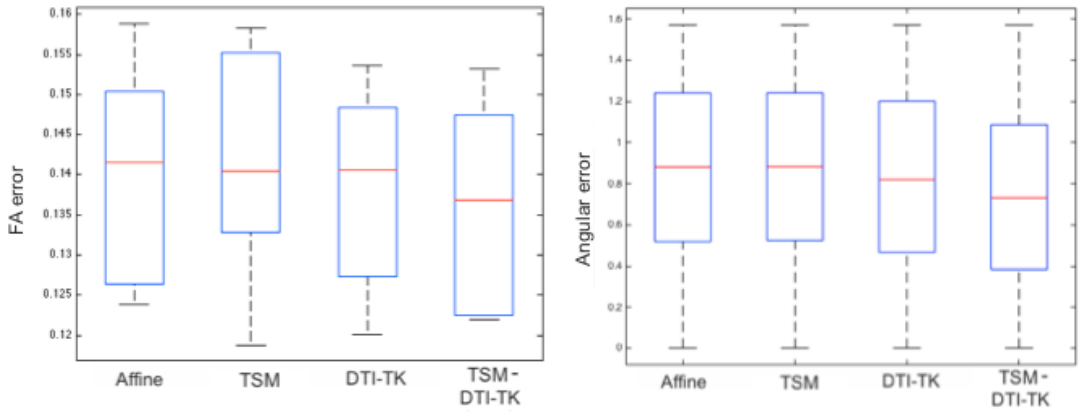

(a) Mean Difference in FA

(b) Mean Difference in Angle [rad]

Figure 8.6: Boxplots of mean absolute differences in FA in white matter and angle orientation in the white matter for the preterm infant data (all subjects)

We performed a groupwise registration between the diffusion tensor images at the first timepoint from all infants to create an average early scan atlas space. First, we chose a random subject as initial template and we linearly registered the early DTIs of all other infants to the one of the chosen template. We then averaged the resulting images to create a first average atlas image. We then registered all early DTIs to the average atlas linearly, followed by the same TSM-DTI-TK framework, to create an average atlas. The average atlas was updated after each non-linear registration step. The number of registration steps in a groupwise usually depends on the diversity of the images. Four non-linear registrations (TSM-DTI-TK) were required until convergence of the procedure. The final transformations γ_i which maps each early time points of each subject i to the obtained average space is thus a composition of one affine transformation ad four TSM-DTI-TK transformations.

Finally, for each subject i we mapped the longitudinal change (deformation field) obtained from the ϕ_i transformation into the average early time point space by applying the transformation γ_i to investigate microstructural changes during the preterm period for all infants in a same common space. This registration pipeline is described in Figure 8.7.

8.4.2 Results

The longitudinal changes in deformation field magnitude follow similar patterns, with larger deformations in the corpus callosum and internal capsule in all infants (Figure 8.8). The changes in the white matter regions appear to be proportional to the time difference between scans. Considering a constant change over time in the white matter structures, we estimated an average rate of change per week from the magnitude of the deformation field. This was computed by averaging the changes in all infants and correcting for scan time [117]. From the map of average rate change in white matter structures (Figure 8.8, last row), we notice again that the internal capsule and corpus callosum are subject to the largest

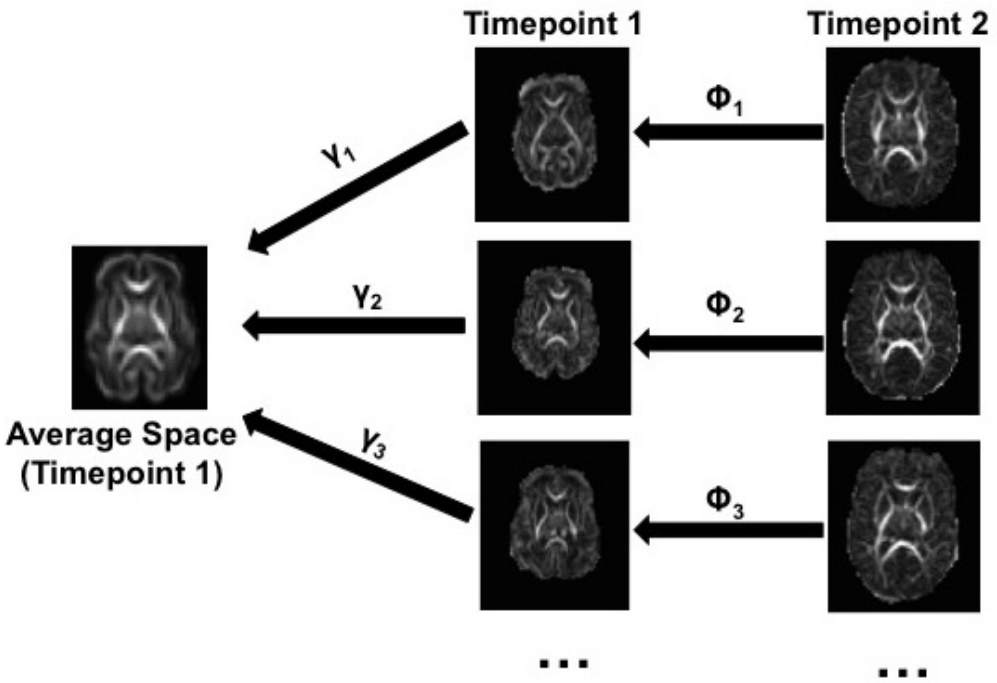

Figure 8.7: Groupwise registration of the extremely preterm infant data. Longitudinal inter-subject registration is performed using TSM-DTI-TK. Cross-sectional registration is performed for the first timepoint to create an average space where we mapped all the longitudinal changes. This average space is obtained after performing one affine transformation and four TSM-DTI-TK steps.

changes during the preterm period.

8.5 Discussion

In this work we proposed a novel registration framework for diffusion weighted images (TSM-DTI-TK) based on the spectral decomposition of the diffusion tensor images and one of the state-of-the-art algorithms for tensor registration. When applied alone, TSM was found to be comparable globally to DTI-TK on adult data, however it underperforms compared to DTI-TK when it comes to tensor alignment and reorientation, which is expected since DTI-TK minimises the angle between tensors as part of its optimisation process.

Tensor orientation in the spectral matching framework is conceptually difficult but could be added using an iterative strategy. Thus, combining TSM with DTI-TK (TSM-DTI-TK) provides a novel optimal registration framework accounting for both global and local tensor properties, improving the DTI-TK result. Moreover, TSM-DTI-TK outperformed DTI-TK alone when applied to longitudinal diffusion data from preterm-born infants ($p < 0.05$). The favourable preliminary results on the preterm cohort were enabled by the proposed $global$ representation of tensor features obtained through the spectral decomposition strategy introduced in this paper.

We successfully registered longitudinal diffusion tensor images of nine extremely preterm born infants

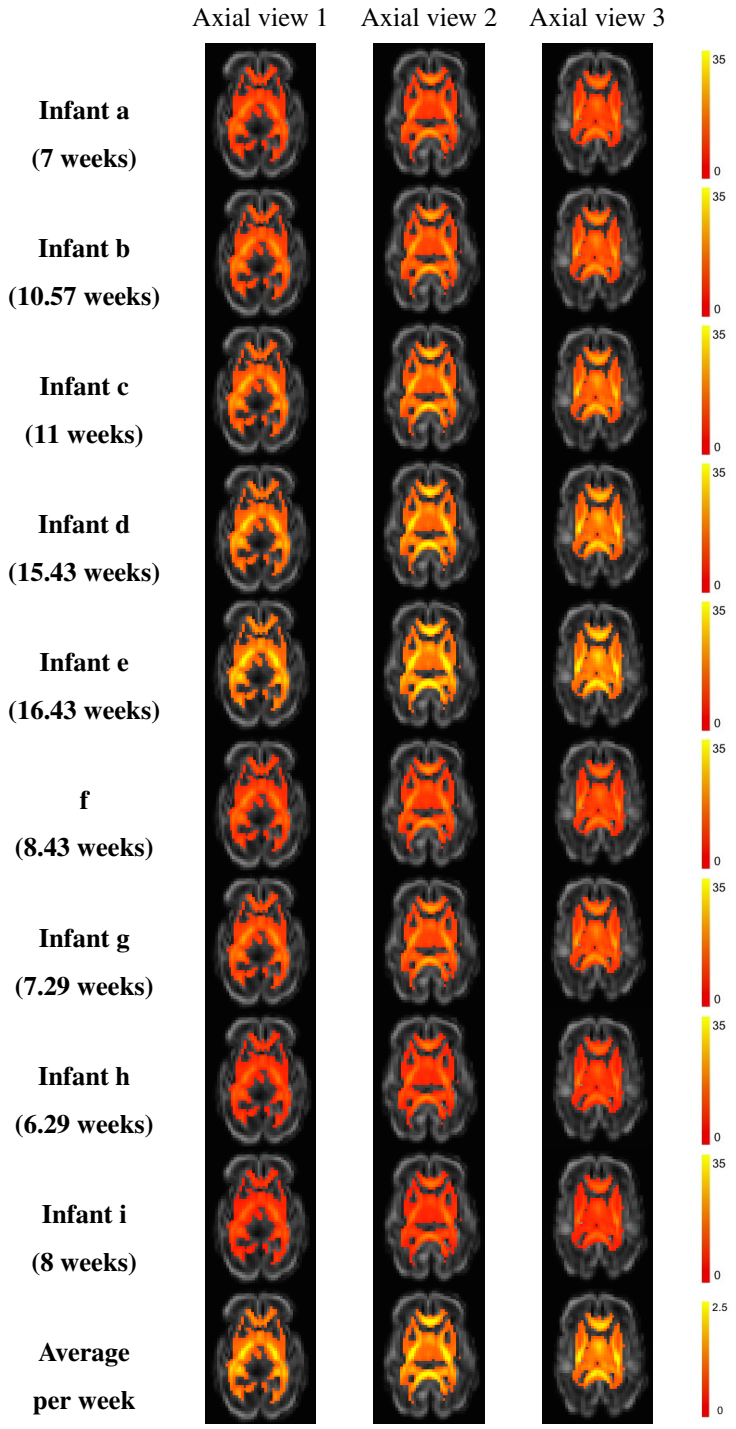

Figure 8.8: Longitudinal changes during the preterm period in white matter diffusion tensor images at three different axial views from the scalar deformation field. Units are mm. Changes are larger when the time between scans is larger (infants ***d***, ***e***) compared to shorter time period between scans (infant ***h***). Last row shows the average rates of longitudinal changes per week during the preterm period in white matter diffusion tensor images at three different axial views in all infants. The largest white matter changes appear to be in the corpus callosum and internal capsule.

scanned shortly after birth and at term time. Using the same framework, we also created an average early time point scan to map all the changes in the same space. We notice that morphometric microstructural changes are consistent among infants and that the largest changes during the preterm period take place in the corpus callosum (CC) and internal capsule. Hence, these regions are likely to be affected by preterm birth and influence neurodevelopment in extremely preterm born infants. The corpus callosum is the largest white matter tract, with a role in interhemispheric communication. Previous studies found smaller CC in preterm infants, when compared to their term peers, with the posterior CC being more vulnerable to insults [152]. Deficits in the CC have been previously associated with delayed motor functioning and reduced IQ and disorders such as autism, attention deficits, schizophrenia and bipolar disorder [152]. The internal capsule carries the major sensory and motor pathways from the cortex to the spinal cord and back [41]. Abnormalities in the internal capsule have been associated with many metabolic diseases and it is a strong predictor of abnormal motor outcome in hypoxic-ischaemic encephalopathy [41]. Disruptions in the development of the CC and internal capsule may affect other regions connected to them, hence it is important to know how they develop over the preterm period to predict further outcome.

A limitation of TSM is that it does not optimise for tensor reorientation, hence the need to add the DTI-TK registration step. A future goal would be to incorporate this reorientation into the spectral matching pipeline. This could be achieved as an additional optimisation step after an initial spectral matching using an iterative process of tensor embedding matching and tensor reorientation at each step. One way of implementing the reorientation as part of the spectral embedding would be to add the principal directions or angles as an additional registration step, with more weighing. Another limitation of this work is the relatively small number of extremely preterm born infants. Recruitment of these infants is quite a challenging task, particularly when attempting to obtain longitudinal data, since most of them spend a long time in the intensive care unit.

Our further work will include quantification of the white matter changes and acquisition of more subjects to perform a statistical analysis. The proposed registration technique of diffusion tensor images allows one to quantify the changes in diffusion parameters over the preterm period on a voxel-wise basis in different white matter tracts. Investigating longitudinal microstructural changes in tracts was out of the scope of this paper and it requires an accurate segmentation of the white matter tracts, which is very challenging for this cohort, especially for the early timepoint. Methods to tackle tract segmentation in similar populations have been proposed [13] and we aim to test their applicability on our datasets. Future recruiting of more subjects will allow us to do a voxel-wise statistical analysis of longitudinal changes in the microstructure and clarify our understanding of this early developmental stage. Furthermore, we plan to investigate correlations between the microstructural white matter development and morphological changes occurring in the cortex over the same timeframe, which may elucidate relationships between the cortical surface folding and in establishing cortico-cortical connections.

The proposed registration framework represents a very promising tool for the study of large morphological changes in the white matter of preterm and extremely preterm-born infants, a problem which, to the

best of our knowledge, has not been addressed before. Medical image computing techniques of this type are fundamental to establish, *in vivo*, what leads to the developmental differences seen between preterm children and their term-born peers.

Chapter 9

Multi Modal Spectral Matching

As already stated, longitudinal studies over the preterm period are challenging for several reasons. First, the early and more developed infant brains have very different appearance and connectivity. Spectral techniques have been used in the preterm populations for matching white matter surfaces for the study of longitudinal cortical folding patterns and changes in the white-grey matter boundary [109] (see Chapter 6). These techniques have proved successful in the intra-subject case due to the prominance of primary sulci even at early gestational age allowing matching to be driven by low-frequency spatial features. Second, the anatomical variability of cortical surfaces is very high cross-sectionally, and variability is not well-represented by geometric folding patterns. This is especially true in the very early stages of development, when we deal with lissencephalic brains from different subjects. During the very-preterm period, additional diffusion information of the white matter might guide surface registration by contributing emergent microstructural information; high cortical fractional anisotropy (FA) is a feature of early brain development, although FA falls rapidly in the third trimester with cortical maturation. Matching of diffusion tensor images alone [116] (see Chapter 8) to study longitudinal changes in diffusion parameters and white matter tract shape has already shown to be successful, but is of limited use to align cortical surfaces except within a very narrow age range.

In this chapter we propose a novel multi-modal registration technique based on Pairing Images using Multi-Modal Spectra (PIMMS) to register cross-sectional data from 9 early-scanned preterm infants (Chapter 3, Section 3.2) and investigate longitudinal rates of change in cortical thickness, cortical FA and MD, in the created groupwise space. The method matches the combined spectra based on tensor similarity inside the white matter (from the diffusion weighted images), described in Chapter 8, and the WM/GM surface information (obtained from structural image segmentation). The proposed method has an advantage over the classical surface registration algorithm (spectral matching of surfaces - JSM), since it optimises surface and microstructural information, thus providing a more biologically meaningful mapping based on additional tissue properties and not only sulcal patterns. This is particularly of interest in the case of cross-sectional early data, where the lissencephalic brain is more challenging to register using regular surface registration techniques, since there is less surface information to drive the registration. The mapping also enables us to study multi-modal variations and interdependency between

parameters obtained from different imaging modalities.

This work was conducted in collaboration with the Neurophysics department at the Max Planck Institute for Cognitive and Brain Sciences in Leipzig, Germany.

Derived publications:

- **Orasanu, E.**, Bazin, P.L., Melbourne, A., Lorenzi, M., Lombaert, H., Kendall, G.S., Robertson, N.J., Weiskopf, N., Marlow, N., Ourselin, S., Longitudinal analysis of the preterm cortex using multi-modal spectral matching. MICCAI, 2016.

9.1 Pairing Images using Multi-Modal Spectra (PIMMS)

To estimate a more biologically meaningful surface matching in the case of lissencephalic surfaces, we propose the novel PIMMS, which uses both diffusion tensor images and surface information [108]. Combining surface (2D) and volume (3D) information is not trivial [126]. Here, we tackled this problem by embedding the surface with a level set representation in the 3D image domain, and reformulating the surface spectral matching problem in this context. We followed the previous strategies of spectral decomposition in the case of surfaces and diffusion tensor images. We then compared the groupwise average of PIMMS with the results of JSM.

9.1.1 Level Set representation of surface boundary

Surface information can be represented in Cartesian grid by using a level-set framework. The level set representation of a surface boundary is a signed function, where the value at each voxel is equal to the distance of the voxel from the boundary, with positive values outside the surface and negative values inside [120]. An advantage of level sets is that numerical computations of surface curvature and normals can easily be evaluated in the Cartesian space without surface parametrisation [88]. Changes in topology like breaking and merging are well-defined and can be allowed or prevented [63].

9.1.2 Spectral components of surface in image domain

To decompose the cortical surface, but in image space, we used the level set images of the white-grey matter boundary, I_{LS}. For computation efficiency of our decomposition, we considered a subset of our image, $I_{LS\Omega_1}$, consisting of the voxels around the boundary within a chosen threshold. Similarly to the surface decomposition, where we need to have continuous surfaces with no holes to obtain smooth spectra, we chose the smallest threshold (for computational efficiency) that ensured a continuous surface for all subjects, which was found to be of 3.5 mm in the presented work.

We constructed the connected graph (V, E) with the vertices V being image voxels and the edges E are defined by the neighbourhood structure of these vertices. We then represented the graph with its adjacency matrix W, where for each pair of voxels i and j, $i \neq j$, with the level set values x_i and x_j respectively, W_{ij} is 1 if the voxels are neighbours and 0 if they are not. The diagonal matrix D gives the

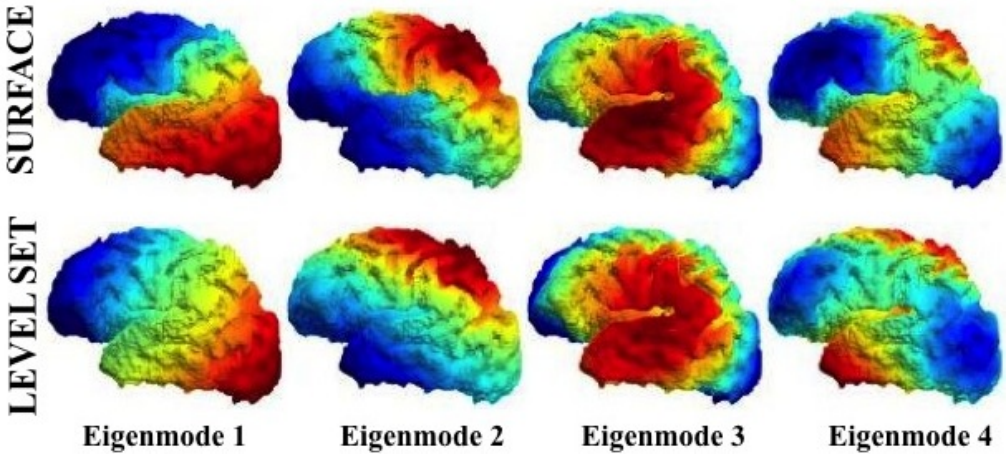

Figure 9.2: Spectral modes of shape variation given by the decomposition of a subset of the level set image of the white-grey matter boundary mapped on the corresponding surface, and the modes given by the direct surface decomposition of the same boundary in the same subject

total weighting of all edges connected to each voxel and is computed by $D_{ii} = \sum_j W_{ij}$. The general graph Laplacian is defined by $\mathcal{L} = G^{-1}(D - W)$, with G being the diagonal node weighting matrix, which we computed according to the each voxel i's inverse level set value $G_{ii} = 1/x_i$. Hence, elements closer to the boundary, with a smaller level set value, will have a higher weighting when computing the spectra.

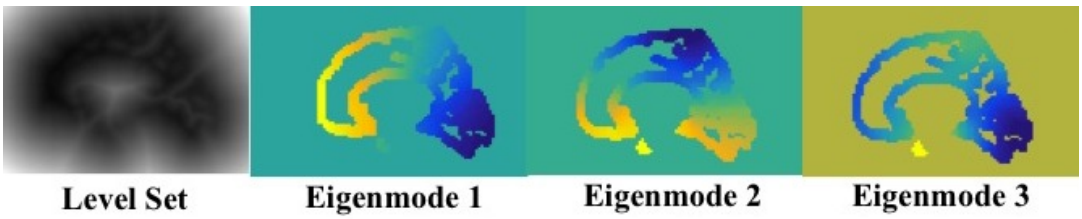

Figure 9.1: Level set representation of the white-grey matter boundary and the first 3 spectral modes of shape variation given by its decomposition

The graph spectrum of the level set image at the defined points is given by the eigen-decomposition of the general graph Laplacian $\mathcal{L}$ .The spectral components $U_{1LS\Omega_1}, \ldots, U_{NLS\Omega_1}$ represent the fundamental modes of vibrations of the image, and respectively describe increasing complexity of its geometric features, from coarse to fine scales. An example level set image and its decomposition around the white-grey matter boundary is shown in Figure 9.1.

Mapping the obtained spectra from the level set image decomposition on surfaces describe similar patterns of variations as the direct spectral decomposition of surfaces given by [87], as shown in Figure 9.2. Scaling variations do exist, probably due to the fact that when we decompose the subset of the level set image, we use more information in deriving the spectra and not only the exact boundary as in the surface case.

9.1.3 Combined Level Set and Diffusion Tensor Spectra

We combined the level set spectra with the spectra obtained by the decomposition of the diffusion tensor images as described by [116]. Our main goal was to optimise the surface correspondence by taking into account microstrucural information of the white matter. Hence, we separately compute tensor spectral components as described in Chapter 8 $U_{1DTI\Omega_2}, \ldots, U_{NDTI\Omega_2}$ for a subset of the image $I_{DTI\Omega_2}$, in the deeper white matter structures, i.e. for the values inside the level set boundary (negative level set values) and outside the level set subset $I_{LS\Omega_1}$ ($I_{DTI\Omega_2} \bigcup I_{LS\Omega_1} = \emptyset$). The independently computed spectra were then combined together to obtain the combined spectra, with voxels receiving spectral information from either diffusion (inside the WM) or the surface data (around the boundary) $[U_{1LS\Omega_1}, U_{1DTI\Omega_2}], \ldots, [U_{NLS\Omega_1}, U_{NDTI\Omega_2}]$ (Figure 9.3).

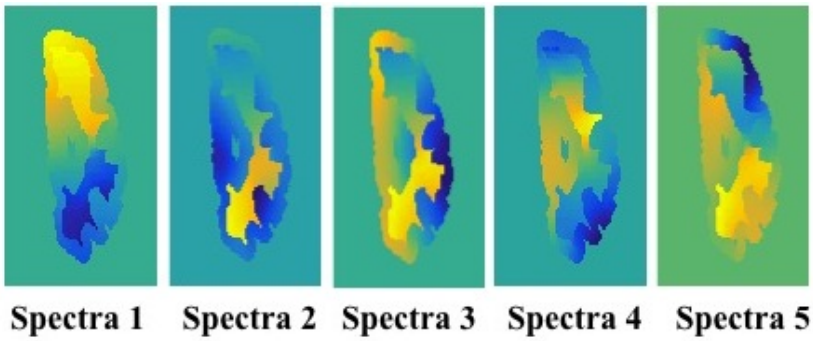

Figure 9.3: Combined spectral modes for the left hemisphere: shape variation given by the decomposition a subset of a level set image (edges of the surface) and microstructural variation given by the decomposition of the diffusion tensor image (inner)

9.1.4 Matching of multi-modal spectra

Having the multi-modal spectra of two subjects R and F, we can now estimate the spatial correspondences between them by optimising the correspondences between the spectral coordinates defined by the first k multi-modal components of $\mathbf{U^R}$, and $\mathbf{U^F}$. We followed the computational scheme introduced in [87]. Briefly, the first k spectral components are initially corrected for their sign ambiguity by computing the dot product between the corresponding eigenmodes at similar locations. For this we ran a coherent-point drift (CPD) rigid registration [104] of the respective clouds of points, which we used just to ensure the sign matching of the spectra in both the spectral and diffusion components, independently.

Using the combined spectral representation and the thresholded level set distance maps for regularisation of the reference and floating images, we estimate a spatial transformation $\phi(x)$. This is done by optimising the similarity between the embeddings (spectral representations and level set distance maps) through a nearest-neighbour search, by including a local regularisation term based on minimising the harmonic energy associated to the transformation [85]. Note that this was done by matching the spectra separately, and not by building a joint graph.

9.2 Validation

In this section we validate PIMMS by comparing it with results of the Joint-Spectral Matching (JSM) of surfaces (mono-modal) and Multi-contrast Multi-scale Surface Registration (multi-modal). The accuracy of the matching was evaluated by comparing at each vertex the standard deviation of the mean diffusivity values in the groupwise space. A lower variability indicates better alignment and consistency of the registration algorithm. We chose the MD for this validation over the FA, since FA values in the cortex are more homogeneous.

9.2.1 Comparison of PIMMS with Joint-Spectral Surface Matching

We used both PIMMS and JSM (see Chapter 6) to create a groupwise average of the early time point of the subjects described in Section 3.2.

Figure 9.4 first and second rows show that the registration error, quantified by the standard deviation of the mean diffusivity, is minimised when we used the proposed multi-modal technique. The smaller variation in mean diffusivity when using PIMMS is more obvious on the inside surface of the white matter meshes (second and fourth columns), as well as in the prefrontal cortex. Using additional microstructural information improves the alignment of the surfaces by taking into account tissue properties, while JSM is inherently limited to the use of geometric similarity only.

9.2.2 Comparison of PIMMS with Multi-contrast Multi-scale Surface Registration (MMSR)

Subsequently, we used MMSR (implemented as part of the CBS toolbox[1] in mipav, using the JIST processing infrastructure[2]) to create a groupwise average of the early time point of the subjects described in Section 3.2. MMSR is a multi-modal registration technique based on registering partially inflated surfaces in the level-set framework, to which it different contrast types can be added [88]. MMSR was shown to give comparable results to Freesurfer, when no contrast is used, and these results are improved when contrast is added [88]. T1 maps were previously used as contrast by MMSR, since they reflect myelin content and thus improve the cortical alignment [88]. However, in the case of infants born extremely preterm, myelination is still on-going and since the infants are not scanned at the same time, they will be at various stages of myelination. We decided to use FA maps as contrast for MMSR, since this is also used as an embedding for TSM.

Figure 9.4, first and third rows, show that the variation of the mean MD is minimised when we used the proposed multi-modal technique, PIMMS, instead of MMSR. Smaller variation in mean diffusivity when using PIMMS is observed on the inside surface of the white matter meshes (second and fourth columns), but also across gyri in the occipital and parietal lobes.

[1] http://www.nitrc.org/projects/cbs-tools

[2] https://www.nitrc.org/projects/jist

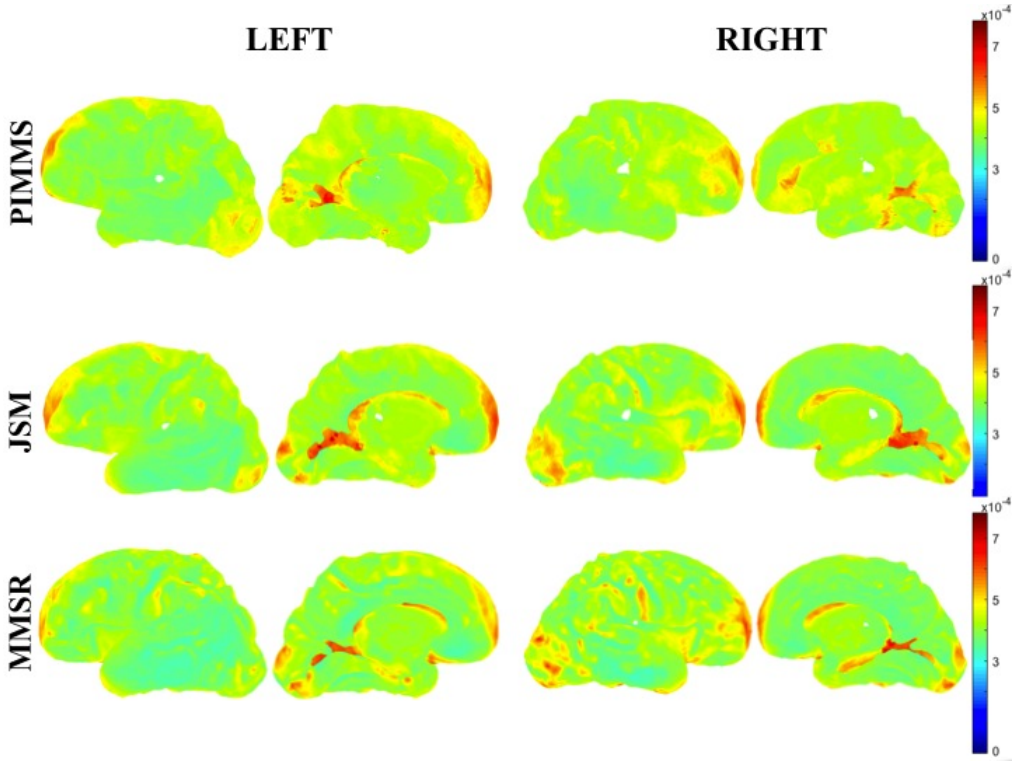

Figure 9.4: Standard deviation in cortical mean diffusivity of the early timepoint on average groupwise for the left hemisphere and right hemisphere (outside and inside views), obtained using the proposed method (PIMMS), Joint-Spectral Matching of surfaces (JSM) and Multi-contrast Multi-scale Surface Registration (MMSR)

9.3 Data processing and experiments

9.3.1 Cortical Thickness

Using the obtained white matter, grey matter and CSF segmentations, we automatically computed the level set functions of the inner (WM/GM), central and outer (GM/CSF) boundaries of each hemisphere of the cerebral cortex using CRUISE [62], implemented as part of the CBS toolbox of mipav. We estimated the cortical thickness (CT) as the difference between the distance to the inner cortical surface and the distance to the outer cortical surfaces (given by the level set values). The WM/GM boundary level set was used to create smooth triangle based meshes of each hemisphere. We mapped the CT values onto the white-grey matter inner surface.

9.3.2 Laminar Analysis

From the level set functions of the WM/GM and GM/CSF boundaries, we created a continuous layering of the cortex (cortical grey matter) [161], also implemented as part of the CBS toolbox of mipav. We used the obtained 11 laminar profiles to sample the FA and MD maps, and computed the mean values of these parameters across the cortex. To reduce partial volume effects, we excluded the first and last three

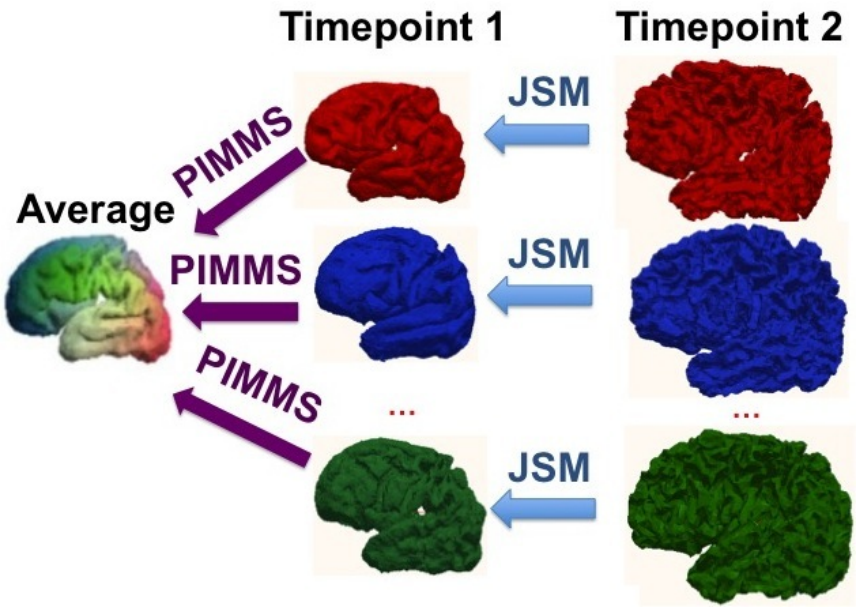

Figure 9.5: Registration pipeline for investigating longitudinal preterm changes in cortical thickness, cortical FA and MD. Intra-subject registration is done using a surface registration only (JSM), while inter-subject registration is done using a multi-modal technique (PIMMS).

profiles from the computation of the average cortical FA and MD values. These mean FA and MD values were then mapped onto the white-grey surface.

9.3.3 Longitudinal and cross-sectional mapping

To quantify the longitudinal changes taking place over the preterm period, we defined a mapping for the intra-subject white matter surfaces, by hemisphere, at the two timepoints, using JSM initialised with a rigid CPD, as explained and detailed in Chapter 6. To investigate the changes in the same reference space, we create an average early time point template, by choosing a random subject as template, mapping all the others into its space and averaging the results using the proposed multi-modal registration method PIMMS described in Section 9.1. The registration pipeline is described in Figure 9.5.

9.4 Results

9.4.1 Cortical Thickness, cortical FA and cortical MD

Figure 9.6 shows an example of infant *c*'s cortical thickness, cortical FA and cortical MD at both time points, mapped onto the respective surface. It can be observed that cortical thickness decreases in the temporal lobe, while increasing in all the other lobes. A decrease in FA is noticed which is expected, except for the region around the central gyrus, where a slight increase in FA is noticed. Furthermore, the changes in MD are small and don't follow a particular pattern.

The visual inspection results are supported when plotting average results (per lobe) for all infants as a function of GA. The cortical thickness increases as a function of GA for all lobes except the temporal

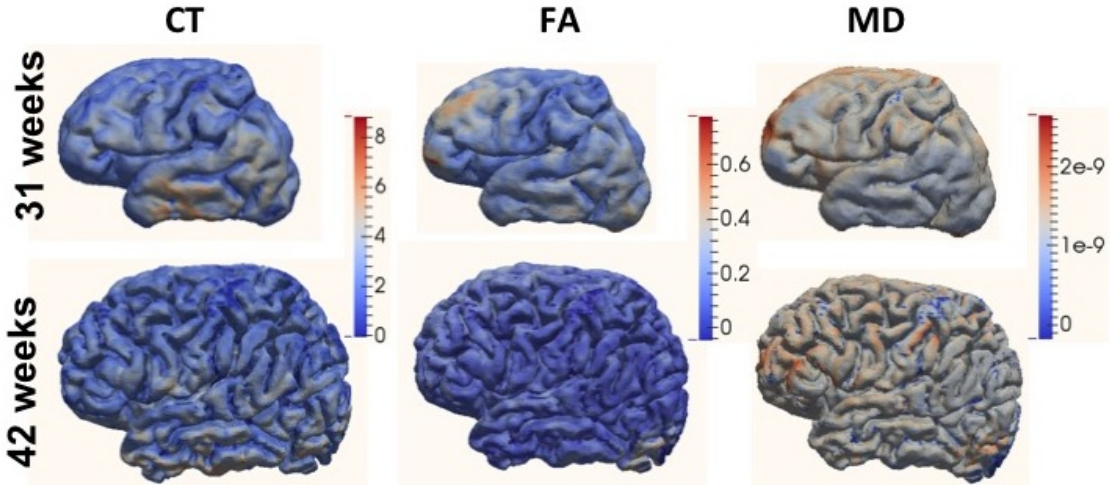

Figure 9.6: Example maps of cortical thickness (CT), cortical fractional anisotropy (FA) and mean diffusivity (MD) plotted on the average surface (mid-cortex) for infant *c*

lobe for which it is decreasing. Cortical FA is decreasing with gestational age, while the changes in cortical MD does not follow any particular pattern.

9.4.2 Groupwise Analysis of Longitudinal Changes

9.4.2.1 Longitudinal Rates of Change

All longitudinal changes in the parameters were corrected for the time between scans. We computed rates of change per week in CT, cortical FA and cortical MD during the preterm period in all infants and mapped them in the groupwise average space (Figure 9.8).

9.4.2.2 Multi-modal parameters interdepencies

To investigate correlations between the rates of change in the cortex, we computed the rank based correlation coefficient between rates in all infants, per region, for each pair of parameters: CT-FA, CT-MD and FA-MD. The p-values were FDR corrected at a 0.05 significance rate. The cortical rates of change show statistically significant correlations between the three measures in different regions summarised in Table 9.1. We notice that the changes in CT and FA are positively correlated, while the ones in CT-MD and FA-MD show a direct negative correlation.

9.5 Discussion

In this work we propose a multi-modal registration technique based on Pairing Images using Multi-Modal Spectra (PIMMS), which defines a surface-to-surface mapping in image domain by optimising both microstructural information in the white matter (from the diffusion tensor images) and WM/GM surface information (obtained from structural image segmentation) [108]. We applied this method to the challenging problem of registering early developmental stages in preterm born infants. Because

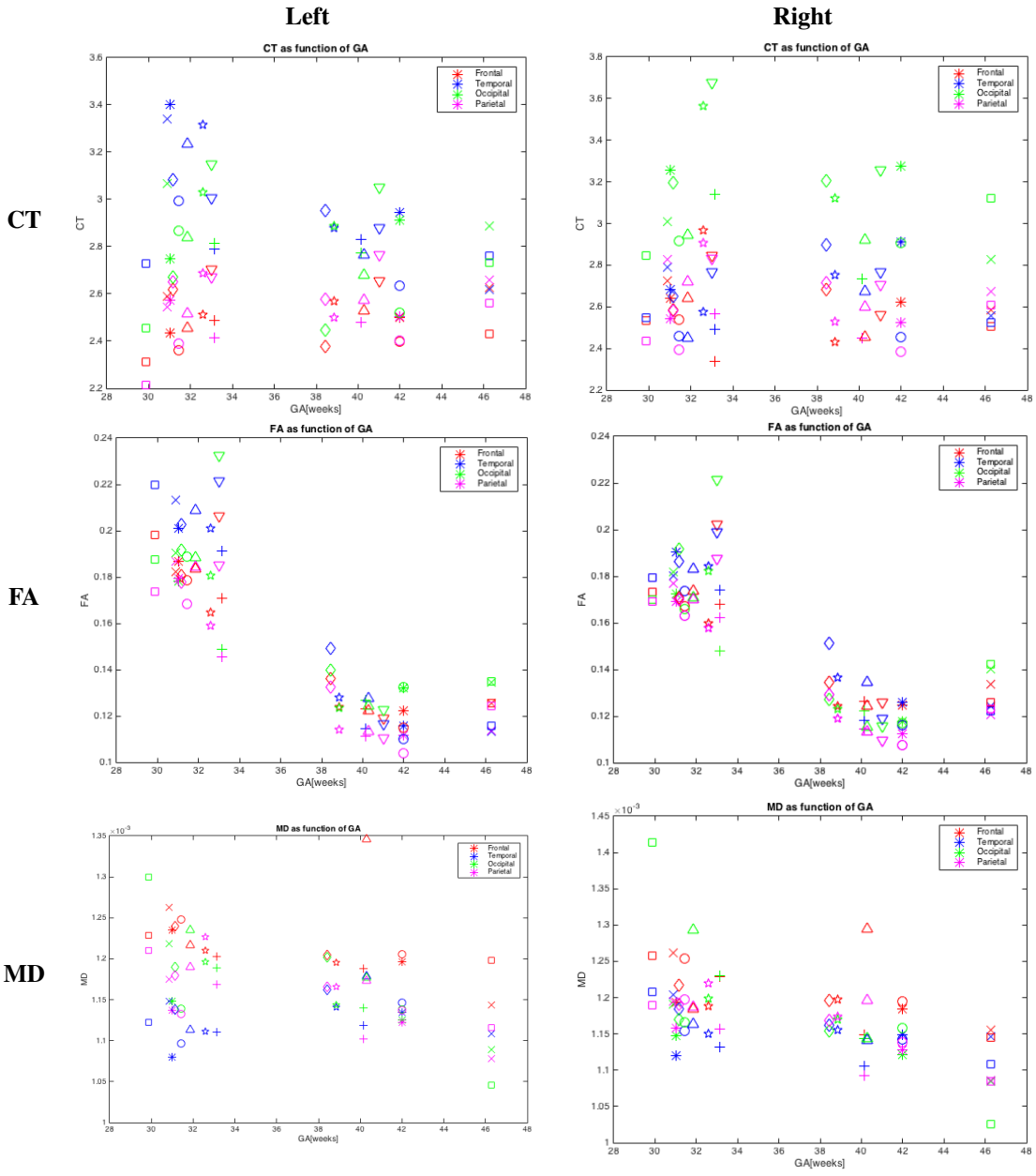

Figure 9.7: Average cortical changes per lobe for all infants as function of gestational age: cortical thickness (upper row), cortical FA (middle row) and cortical MD (lower row). Each infant is represented by a different marker.

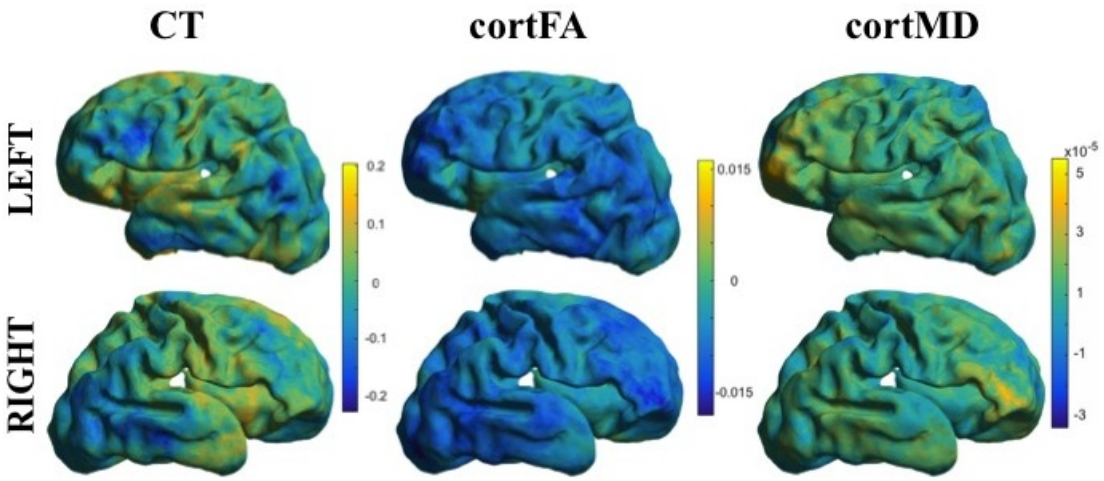

Figure 9.8: Mean Longitudinal Rates of Change per week in cortical thickness (CT), cortical fractional anisotropy (FA) and cortical mean diffusivity (MD) in Groupwise Space

Table 9.1: Statistically significant (0.05 significance, FDR corrected) correlation coefficients between multi-modal cortex parameters in all four lobes. Negative values imply a negative correlation, while positive imply a direct positive correlation. The regions not mentioned did not have a significant correlation between certain parameters.

	Left Hemisphere	Right Hemisphere
CT-FA	Temporal: 0.15, Occipital: 0.09	Temporal: 0.32, Occipital: 0.21
CT-MD	Frontal: -0.06, Occipital: -0.13, Parietal: -0.17	Frontal: -0.11, Temporal: -0.33, Occipital: -0.17
FA-MD	Frontal: -0.24, Temporal: -0.18, Parietal: -0.33	-

of the timing, these surfaces do not provide us with sufficient sulcal patterns needed for a classical surface registration algorithm. The novelty of this method consists in guiding a biologically relevant correspondence for surfaces with low gyrification.

We evaluated PIMMS against JSM (mono-modal registration) and MMSR (multi-modal registration), by looking at the variability of the mean diffusivity in the groupwise space created by each individual method. PIMMS gives a smaller registration error (lower variability in MD) and thus overperforms both these methods.

We used PIMMS to create a groupwise average space of the early developmental time point, in which we mapped longitudinal changes over the preterm period in 9 infants. We investigated the rates of change per week in cortical thickness, cortical fractional anisotropy and cortical mean diffusivity in the cortex. We further investigated the interdependency of these multi-modal parameters of the cortex across the different lobes.

Our future research will imply linking grey and white matter properties close to the surface (e.g. studying cortical laminae in the cortex and closer to the white matter boundary), as well as linking the cortical surface and deep white matter connectivity. Furthermore, this method may allow us to also look into the relationship between cortical folding and fibre-based connectivity.

Chapter 10

Discussion

In this chapter we discuss the results presented in this work and their relevance to the field of neonate imaging, specifically extremely preterm birth. We then present the future directions of this project.

10.1 Summary and impact of results

This thesis presents a variety of mono- and multi-modal registration methods based on spectral matching and processing pipelines for image segmentation for investigating longitudinal changes in structure, shape and microstructure of the brains of extremely preterm born infants over the preterm period.

In Chapter 4 we described the steps required for tissue segmentation in post-mortem fetuses and newborns. We used a previously developed infant specific Expectation-Maximization (EM) segmentation with prior relaxation, AdaPT [28], with anatomical priors. The anatomical priors, however, had to be derived from similar populations, thus we created our own specific atlases for the post-mortem newborn and fetal populations. We demonstrated how the use of an atlas based on subjects with similar characteristics is more appropriate than just using a publicly available neonate atlas, providing better segmentations (see Figure 4.3). Using the obtained accurate segmentations we calculated the brain volumes and weights, respectively; we demonstrated how brain weights obtained from conventional autopsy can be accurately estimated from postmortem MRI. Accurate estimation of brain weight is an integral part of autopsy, since any deviation from normal ranges could indicate pathological change in the brain and therefore might help in establishing the cause of death. This brings further support to the idea of a non-invasive alternative to conventional autopsy, especially in fetuses and newborns: autopsy by MRI, an alternative which would be more acceptable and less traumatising for the parents, without causing delay to the burial or raise religious issues.

We also followed the same pipeline for the tissue segmentation of nine infants born extremely preterm, scanned twice: once shortly after birth around 31 weeks equivalent gestational age (EGA); and once at an average of 41 weeks EGA, as described in Chapter 3.2. Since the data from these infants was challenging to segment due to different low tissue contrast and slight motion of the subjects, the tissue segmentation

also needed appropriate anatomical priors derived from subjects with similar characteristics. We used publicly available atlas to segment three subjects at each different time point, to which we applied slight manual corrections and created a database of accurate segmentations. Each of the other subjects was segmented using anatomical priors derived from the newly created database, and each time fewer manual corrections had to be made. The use of this specific atlas gave a large improvement over the initial segmentation (see Figure 6.1 and the improvement made in Figure 6.2).

In Chapter 5, we introduced the spectral decomposition of a graph and how it can be useful for matching surface boundaries. In Chapter 6 we used spectral representations of the white-grey matter boundaries to define a longitudinal correspondence, after defining an initial correspondence using a rigid CPD instead of FOCUSR, between the preterm and term equivalent surfaces of the nine extremely preterm born infants. CPD was shown to be more stable than FOCUSR for the ordering and sign flipping of the spectra and thus assuring a good match (see Figure 6.4). Defining such a correspondence was a challenge, since the brain undergoes major development over the preterm period, changing in volume, surface area, shape and cortical folding. However, the lower frequency modes of shape variation defined by the spectral decomposition of each surface are similar since they are based on the main surface characteristics, such as overall shape and main gyri and sulci present at both time point, making it possible to define a correspondence.This correspondence was then used to investigate the longitudinal cortical folding in different brain regions by looking at the changes in curvature parameters such as the mean curvature. After statistical analysis, we found that the left temporal lobe and the left and right prefrontal cortex exhibited the most pronounced changes over the preterm period, which was consistent with our initial hypothesis. We expected more folding in these regions, since most of their development happens during the last trimester of pregnancy.

In Chapter 7, we applied the optimised spectral matching spectral pipeline of surface boundary to perform a shape analysis of the thalamus, cerebellum and white-grey matter boundary in a cohort of 60 extremely preterm young adults (all ages 19 year at the time of scanning) and 48 of their matched term controls. We investigated the shape differences between the two groups and found that although the cerebellum did not display any significant shape differences, the thalamus (upper and lateral side) and the cortex (temporal lobe) did, and these differences were more pronounced in male subjects. The differences in cortical folding were consistent with our previous findings from the extremely preterm born infants, where we found that the temporal lobe develops the most after the extremely preterm birth and it still presented a different degree of folding in adulthood when compared to adult controls. Furthermore, the results are in agreement with some of the previous studies on extreme prematurity in infants, children and young adults, studies that found that males are more affected by prematurity that females in terms of brain development and/or neurological outcome [89], [74], [43]. The results presented in this chapter represent the first findings in this cohort of extremely preterm young adults of structure analysis of shape.

It is important that preterm development is also investigated from other types of MR imaging, such as

diffusion, since it provides us with microstructural and connectivity information that cannot be investigated using T1-weighted MRI. In Chapter 8, we introduced spectral decomposition in the context of diffusion tensor images, by defining the nodes of the graph as voxels of DTI voxel connections through a tensor log-Euclidean similarity term [7]. We defined a correspondence for the diffusion tensor images using their diffusion tensor spectral representation (tensor spectral matching (TSM)), followed by a tensor orientation optimisation using DTI-TK [175]. This registration framework was successfully applied on both control adult data (atlas construction for validation) and on the longitudinal data of the 9 extremely preterm born infants, where it performed better DTI-TK, one of the state-of-art methods for tensor registration. This is the first time spectral decomposition has been extended to diffusion tensor images and, to the best of our knowledge, the first time a longitudinal registration of DTI of extremely preterm infants was performed. We used the newly proposed novel registration framework to investigate longitudinal development of white matter microstructure over the preterm period in a groupwise space defined using the same registration framework. We looked at the longitudinal changes of the deformation field brought into the same common space and noticed consistent changes morphometric microstructural changes over the preterm period in all infants, with the largest changes taking place in the corpus callosum and internal capsule. Thus these regions are likely to be affected by prematurity and influence the neurodevelopment in these infants, as well as the brain regions to which they are connected. Previous studies have found that corpus callosum abnormalities were likely to be correlated with motor functioning and reduced IQ [152], and carpus callosum abnormalities are have been associated with many metabolic diseases [41], thus motivating this type of research to understand their premature development.

Finally, in Chapter 9 we proposed a more generic multi-modal registration approach (PIMMS) for white-grey matter boundaries, based on spectral decomposition that uses both surface and diffusion information. The goal of PIMMS was to establish a more biologically meaningful correspondence based on both cortical surface features and structural information. This registration technique combined the surface spectral matching introduced in Chapter 6 and the tensor spectral matching from Chapter 8, by defining the surface-to-surface mapping in the image domain. To define the cortical surface in image space we took advantage of the level set representation of the surface boundary (in this case the WM/GM boundary) and reproduced the surface spectral matching in image space. This was the first time the spectral matching of surfaces was done in image space. We used PIMMS to define a new and more biologically meaningful groupwise average surface of the early time point of the 9 extremely preterm infants. We compared PIMMS against the surface-only joint-spectral matching and a multi-modal approach, Multi-contrast Multi-scale Surface Registration, and found that the registration error was smaller for PIMMS. We investigated the longitudinal changes in cortical thickness, cortical FA and cortical MD, as well as the interdependencies of these parameters. Again, the temporal lobe exhibited the most extreme changes, with a significant thinning of the cortex.

Overall, this thesis explores several steps for processing extremely preterm data for neuroimage analysis, enabling the study of longitudinal structural morphometry and microstructural features of this data. Two population specific brain atlases have been constructed for the post-mortem fetal population and

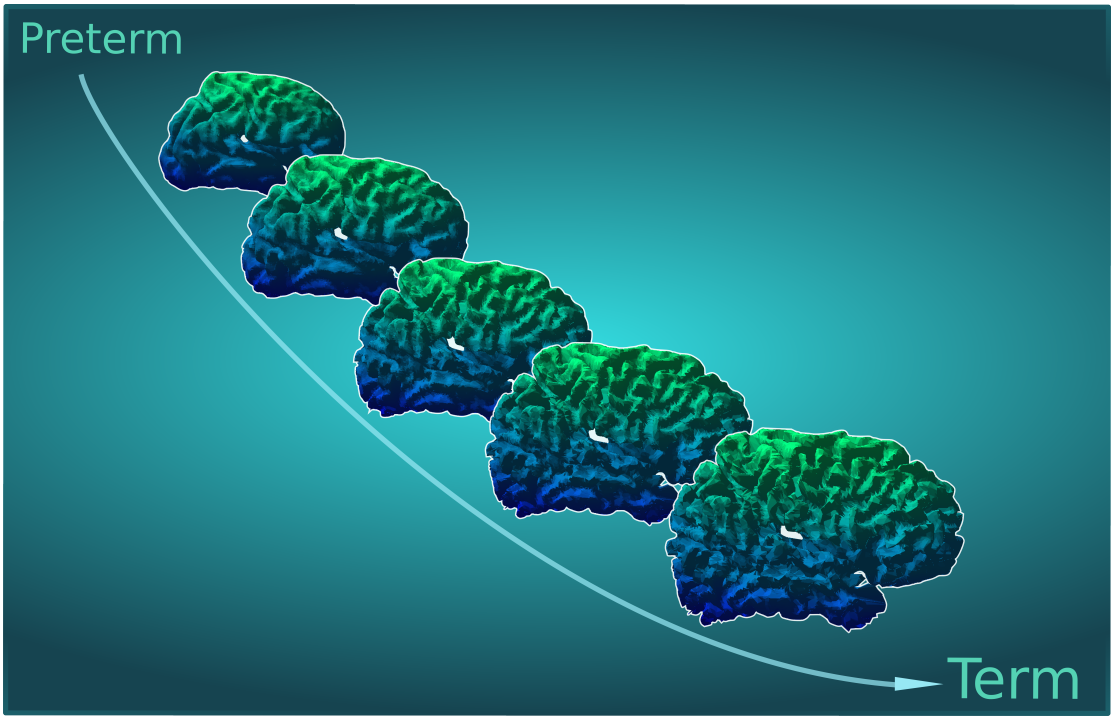

Figure 10.1: Brain development over the preterm period. Image was submitted to the ”Research Images as Art Competition” at University College London, November 2014.

extremely preterm born infants, and three novel registration algorithms were developed, for both mono- and multi-modal MR data. These algorithms are important for studying the fetal and extremely preterm brain, their development, as long as the long term impact caused by prematurity. Firstly, a lot can be learned by investigating this type of data about brain development and functions, and hopefully how it is all connected to the neurological outcome. Secondly, it is important that we understand the mechanism leading to this outcome. The matching of cortical surfaces allows the comparison of normal versus diseased development. The matching of diffusion tensors allows the matching of fibre bundles so one can understand changes in microstructure, such as axons, neurites, NODDI parameters, as well as changes in myelination, which can also be noticed from T2-weighted images. The multi-modal spectral matching will allow us to establish how all these processes (morphological and electrical) are occurring at the local level, how they are synchronised and how we can monitor any deviation from normal. It might also give us insight into the constraints on both large and small scale optimisations in terms of path length of the brain connections, signal sychronisation, energetic costs, network efficiency and the combined effect of path length and cortical folding. All these processes together might illuminate the understanding of this complex brain development.

The work developed in this thesis is of great importance for the neonatal community and specifically for the preterm community and has been well received at a series of conferences, workshops and journals.

10.2 Future Research Directions

Notwithstanding the novel methodology and analysis presented in this thesis, there are still some conceptual ideas associated with this work that are worth pursuing.

The main challenge regarding this work is that for all of the qualitatively good correspondences obtained by the proposed longitudinal spectral matching techniques, a validation is very difficult, as there is no principled way of establishing a ground truth. One possibility would be a manual validation by a trained neuroanatomist, but this would be limited to the most obvious landmarks. As is already known and proved in this thesis, several brain structures, both on the macro- and microstructural level, only emerge during the preterm period and are not present at the time of the first scan. Thus, we are assuming that the link can be established with shape geometry by inferring the locations where some gyri and sulci will appear, but this might not be entirely certain. Another way of possibly validating the established correspondences would be to have a similar cohort with more longitudinal time points and investigating if the composition of the registration of the first and last time points to the middle points is equivalent to the overall registration.

One of the main challenges in the field of preterm imaging is the lack of large cohorts, since any significant results might be hard to validate on a small cohort. Recruitment of extremely and very preterm neonates for research studies is quite a challenging task, particularly when attempting to obtain longitudinal data. Scanning preterm born infants is difficult since most of them spend a lot of time in the neonatal intensive care unit. Getting longitudinal information is even more challenging, since infants who undertake one of the scans may not be particularly fit for one of the other ones. Another more minor issue is that one would always end up correcting for age differences, since infants might need to be scanned at different time points, depending on their health status. Finally, extremely preterm birth remains a relatively rare event in the United Kingdom. I hope that in the future, with advances in healthcare, imaging software and hardware and improvements in the neonatal intensive care units, a larger amount of data can be acquired from extremely and very preterm born infants, scanned at multiple time points over the preterm period to help us fill in the blanks and unify the longitudinal analysis of preterm brain development. This would allow a proper modelling of their longitudinal development, making it possible to establish biomarkers for early brain development. Ideally, these infants would also be followed into childhood, adolescence and adulthood for a more complex model of their development, to get a clear insight into how extreme prematurity affects individuals on the long term. The techniques I have developed and presented in this thesis can be used for the study of longitudinal brain development of the preterm population, from birth until late adulthood. They could also be used to look at group differences between this population and term controls so that the differences from term brain development at all stages is clear.

The EPICure shape analysis of different brain structures presented in this thesis could be expanded. A groupwise analysis of the diffusion data using TSM could be performed, thus also looking into the microstructural differences between extremely preterm born young adults and term controls. It will be

interesting to explore how different brain structures and white matter tracts are influenced by premature birth. Previous studies on this cohort have looked into the diffusion properties of white matter using TBSS [48], perfusion and diffusion properties of the thalamus [92] and microstructural characteristics of the corpus callosum ([96]). All these findings can be correlated with the shape analysis findings. Shape analysis could also be performed for the corpus callosum, to connect it with the diffusion information obtained by [96]. The use of shape information will bridge the gap between tissue structure and macroscale tissue properties.

Lastly, with tools presented in this thesis, we could also model the early brain development from animals. We could acquire animal data more frequently than we can in preterm born infants and study brain development. Animal models still provide an essential way of providing insights into the mechanisms underlying the vulnerability of the developing brain to the changes in the environment [128] and help us validate our findings about brain development described in this thesis. Furthermore, animal models have made it possible to determine the effects of a specific insult that happened at a specific stage of development on the function or structure of the brain [128]. Comparing these outcomes with human neuropathologies and neurological disorders can provide some insight into possible causes and treatment that can be administered.

Over the short term, most of techniques I have developed will become publicly available, especially the surface spectral matching, the tensor spectral matching and the multi-modal spectral matching. I believe that the neonatal research community will benefit from this, but of course many other areas of neuroimaging can use these methods. For example, I believe they would be quite useful in modelling neurodegeneration and the progression of several diseases, such as Alzheimer's Disease and multiple sclerosis. Furthermore, they could also be used to investigate group differences between controls and pathology populations of different types (schizophrenia, ADHD, autism). Finally, these methods could also be used to monitor subjects pre- and post-surgery, who underwent brain tumours resections and not only. I plan to make publicly available also the the post-mortem atlases and preterm database that I have created, in the hope that they would benefit the segmentation of newer subjects, particularly those with similar characteristics to the ones presented in this thesis. Nonetheless, a pipeline describing the steps necessary to create new databases for other cohorts could be written and distributed.

Over the long term, the goal would be to further investigate our results and create an accurate model of brain development over the preterm period, incorporating all the different measures we looked into such as cortical folding, microstructural changes in the white matter, cortical thickness, cortical fractional anisotropy and cortical mean diffusivity, as well as linking the grey and white matter properties. Having a clear idea about how all these measures are dependent on each other may contribute to developing early biomarkers for predicting the executive and motor development of extremely preterm infants. We plan to investigate correlations between the white matter microstructural development and the morphological changes taking place in the cortex over the same timeframe. The techniques that I developed and presented in this thesis have put me in the perfect position to bring this different type of structural and

microstrucural information together and to, ideally, establish a comprehensive measurement of preterm brain development that can be used as a biomarker of disability.

Chapter 11

Appendix

Global Changes over the Preterm Period

This section presents additional global changes results over the preterm period in the Sparks dataset described in Section 3.2, unrelated with the spectral matching results and methods. These include the changes in all infants as a function of equivalent gestational age in volume and surface area for the whole brain and by region of interest (prefrontal cortex, temporal lobe, occipital lobe, parietal lobe) and a multivariate descriptor of curvature, all obtained from the triangle-based meshes of these surfaces (Section 6.1.2).

Volume and surface area over the preterm period

The volume and surface area change of the right and left hemispheres, prefrontal cortex and temporal lobe, respectively, were plotted against estimated gestational age for all 9 infants at the 2 different time points. By using a linear fit, we can estimate that the white matter surface area increase rate of the right hemisphere to be $25.79cm^2/week$ ($R^2 = 0.96$) and the slightly higher increasing rate for the left hemisphere to be $26.23cm^2/week$ ($R^2 = 0.97$) (Figure 11.1 (a)). We do not report a growth increase rate for the volume since a linear fit is not supported by the data ($R^2 < 0.85$) (Figure 11.1 (b)).

Furthermore, we can estimate the surface area increase rate of the left PFC to be $6.00cm^2/week$ ($R^2 = 0.98$) and the slightly higher increasing rate for the right PFC to be $6.21cm^2/week$ ($R^2 = 0.94$) (Figure 11.2 (a)). Similarly, the surface area increase rate of the left and right temporal lobe are found to be $3.44cm^2/week$ ($R^2 = 0.97$) and $3.20cm^2/week$ ($R^2 = 0.94$), respectively (Figure 11.3 (a)). The rates for the left and right hemispheres do not show any statistically significant asymmetry correlation at a 5% significance level ($p < 0.05$). We do not report a growth increase rate for the volume since a linear fit is not supported by the data ($R^2 < 0.85$) (Figures 11.2 (b) and 11.3 (b)). We notice the expected right-greater than-left asymmetry for the prefrontal cortex only.

We also report a surface area increase rate of the left occipital lobe of $3.86cm^2/week$ ($R^2 = 0.90$) and the slightly lower increasing rate for the right occipital lobe of $3.77cm^2/week$ ($R^2 = 0.88$). Similarly, we report a surface area increase rate of the left and right parietal lobes of $5.80cm^2/week$ ($R^2 = 0.97$)

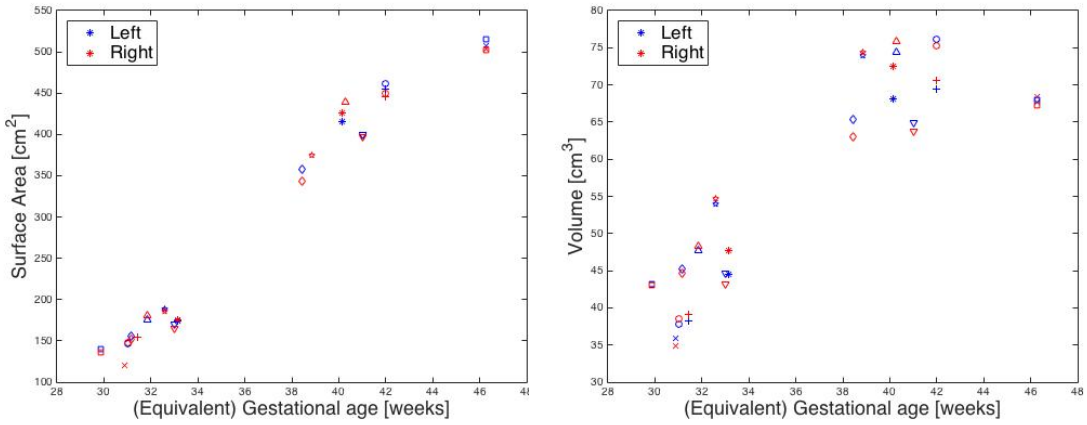

(a) Surface area change

(b) Volume change

Figure 11.1: Surface area and volume change for all 9 subjects of the left and right white matter as a function of EGA: blue represents the left hemisphere and red the right hemisphere. Subjects have unique marker identifiers: a - asterisk, b - addition sign, c - circle, d - cross, e - square, f - triangle, g - diamond; h - star; i - upside-down triangle

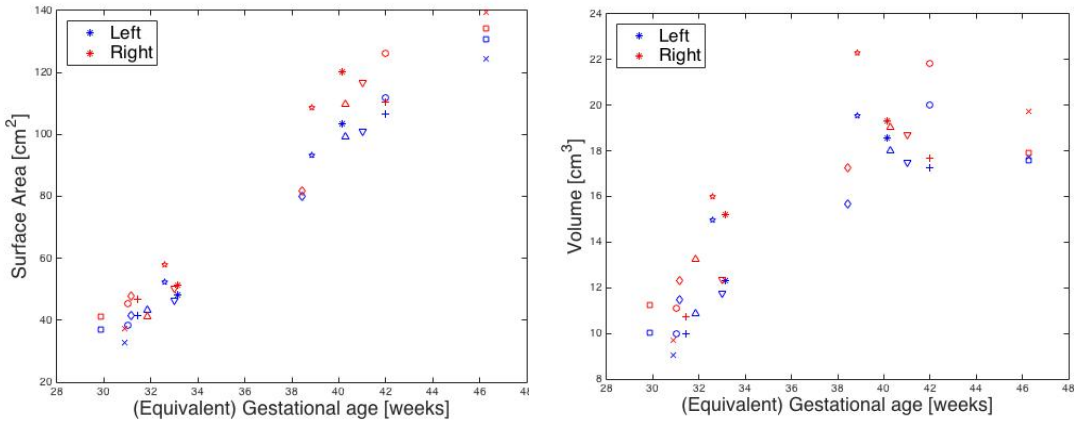

(a) Surface area change of prefrontal cortex

(b) Volume change of prefrontal cortex

Figure 11.2: Surface area and volume change for all 9 subjects of the left and right PFC as a function of EGA: blue represents the left hemisphere and red the right hemisphere. Subjects have unique marker identifiers: a - asterisk, b - addition sign, c - circle, d - cross, e - square, f - triangle, g - diamond; h - star; i - upside-down triangle

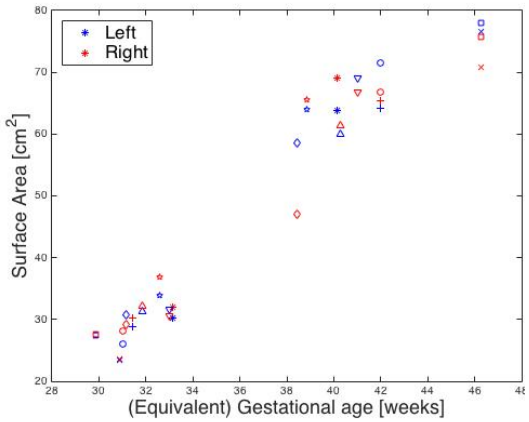

(a) Surface area change of temporal lobe

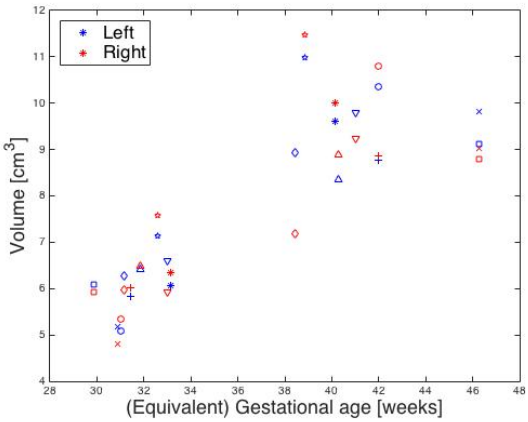

(b) Volume change of temporal lobe

Figure 11.3: Surface area and volume change for all 9 subjects of the left and right temporal lobe as a function of EGA: blue represents the left hemisphere and red the right hemisphere. Subjects have unique marker identifiers: a - asterisk, b - addition sign, c - circle, d - cross, e - square, f - triangle, g - diamond; h - star; i - upside-down triangle

and $5.59cm^2/week$ ($R^2 = 0.96$), respectively. Again we cannot report a linear growth increase rate for the volume since a linear fit is not supported by the data ($R^2 < 0.85$).

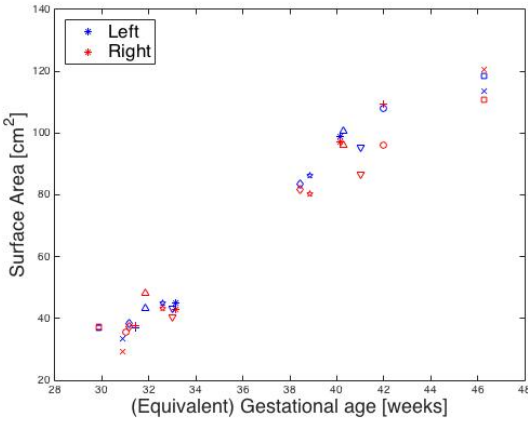

(a) Surface area change of parietal lobe

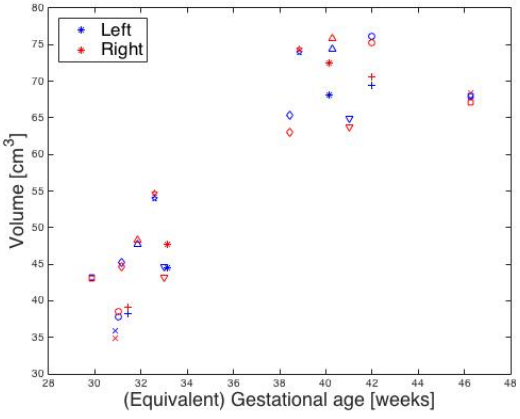

(b) Volume change of parietal lobe

Figure 11.4: Surface area and volume change for all 9 subjects of the left and right parietal lobe as a function of EGA: blue represents the left hemisphere and red the right hemisphere. Subjects have unique marker identifiers: a - asterisk, b - addition sign, c - circle, d - cross, e - square, f - triangle, g - diamond; h - star; i - upside-down triangle

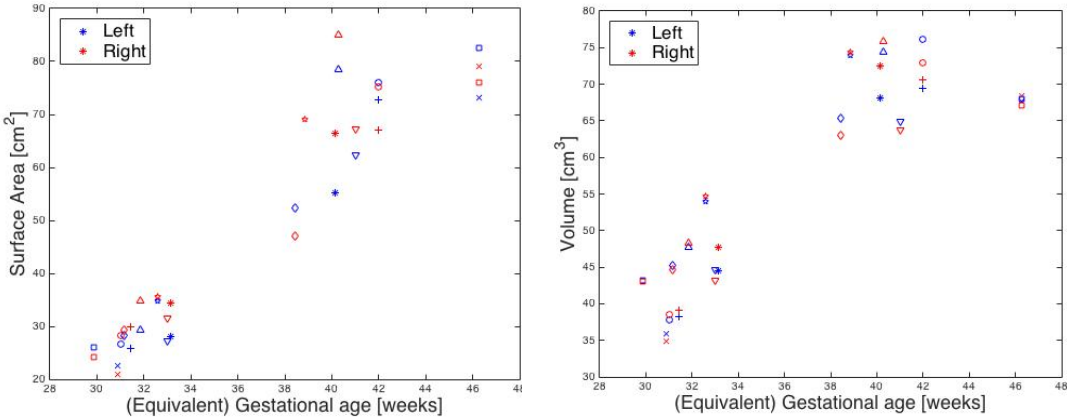

(a) Surface area change of occipital lobe

(b) Volume change of occipital lobe

Figure 11.5: Surface area and volume change for all 9 subjects of the left and right occipital lobe as a function of EGA: blue represents the left hemisphere and red the right hemisphere. Subjects have unique marker identifiers: a - asterisk, b - addition sign, c - circle, d - cross, e - square, f - triangle, g - diamond; h - star; i - upside-down triangle

Multivariate folding descriptor

We used the shape index and curvedness to compute the joint PDF $P(C, S)$ as the multivariate high-dimensional descriptor of cerebral cortical folding patterns of a surface as proposed by [8]. Additionally to investigating this descriptor, we also looked at the group difference of the measures (S and C) between the two time points using the correspondence obtained in Chapter 6 and calculated the descriptors for this.

Figures 11.6, 11.7 and 11.8 show the group folding complexity and shape index of the whole brain white matter, prefrontal cortex and temporal lobe, at the two time points. The left and right half of this descriptor represent the convex and concave patches, respectively, and the colour scale represents the density of mesh nodes. It can be noticed how the whole brain white matter and the white matter of both regions evolve from a less folded, convex shape (11.6 a, d; 11.7 a, d and 11.8 a, d, where the left half, the convex one, is red i.e. higher node density) to a much more folded, concave surface (11.6 b, e; 11.7 b, e and 11.8 b, e), where the right half, the concave one, is now red, related to deeper sulci and/or larger sulci number).

Additionally, from the multivariate folding descriptors group differences of the prefrontal cortex (11.7 c and f) we notice how the the right PFC exhibits more sulcation and folding than the left PFC (the group difference descriptor of the right PFC show a larger red left half than the descriptor of the left PFC). This result is in agreement with the results from Section 11, where we found the the right PFC develops more than the right PFC during the preterm period in terms of volume and surface area. The opposite effect is observed from the multivariate folding descriptors group differences of the temporal lobe 11.8 c and f), where the left temporal lobe shows more folding than the right temporal lobe, in agreement with results

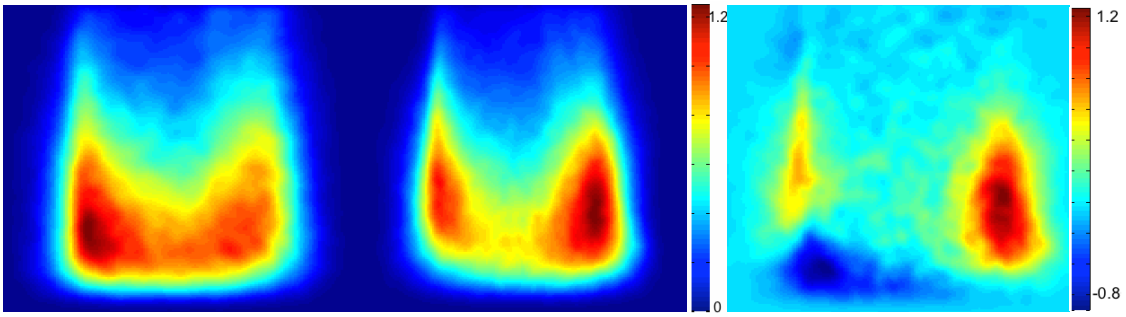

(a) Group Preterm left (b) Group Term left (c) Group Difference left

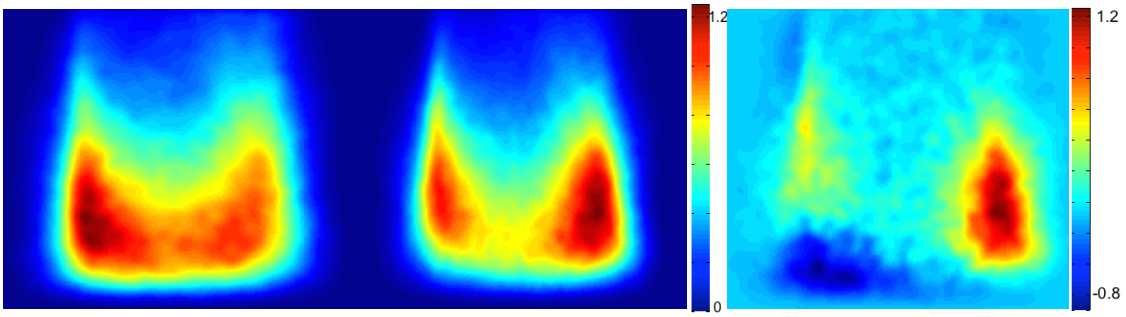

(d) Group Preterm right (e) Group Term right (f) Group Difference right

Figure 11.6: Group mean of the multivariate surface descriptors P(C,S) for the whole brain white matter left (a-c) and right (d-f). For all plots, horizontal axis = S, vertical axis = C. The left and right half of this descriptor represent the convex and concave patches, respectively, and the colour scale represents the density of mesh nodes.

from Section 11. No significant right-left folding asymmetry was found for the whole brain white matter (11.6 c and f).

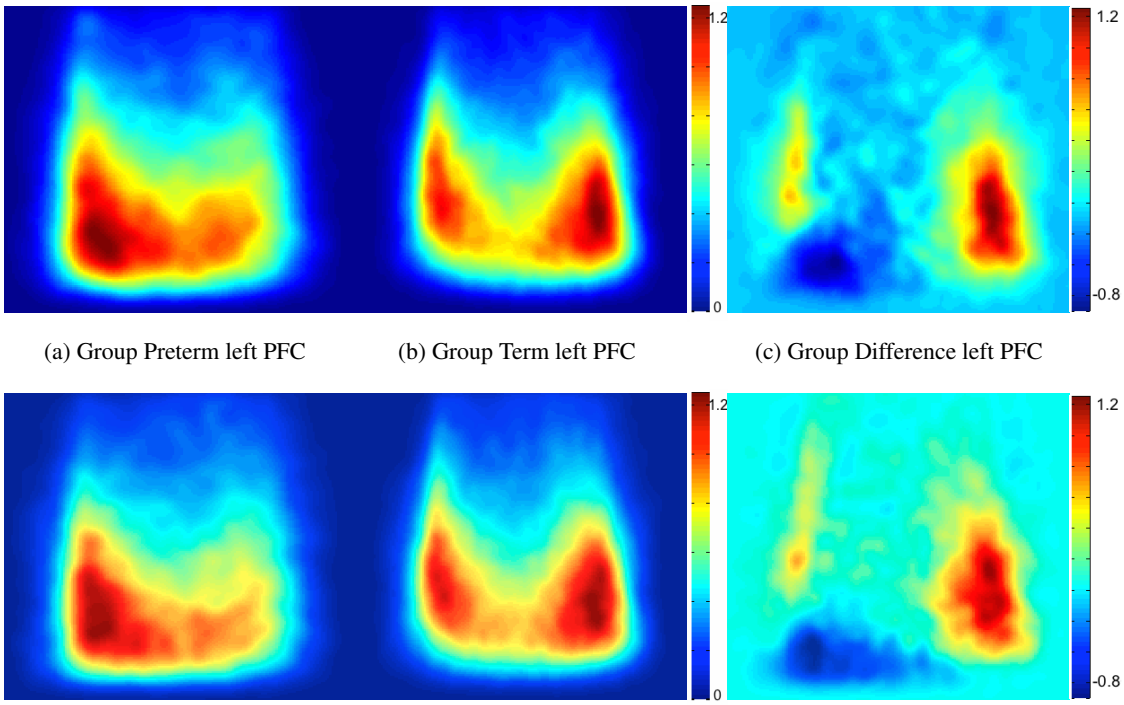

(a) Group Preterm left PFC (b) Group Term left PFC (c) Group Difference left PFC

(d) Group Preterm right PFC (e) Group Term right PFC (f) Group Difference right PFC

Figure 11.7: Group mean of the multivariate surface descriptors P(C,S) for the prefrontal cortex left (a-c) and right (d-f). For all plots, horizontal axis = S, vertical axis = C. The left and right half of this descriptor represent the convex and concave patches, respectively, and the colour scale represents the density of mesh nodes.

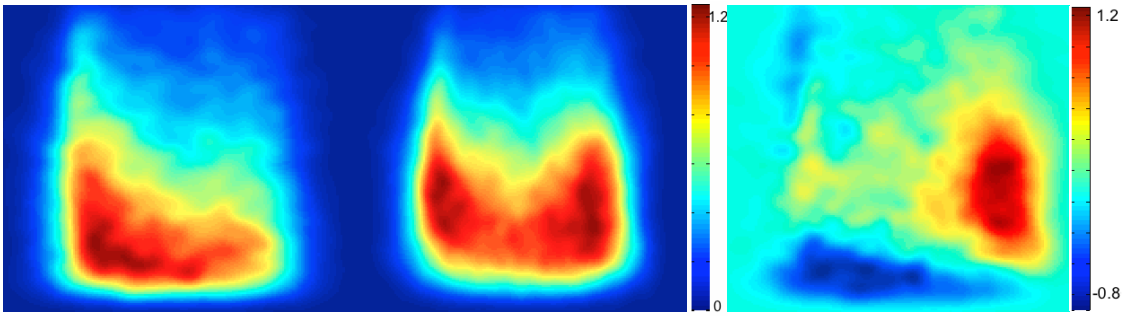

(a) Group Preterm left Temporal (b) Group Term left Temporal (c) Group Difference left Temporal

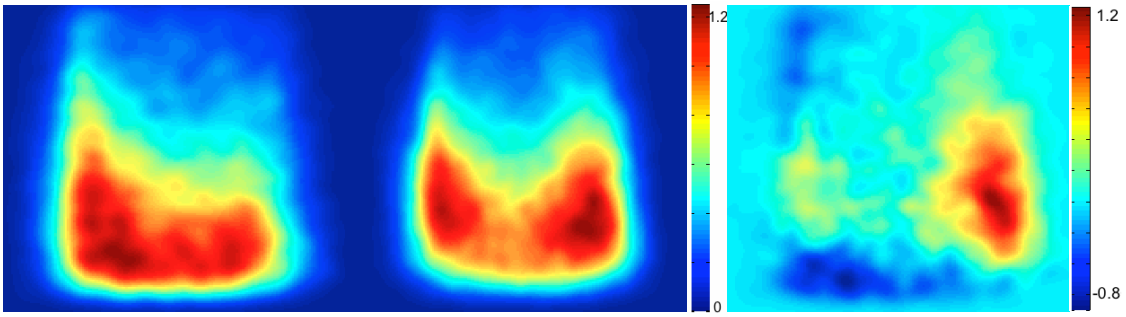

(d) Group Preterm right Temporal (e) Group Term right Temporal (f) Group Difference righ Temporal

Figure 11.8: Group mean of the multivariate surface descriptors P(C,S) for temporal left (a-c) and right (d-f). For all plots, horizontal axis = S, vertical axis = C. The left and right half of this descriptor represent the convex and concave patches, respectively, and the colour scale represents the density of mesh nodes.

Bibliography

[1] Shea Addison, Owen J Arthurs, and Sudhin Thayyil. Post-mortem MRI as an alternative to non-forensic autopsy in foetuses and children: from research into clinical practice. *The British Journal of Radiology*, 87(1036), 2014.

[2] Daniel C Alexander, Carlo Pierpaoli, Peter J Basser, and James C Gee. Spatial transformations of diffusion tensor magnetic resonance images. *IEEE Transactions on Medical Imaging*, 20(11):1131–1139, 2001.

[3] David C Alsop, John A Detre, Xavier Golay, Gunther Matthias, Jeroen Hendrikse, Luis Hernandez-Garcia, Hanzhang Lu, Bradley J Macintosh, Laura M Parkes, Marion Smits, Matthias J P Van Osch, Danny J J Wang, Eric C Wong, and Greg Zaharchuk. Recommended Implementation of Arterial Spin-Labeled Perfusion MRI for Clinical Applications: A Consensus of the ISMRM Perfusion Study Group and the European Consortium for ASL in Dementia. *Magnetic Resonance in Medicine*, 73(1):102–116, 2015.

[4] Katrin Amunts, Axel Schleicher, and Karl Zilles. Cytoarchitecture of the cerebral cortex - More than localization. *NeuroImage*, 37(4):1061–1065, 2007.

[5] Petronella Anbeek, Koen L Vincken, Floris Groenendaal, Anneke Koeman, Matthias J P Van Osch, and Jeroen Van der Grond. Probabilistic Brain Tissue Segmentation in Neonatal Magnetic Resonance Imaging. *Pediatric Research*, 63(2):158–163, 2008.

[6] Cody C Arnold, Michael S Kramer, Charlotte A Hobbs, Frances H McLean, and Robert H Usher. Very Low Birth Weight: A Problematic Cohort for Epidemiologic Studies of Very Small or Immature Neonates. *American Journal of Epidemiology*, 134(6):604–613, 1991.

[7] Vincent Arsigny, Pierre Fillard, Xavier Pennec, and Nicholas Ayache. Log-Euclidean metrics for fast and simple calculus on diffusion tensors. *Magnetic Resonance in Medicine*, 56(April):411–421, 2006.

[8] Suyash P Awate, Paul Yushkevich, Zhuang Song, Daniel J Licht, and James C Gee. Cerebral cortical folding analysis with multivariate modeling and testing: Studies on gender differences and neonatal development. *NeuroImage*, 53(2):450–459, 2010.

[9] Glen P Aylward, Steven I Pfeiffer, Anne Wright, and Steven J Verhulst. Outcome studies of low birth weight infants published in the last decade: A metaanalysis. *The Journal of Pediatrics*, 115(4):515–520, 1989.

[10] Gareth Ball, James P Boardman, Daniel Rueckert, Paul Aljabar, Tomoki Arichi, Nazakat Merchant, Ioannis S Gousias, a David Edwards, and Serena J Counsell. The effect of preterm birth on thalamic and cortical development. *Cerebral Cortex*, 22(5):1016–24, 2012.

[11] Gareth Ball, Latha Srinivasan, Paul Aljabar, Serena J Counsell, Giuliana Durighel, Joseph V Hajnal, Mary a Rutherford, and a David Edwards. Development of cortical microstructure in the preterm human brain. *Proceedings of the National Academy of Sciences of the United States of America*, 110(23):9541–9646, 2013.

[12] Peter J Basser, James Mattiello, and Denis Lebihan. MR Diffusion Tensor Spectroscopy and Imaging. *Biophysical Journal*, 66(January):259–267, 1994.

[13] Mark E Bastin, Devasuda Anblagan, Sarah Sparrow, Emma Moore, Rozi Pataky, and Chinthika Piyasena. Using Diffusion MRI and Quantitative Tractography to Investigate Gender Specific Effects on the Development of White Matter after Preterm Birth at 3T. *Magnetom Flash*, pages 42–44, 2014.

[14] Pierre-Louis Bazin, Marcel Weiss, Juliane Dinse, Andreas Schäfer, Robert Trampel, and Robert Turner. A computational framework for ultra-high resolution cortical segmentation at 7 Tesla. *NeuroImage*, 93:201–209, 2014.

[15] MF Beg, MI Miller, A Trouvé, and L Younes. Computing large deformation metric mappings via geodesic flows of diffeomorphisms. *International Journal of Computer Vision*, 61(2):139–157, 2005.

[16] Duane D Blatter, Erin D Bigler, Shawn D Gale, Sterling C Johnson, Carol V Anderson, Bruce M Burnett, Natalie Parker, Shanna Kurth, and Susan D Horn. Quantitative Volumetric Analysis of Brain MR: Normative Database Spanning 5 Decades of Life. *American Journal of Neuroradiology*, pages 241–252, 1995.

[17] James P Boardman, Serena J Counsell, Daniel Rueckert, Olga Kapellou, Kanwal K Bhatia, Paul Aljabar, Jo Hajnal, Joanna M Allsop, Mary A Rutherford, and A David Edwards. Abnormal deep grey matter development following preterm birth detected using deformation-based morphometry. *NeuroImage*, 32:70–78, 2006.

[18] James P Boardman, Cathy Craven, Sabeel Valappil, Serena J Counsell, Leigh E Dyet, Daniel Rueckert, Paul Aljabar, Mary Rutherford, Andrew T M Chew, Joanna M Allsop, Frances M Cowan, and A David Edwards. A common neonatal image phenotype predicts adverse neurodevelopmental outcome in children born preterm. *NeuroImage*, 52(2):409–414, 2010.

[19] J. A. Bondy and U. S. R. Murty. *Graph Theory with Applications*. The Macmillan Press Ltd., 1976.

[20] Linda D Breeman, Julia Jaekel, Nicole Baumann, Peter Bartmann, and Dieter Wolke. Attention problems in very preterm children from childhood to adulthood: the Bavarian Longitudinal Study. *The Journal of Child Psychology and Psychiatry*, 57(2):132–140, 2016.

[21] Andrew C G Breeze, Justin J Cross, G. A. Hackett, F. A. Jessop, I. Joubert, D J Lomas, P. A. K. Set, A. L. Whitehead, and C. C. Lees. Use of a confidence scale in reporting postmortem fetal magnetic resonance imaging. *Ultrasound in Obstetrics and Gynecology*, 28(7):918–24, dec 2006.

[22] Andrew C G Breeze, F. A. Gallagher, D. J. Lomas, G. C. S. Smith, and C. C. Lees. Postmortem fetal organ volumetry using magnetic resonance imaging and comparison to organ weights at conventional autopsy. *Ultrasound in Obstetrics and Gynecology*, 31(2):187–93, feb 2008.

[23] L Breysem, H Bosmans, S Dymarkowski, D Van Schoubroeck, I Witters, Jan Deprest, P Demaerel, D Vanbeckevoort, C Vanhole, P Casaer, and M Smet. The value of fast MR imaging as an adjunct to ultrasound in prenatal diagnosis. *European Radiology*, 13(7):1538–1548, 2003.

[24] Betty Ann Brody, Hannah C. Kinney, Alexander S. Kloman, and Floyd H. Gilles. Sequence of Central Nervous System Myelination in Human Infancy: An Autopsy Study of Myelination. *Journal of Neuropathology and Experimental Neurology*, 46(3):283–301, 1987.

[25] William M Callaghan, Marian F Macdorman, Sonja A Rasmussen, Cheng Qin, and Eve M Lackritz. The Contribution of Preterm Birth to Infant Mortality Rates in the United States. *Pediatrics*, 118(4), 2006.

[26] M Cannie, J Jani, S Dymarkowski, and Jan Deprest. Fetal magnetic resonance imaging: luxury or necessity? *Ultrasound in Obstetrics and Gynecology*, 27:471–476, 2006.

[27] Yan Cao, Michael I. Miller, Raimond L. Winslow, and Laurent Younes. Large deformation diffeomorphic metric mapping of fiber orientations. *Proceedings of the IEEE International Conference on Computer Vision*, II(9):1379–1386, 2005.

[28] M Jorge Cardoso, Andrew Melbourne, Giles S Kendall, Marc Modat, Nicola J Robertson, Neil Marlow, and Sebastien Ourselin. AdaPT: An adaptive preterm segmentation algorithm for neonatal brain MRI. *NeuroImage*, 65:97–108, jan 2013.

[29] M Jorge Cardoso, Marc Modat, Robin Wolz, Andrew Melbourne, David Cash, and Daniel Rueckert. Geodesic Information Flows: Spatially-Variant Graphs and Their Application to Segmentation and Fusion. *IEEE Transactions on Medical Imaging*, 34(9):1976–1988, 2015.

[30] Centre for Maternal and Child Enquiries (CMACE). Perinatal Mortality 2009: United Kingdom. Technical Report March, London, 2011.

[31] Vann Chau, Rollin Brant, Kenneth J Poskitt, Emily W Y Tam, Anne Synnes, and Steven P Miller. Postnatal infection is associated with widespread abnormalities of brain development in premature newborns. *Pediatric Research*, 71(3):274–279, 2012.

[32] Xin Chen and Francis Schmitt. Intrinsic Surface Properties from Surface Triangulation. In *Computer Vision ECCV*, number 588, pages 739–743, 1992.

[33] J G Chi, E C Dooling, and F H Gilles. Gyral development of the human brain. *Annals of Neurology*, 1(1):86–93, jan 1977.

[34] Fan R K Chung. *Spectral Graph Theory*. AMS & CBMS, 1997.

[35] Cedric Clouchoux, Nicolas Guizard, Alan Charles Evans, Adre Jacques du Plessis, and Catherine Limperopoulos. Normative fetal brain growth by quantitative in vivo magnetic resonance imaging. *American Journal of Obstetrics and Gynecology*, 206(2):173–178, feb 2012.

[36] Marta C Cohen, Martyn N Paley, Paul D Griffiths, and Elspeth H Whitby. Less Invasive Autopsy: Benefits and Limitations of the Use of Magnetic Resonance Imaging in the Perinatal Postmortem. *Pediatric and Developmental Pathology*, 11(1):1–9, mar 2007.

[37] J Cohen-Adad. What can we learn from T2* maps of the cortex? *NeuroImage*, 93:189–200, 2014.

[38] Alain Combes, Mourad Mokhtari, Anne Couvelard, Jean-Louis Trouillet, Jerome Baudot, Dominique Henin, Claude Gilbert, and Jean Chastre. Clinical and Autopsy Diagnoses in the Intensive Care Unit. *Archives of Internal Medicine*, 164, 2004.

[39] Bryan R Conroy, Benjamin D Singer, J Swaroop Guntupalli, Peter J Ramadge, and James V Haxby. NeuroImage Inter-subject alignment of human cortical anatomy using functional connectivity. *NeuroImage*, 81:400–411, 2013.

[40] Kate Costeloe, Enid Hennessy, Alan T Gibson, Neil Marlow, and Andrew R Wilkinson. The EPICure Study: Outcomes to Discharge From Hospital for Infants Born at the Threshold of Viability. *Pediatrics*, 106(4), 2000.

[41] Frances M Cowan and Linda S De Vries. The internal capsule in neonatal imaging. *Seminars in Fetal and Neonatal Medicine*, 10(5):461–474, 2005.

[42] Andreas Dedner, L Marcel, Thomas Albrecht, and Thomas Vetter. Adaptive Finite Elements. In *Pattern Recognition*, pages 527–536, 2007.

[43] Nicholas Dingwall, Alan Chalk, Teresa I Martin, Catherine J Scott, Carla Semedo, Quan Le, Eliza Orasanu, Jorge M Cardoso, Andrew Mel, Neil Marlow, and Sebastien Ourselin. T2 relaxometry in the extremely-preterm brain at adolescence. *Magnetic Resonance Imaging*, 2015.

[44] Chen-shi Dong and Guo-zhao Wang. Curvatures estimation on triangular mesh. *Journal of Zhejiang University SCIENCE*, 6(Suppl. I):128–136, aug 2005.

[45] Jessica Dubois, Ghislaine Dehaene-Lambertz, S Kulikova, Cyril Poupon, Petra S Hüppi, and Lucie Hertz-Pannier. The early brain development of brain white matter: a review of imaging studies in fetuses, newborns and infants. *Neuroscience*, 276:48–71, 2014.

[46] Jessica Dubois, Ghislaine Dehaene-Lambertz, Muriel Perrin, Jean François Mangin, Yann Cointepas, Edouard Duchesnay, Denis Le Bihan, and Lucie Hertz-Pannier. Asynchrony of the early maturation of white matter bundles in healthy infants: Quantitative landmarks revealed noninvasively by diffusion tensor imaging. *Human Brain Mapping*, 29(1):14–27, 2008.

[47] Zach Eaton-Rosen, M Jorge Cardoso, Andrew Melbourne, Eliza Orasanu, Giles S Kendall, Nicola J Robertson, Neil Marlow, and Sebastien Ourselin. Fitting parametric models of diffusion MRI in regions of partial volume. In *SPIE Medical Imaging*, volume 9784, pages 1–9, 2016.

[48] Zach Eaton-Rosen, Andrew Melbourne, Eliza Orasanu, Joanne Beckmann, Nicola Stevens, David Atkinson, Neil Marlow, and Sebastien Ourselin. White matter alterations in young adults born extremely preterm: a microstructural point of view. In *ISMRM*, 2016.

[49] Zach Eaton-Rosen, Andrew Melbourne, Eliza Orasanu, M Jorge Cardoso, Marc Modat, Alan Bainbridge, Giles S Kendall, Nicola J Robertson, Neil Marlow, and Sebastien Ourselin. Longitudinal measurement of the developing grey matter in preterm subjects using multi-modal MRI. *NeuroImage*, 111:580–589, 2015.

[50] E Elsme, I Hansen Pupp, and L Hellstro. Preterm male infants need more initial respiratory and circulatory support than female infants. *Acta Pediatric*, 93:529–533, 2004.

[51] Erin Engelhardt, Terrie E Inder, Dimitrios Alexopoulos, Donna L Dierker, Jason Hill, David Van Essen, and Jeffrey J Neil. Regional Impairments of Cortical Folding in Premature Infants. *Annals of Neurology*, 77(1):154–162, 2015.

[52] Douglas E Fields. White Matter. *Brain Science*, (March):54–61, 2008.

[53] B Fischl, Martin I Sereno, R B Tootell, and M Dale. High-resolution intersubject averaging and a coordinate system for the cortical surface. *Human Brain Mappingrain mapping*, 8(4):272–284, jan 1999.

[54] D Fraello, Jill Maller-Kesselman, and Betty Vohr. Consequence of preterm birth in early adolescence: the role of language on auditory short-term memory. *Journal of Child Neurolgy*, 26:738–742, 2011.

[55] R S Gibbs, R Romero, S L Hillier, D A Eschenbach, and R L Swer. A review of premature birth and subclinical infection. *American Journal of Obstetrics and Gynecology*, 166(5):1515–1528, 1992.

[56] Monica Gimenez, Carme Junque, Ana Narberhaus, Francesc Botet, and Josep Maria Mercader. White matter volume and concentration reductions in adolescents with history of very preterm birth: A voxel-based morphometry study. *NeuroImage*, 32(4):1485–1498, 2006.

[57] Nadine J Girard, Philippe Dory-Lautrec, Mériam Koob, and Anca Melania Dediu. MRI assessment of neonatal brain maturation. *Imaging in Medicine*, 4(6):613–632, dec 2012.

[58] Matthew F Glasser and David C Van Essen. Mapping Human Cortical Areas In Vivo Based on Myelin Content as Revealed by T1- and T2-Weighted MRI. *Journal of Neuroscience*, 31(32):11597–11616, 2011.

[59] Leo J Grady and J Polimeni. *Discrete calculus: Applied analysis on graphs for computational science*. Springer Science & Business Media, 2010.

[60] Paul D Griffiths, Dick Variend, Margaret Evans, Angharad Jones, Iain D Wilkinson, Martyn N J Paley, and Elspeth Whitby. Postmortem MR imaging of the fetal and stillborn central nervous system. *American Journal of Neuroradiology*, 24(1):22–7, jan 2003.

[61] Piotr A Habas, Kio Kim, Francois Rousseau, Orit A Glenn, A James Barkovich, and Colin Studholme. A spatio-temporal atlas of the human fetal brain with application to tissue segmentation. *Medical Image Computing and Computer-Assisted Intervention (MICCAI)*, 12(Pt 1):289–96, 2009.

[62] Xiao Han, Dzung L Pham, Duygu Tosun, Maryam E Rettmann, Chenyang Xu, and Jerry L Prince. CRUISE: Cortical reconstruction using implicit surface evolution. *NeuroImage*, 23:997–1012, 2004.

[63] Xiao Han, Chenyang Xu, Ulisses Braga-neto, Jerry L Prince, and Senior Member. Topology Correction in Brain Cortex Segmentation Using a Multiscale, Graph-Based Algorithm. *IEEE Transactions on Medical Imaging*, 21(2):109–121, 2002.

[64] Jamie L Hanson, Nicole Hair, Dinggang G Shen, Feng Shi, John H Gilmore, Barbara L Wolfe, and Seth D. Pollak. Family poverty affects the rate of human infant brain growth. *PLoS ONE*, 8(12):e0146434, 2013.

[65] Gabrielle J Hindmarsh, Michael J O Callaghan, Heather A Mohay, and Yvonne M Rogers. Gender differences in cognitive abilities at 2 years in ELBW infants. *Early Human Development*, 60:115–122, 2000.

[66] Donna L. Hoyert and Elizabeth C.W. Gregory. Cause of Fetal Death: Data From the Fetal Death. Technical Report 7, National Vital Statistics Reports, 2016.

[67] Emer J Hughes, Jacqueline Bond, Patricia Svrckova, Antonis Makropoulos, Gareth Ball, David J Sharp, A David Edwards, Joeseph V Hajnal, and Serena J Counsell. Regional changes in thalamic shape and volume with increasing age. *NeuroImage*, 63(3):1134–1142, 2012.

[68] Thierry A G M Huisman. Magnetic resonance imaging: an alternative to autopsy in neonatal death? *Seminars in Neonatology*, 9(4):347–53, 2004.

[69] Petra S Hüppi and Jessica Dubois. Diffusion tensor imaging of brain development. *Seminars in Fetal & Neonatal Medicine*, 11:489–497, 2006.

[70] Terrie E Inder, Simon K Warfield, Hong Wang, and Petra S Hu. Abnormal Cerebral Structure Is Present at Term in Premature Infants. *Pediatrics*, 115(2), 2005.

[71] Derek K Jones, Thomas R Knösche, and Robert Turner. White matter integrity, fiber count, and other fallacies: The do's and don'ts of diffusion MRI. *NeuroImage*, 73:239–254, 2013.

[72] Pushkar Joshi and Carlo Séquin. Energy Minimizers for Curvature-Based Surface Functionals. *Computer-Aided Design and Applications*, 4(5):607–617, 2007.

[73] Olga Kapellou, Serena J. Counsell, Nigel Kennea, Leigh Dyet, Nadeem Saeed, Jaroslav Stark, Elia Maalouf, Philip Duggan, Morenike Ajayi-Obe, Jo Hajnal, Joanna M. Allsop, James Boardman, Mary a. Rutherford, Frances Cowan, and a. David Edwards. Abnormal cortical development after premature birth shown by altered allometric scaling of brain growth. *PLoS Medicine*, 3(8):1382–1390, 2006.

[74] Shelli R Kesler, Allan L Reiss, Betty Vohr, Christa Watson, Karen C Schneider, Katz Karold H, Jill Maller-Kesselman, John Silbereis, R Todd Constable, Robert W Makuch, and Laura R Ment. Brain Volume Reductions within multiple Cognitive Systems in Male Preterm Children at Age Twelve. *The Journal of Pediatrics*, 152(4):513–520, 2008.

[75] Shelli R Kesler, Betty Vohr, Karen C Schneider, Karol H Katz, Robert W Makuch, Allan L Reiss, and Laura R Ment. Increased temporal lobe gyrification in preterm children. *Neuropsychologia*, 44(3):445–53, 2006.

[76] Tat Yung Khong. A review of perinatal autopsy rates worldwide, 1960s to 1990s. *Paediatric and Perinatal Epidemiology*, 10(1):97–109, 1996.

[77] Rebecca C Knickmeyer, Sylvain Gouttard, Chaeryon Kang, Dianne Evans, Kathy Wilber, J Keith Smith, Robert M Hamer, Weili Lin, Guido Gerig, and John H Gilmore. A structural MRI study of human brain development from birth to 2 years. *The Journal of Neuroscience*, 28(47):12176–12182, 2008.

[78] Stine K Krogsrud, Anders M Fjell, Christian K Tamnes, Håkon Grydeland, Lia Mork, Paulina Due-tønnessen, Atle Bjørnerud, Cassandra Sampaio-baptista, Jesper Andersson, Heidi Johansen-berg, and Kristine B Walhovd. NeuroImage changes in white matter microstructure in the developing brain - A longitudinal diffusion tensor imaging study of children from 4 to 11 years of age. *NeuroImage*, 124:473–486, 2016.

[79] Maria Kuklisova-Murgasova, Paul Aljabar, Latha Srinivasan, Serena J Counsell, Valentina Doria, Ahmed Serag, Ioannis S Gousias, James P Boardman, Mary Rutherford, David Edwards, Joseph V Hajnal, and Daniel Rueckert. A dynamic 4D probabilistic atlas of the developing brain. *NeuroImage*, 54(4):2750–63, 2011.

[80] P J Lally, O J Arthurs, S Addison, N J Sebire, A Alavi, A M Taylor, and S Thayyil. Perinatal Virtopsy and miscellaneous fetal abdomen. *Journal of Forensic Radiology and Imaging*, 2(2):99, 2014.

[81] Alexander Leemans and Derek K Jones. The B-Matrix Must Be Rotated When Correcting for Subject Motion in DTI Data. *Magnetic Resonance in Medicine*, 61(6):1336–1349, 2009.

[82] Catherine Limperopoulos, Janet S Soul, Kimberlee Gauvreau, Petra S Hüppi, Simon K Warfield, Haim Bassan, Richard L Robertson, Joseph J Volpe, and Adré J du Plessis. Late gestation cerebellar growth is rapid and impeded by premature birth. *Pediatrics*, 115(3):688–95, 2005.

[83] Herve Lombaert, Michael Arcaro, and Nicholas Ayache. Brain Transfer: Spectral Analysis of Cortical Surfaces and Functional Maps. In *Information Processing in Medical Imaging*, pages 1–12, 2015.

[84] Herve Lombaert, Leo Grady, Xavier Pennec, Nicholas Ayache, and Farida Cheriet. Spectral demons - Image registration via global spectral correspondence. *International Journal of Computer Vision*, 7573:30–44, 2012.

[85] Herve Lombaert, Leo Grady, J Polimeni, and Farida Cheriet. FOCUSR: Feature Oriented Correspondence using Spectral Regularization-A Method for Accurate Surface Matching. *IEEE Transactions on Pattern Analysis and Machine Intelligence*, (99):1–18, 2012.

[86] Herve Lombaert, Leo Grady, JR Polimeni, and Farida Cheriet. Fast brain matching with spectral correspondence. In *Information Processing in Medical Imaging*, pages 660–673, 2011.

[87] Herve Lombaert, Jon Sporring, and Kaleem Siddiqi. Diffeomorphic spectral matching of cortical surfaces. In *Information Processing in Medical Imaging*, volume 7917, pages 376–389, 2013.

[88] Christine Lucas Tardif, Andreas Schäfer, Miriam Waehnert, Juliane Dinse, Robert Turner, and Pierre-Louis Bazin. Multi-contrast multi-scale surface registration for improved alignment of cortical areas. *NeuroImage*, 111:107–122, 2015.

[89] Neil Marlow, Dieter Wolke, Melanie A Bracewell, and Muthanna Samara. Neurologic and Developmental Disability at Six Years of Age after Extremely Preterm Birth. *New England Journal of Medicine*, 352(1):9–19, 2005.

[90] John C. Mazziotta, Arthur W. Toga, Alan Evans, Peter Fox, and Jack Lancaster. Probabilistic Atlas of the Human Brain: Theory and Rationale for Its Development. *NeuroImage*, 2:89–101, 1995.

[91] Donald W McRobbie, Elizabeth A Moore, Martin J Graves, and Martin R Prince. *MRI From Picture to Proton*. Cambridge University Press, 2006.

[92] Andrew Melbourne, Zach Eaton-Rosen, Eliza Orasanu, Joanne Beckmann, Alexandra Saborowska, David Atkinson, Neil Marlow, and Sebastien Ourselin. Perfusion and diffusion in the extremely preterm young adult thalamus. In *ISMRM*, 2016.

[93] Andrew Melbourne, Zach Eaton-Rosen, Eliza Orasanu, David Price, Alan Bainbridge, M Jorge Cardoso, Giles S Kendall, Nicola J Robertson, Neil Marlow, and Sebastien Ourselin. Longitudinal Development in the Preterm Thalamus and Posterior White Matter: MRI Correlations Between Diffusion Weighted Imaging and T2 Relaxometry. *Human Brain Mapping*, 2492(3):2479–2492, 2016.

[94] Andrew Melbourne, Giles S Kendall, M Jorge Cardoso, Roxanna Gunney, Nicola J Robertson, Neil Marlow, and Sebastien Ourselin. Radial Structure in the Preterm Cortex; Persistence of the Preterm Phenotype at Term Equivalent Age. In *Medical Image Computing and Computer-Assisted Intervention (MICCAI)*, pages 256–263, 2012.

[95] Andrew Melbourne, Giles S Kendall, M Jorge Cardoso, Roxanna Gunny, Nicola J Robertson, Neil Marlow, and Sebastien Ourselin. Preterm birth affects the developmental synergy between cortical folding and cortical connectivity observed on multimodal MRI. *NeuroImage*, 89:23–34, 2014.

[96] Andrew Melbourne, Eliza Orasanu, Zach Eaton-Rosen, Joanne Beckmann, Alexandra Saborowska, David Atkinson, Neil Marlow, and Sebastien Ourselin. Characterizing microstructure and shape of the extremely preterm 19 year-old corpus callosum. In *ISMRM*, 2016.

[97] Andrew Melbourne, Eliza Orasanu, Zach Eaton-Rosen, M Jorge Cardoso, Joanne Beckmann, Lorna Smith, David Atkinson, Neil Marlow, and Sebastien Ourselin. Analysis of brain volume in a 19 year-old extremely preterm born cohort. In *ISMRM*, 2016.

[98] Andrew Melbourne, Nicolas Toussaint, David Owen, Ivor Simpson, Thanasis Anthopoulos, Enrico De Vita, David Atkinson, and Sebastien Ourselin. NiftyFit: a Software Package for Multi-parametric Model-Fitting of 4D Magnetic Resonance Imaging Data. *Neuroinformatics*, 2016.

[99] Laura R Ment, Deborah Hirtz, and Petra S Hüppi. Imaging biomarkers of outcome in the developing preterm brain. *The Lancet Neurology*, 8(11):1042–1055, 2009.

[100] E K Miller and J D Cohen. An integrative theory of prefrontal cortex function. *Annual Review of Neuroscience*, 24:167–202, jan 2001.

[101] Marc Modat, Gerard R Ridgway, Zeike a Taylor, Manja Lehmann, Josephine Barnes, David J Hawkes, Nick C Fox, and Sébastien Ourselin. Fast free-form deformation using graphics processing units. *Computer Methods and Programs in Biomedicine*, 98(3):278–284, jun 2010.

[102] Pim Moeskops, Manon J N L Benders, and Karina J Kersbergen. Development of Cortical Morphology Evaluated with Longitudinal MR Brain Images of Preterm Infants. *PLoS ONE*, 10(7), 2015.

[103] Tamanna Moore, Enid M Hennessy, Samantha J Johnson, and Elizabeth S Draper. Neurological and developmental outcome in extremely preterm children born in England in 1995 and 2006: the EPICure studies. *British Medical Journal*, 7961(December):1–13, 2012.

[104] Andriy Myronenko and Xubo Song. Point set registration: Coherent Point Drift. *IEEE Transactions on Pattern Analysis and Machine Intelligence*, 32(12):2262–75, 2010.

[105] A C Nagasunder, H c Kinney, S Blueml, C J Tavare, T Rosser, F H Gilles, M D Nelson, and A Panigraphy. Abnormal Microstructure of the Atrophic Thalamus in Preterm Survivors with Periventricular Leukomalacia. *American*, 32:11–13, 2011.

[106] Chiara Nosarti, Elena Giouroukou, Elaine Healy, Larry Rifkin, Muriel Walshe, Abraham Reichenberg, Xavier Chitnis, Steven C R Williams, and Robin M Murray. Grey and white matter distribution in very preterm adolescents mediates neurodevelopmental outcome. *Brain*, 2008.

[107] Kenichi Oishi, Susumu Mori, Pamela K Donohue, Thomas Ernst, Lynn Anderson, Steven Buchthal, Andreia Faria, Hangyi Jiang, Xin Li, Michael I Miller, Peter C M van Zijl, and Linda Chang. Multi-contrast human neonatal brain atlas: application to normal neonate development analysis. *NeuroImage*, 56(1):8–20, 2011.

[108] Eliza Orasanu, Pierre-Louis Bazin, Andrew Melbourne, Marco Lorenzi, Herve Lombaert, Nicola J Robertson, Giles Kendall, Nikolaus Weiskopf, Neil Marlow, and Sebastien Ourselin. Longitudinal analysis of the preterm cortex using multi-modal spectral matching. In *Medical Image Computing and Computer-Assisted Intervention (MICCAI)*, 2016.

[109] Eliza Orasanu, Andrew Melbourne, M Jorge Cardoso, Herve Lomabert, Giles S Kendall, Nicola J Robertson, Neil Marlow, and Sebastien Ourselin. Cortical folding of the preterm brain: a longitudinal analysis of extremely preterm born neonates using spectral matching. *Brain and Behavior*, 488:1–18, 2016.

[110] Eliza Orasanu, Andrew Melbourne, M Jorge Cardoso, Marc Modat, Andrew M Taylor, Sudhin Thayyil, and Sebastien Ourselin. Average probabilistic brain atlases for post-mortem newborn and stillborn populations and application to tissue segmentation. In *ISMRM*, 2014.

[111] Eliza Orasanu, Andrew Melbourne, M Jorge Cardoso, Marc Modat, Andrew M Taylor, Sudhin Thayyil, and Sebastien Ourselin. Brain volume estimation from post-mortem newborn and fetal MRI. *NeuroImage: Clinical*, 6:438–444, 2014.

[112] Eliza Orasanu, Andrew Melbourne, M Jorge Cardoso, Marc Modat, Andrew M Taylor, Sudhin Thayyil, and Sebastien Ourselin. Fully automated estimation of brain volumes in post-mortem newborn and stillborn infants. In *ISMRM*, 2014.

[113] Eliza Orasanu, Andrew Melbourne, Zach Eaton-Rosen, David Atkinson, Joshua Lawan, Joanne Beckmann, Neil Marlow, and Sebastien Ourselin. Local shape analysis of the thalamus in extremely preterm born young adutls. In *ISMRM*, page 565, 2016.

[114] Eliza Orasanu, Andrew Melbourne, Zach Eaton-Rosen, David Atkinson, Alexandra Saborowska, Joanne Beckmann, Neil Marlow, and Sebastien Ourselin. Cortical folding patterns in extremely preterm born young adults. In *ISMRM*, page 4085, 2016.

[115] Eliza Orasanu, Andrew Melbourne, Herve Lombaert, M Jorge Cardoso, Stian Flage Johnsen, Giles S Kendall, Nicola J Robertson, Neil Marlow, and Sebastien Ourselin. Prefrontal Cortical Folding of the Preterm Brain: A Longitudinal Analysis of Preterm-Born Neonates. In *STIA Conference Proceedings (MICCAI Workshop)*, pages 3–12, 2015.

[116] Eliza Orasanu, Andrew Melbourne, Marco Lorenzi, Marc Modat, Zach Eaton-Rosen, Nicola J Robertson, Giles Kendall, and Sebastien Ourselin. Tensor Spectral Matching of Diffusion Weighted Images. In *SAMI Conference Proceedings (MICCAI Workshop)*, pages 35–44. MIDAS Journal, 2015.

[117] Eliza Orasanu, Andrew Melbourne, Marc Modat, Marco Lorenzi, Herve Lombaert, Zach Eaton-Rosen, Nicola Robertson, Giles Kendall, Sebastien Ourselin, Translational Imaging Group, United Kingdom, Academic Neonatology, and United Kingdom. Mapping longitudinal white matter changes in extremely preterm born infants. In *ISMRM*, 2016.

[118] Jose M Ornelas-Aguirre, Gonzalo Vázquez-Camacho, Laura Gonzalez-Lopez, Araceli Garcia-Gonzalez, and Jorge I Gamez-Nava. Concordance between premortem and postmortem diagnosis in the autopsy: results of a 10-year study in a tertiary care center. *Annals of Diagnostic Pathology*, 7(4):223–230, 2003.

[119] T. Michael O'Shea, L Corbin Downey, and Karl K C Kuban. Extreme prematurity and attention deficit: epidemiology and prevention. *Frontiers in Human Neuroscience*, 7(September):1–5, 2013.

[120] Stanley Osher and James A Sethian. Fronts Propagating with Curvature- Dependent Speed: Algorithms Based on Hamilton-Jacobi Formulations. *Journal of Computational Physics*, 49:12–49, 1988.

[121] Sebastien Ourselin, Alexis Roche, Gerard Subsol, Xavier Pennec, and Nicholas Ayache. Reconstructing a 3D structure from serial histological sections. *Image and Vision Computing*, 19(2000):25–31, 2001.

[122] Martyn N J Paley, A R Hart, M Lait, and Paul D Griffiths. An MR-compatible neonatal incubator. *The British Journal of Radiology*, 85(July):952–958, 2012.

[123] Jennifer Parker, Ann Mitchell, Anastasia Kalpakidou, Muriel Walshe, Chiara Nosarti, Paramala Santosh, Larry Rifkin, John Wyatt, Robin M Murray, and Matthew Allin. Cerebellar growth and behavioural & neuropsychological outcome in preterm adolescents. *Brain*, 131:1344–1351, 2008.

[124] Savannah C Partridge, Pratik Mukherjee, Roland G Henry, Steven P Miller, Jeffrey I Berman, Hua Jin, Ying Lu, Orit Glenn, Donna M Ferriero, James Barkovich, and Daniel B Vigneron. Dif-

fusion tensor imaging: Serial quantitation of white matter tract maturity in premature newborns. *NeuroImage*, 22(3):1302–1314, 2004.

[125] Christopher R Pierson, Rebecca D Folkerth, Saraid S Billiards, Felicia L Trachtenberg, Mark E Drinkwater, Joseph J Volpe, and Hannah C Kinney. Gray matter injury associated with periventricular leukomalacia in the premature infant. *Acta Neuropathol*, 114:619–631, 2007.

[126] G Postelnicu, L Zollei, and B Fischl. Combined volumetric and surface registration. *IEEE Transactions on Medical Imaging*, 28(4):508–522, 2009.

[127] Marcel Prastawa, John H Gilmore, Weili Lin, and Guido Gerig. Automatic segmentation of MR images of the developing newborn brain. *Medical Image Analysis*, 9:457–466, 2005.

[128] Sandra Rees and Terrie Inder. Fetal and neonatal origins of altered brain development. *Early Human Development*, 81(9):753–761, 2005.

[129] Emma C Robinson, Saad Jbabdi, Matthew F Glasser, Jesper Andersson, Gregory C Burgess, Michael P Harms, Stephen M. Smith, David C Van Essen, and Mark Jenkinson. MSM: A new flexible framework for multimodal surface matching. *NeuroImage*, 100:414–426, 2014.

[130] Steffen Ross, Lukas Ebner, Patricia Flach, Rolf Brodhage, Stephan Bolliger, Andreas Christe, and Michael J Thali. Postmortem whole-body MRI in traumatic causes of death. *American Journal of Roentgenology*, 199(6):1186–92, dec 2012.

[131] F Rousseau, O Glenn, B Iordanova, D Vigneron, J Barkovich, and C Studholme. A Novel Approach to High Resolution Fetal. In *Medical Image Computing and Computer-Assisted Intervention (MICCAI)*, pages 548–555, 2005.

[132] D Rueckert, L I Sonoda, C Hayes, D L Hill, M O Leach, and D J Hawkes. Nonrigid registration using free-form deformations: application to breast MR images. *IEEE Transactions on Medical Imaging*, 18(8):712–21, 1999.

[133] Mert R Sabuncu, Benjamin D Singer, Bryan Conroy, E Bryan, Peter J Ramadge, and James V Haxby. Function-based Intersubject Alignment of Human Cortical Anatomy. *Cerebral Cortex*, 20(1), 2010.

[134] Andreas B Schuh, Maria Murgasova, Antonios Makropoulos, Christian Ledig, Serena J Counsell, Jo V Hajnal, Paul Aljabar, and Daniel Rueckert. Construction of a 4D Brain Atlas and Growth Model Using Diffeomorphic Registration. In *STIA Conference Proceedings (MICCAI Workshop)*, volume 1, pages 27–37, 2015.

[135] A Serag, V Kyriakopoulou, M A Rutherford, A D Edwards, and J V Hajnal. A Multi-channel 4D Probabilistic Atlas of the Developing Brain: Application to Fetuses and Neonates. *Annals of the BMVA*, 2012(3):1–14, 2012.

[136] Martin I Sereno, Antoine Lutti, Nikolaus Weiskopf, and Frederic Dick. Mapping the Human Cortical Surface by Combining Quantitative T1 with Retinotopy. *Cerebral Cortex*, 23(9):2261–2268, 2013.

[137] Divyen K Shah, Peter J Anderson, John B Carlin, Masa Pavlovic, Kelly Howard, Deanne K Thompson, Simon K Warfield, Terrie E Inder, Victoria Infant, Brain Study, Australian Centre, and Neuropsychological Studies. Reduction in Cerebellar Volumes in Preterm Infants: Relationship to White Matter Injury and Neurodevelopment at Two Years of Age. *Pediatric Research*, 60(1), 2006.

[138] Mahsa Shakeri, Herve Lombaert, Alexandre N Datta, Nadine Oser, Laurent Létourneau-guillon, Laurence Vincent, Florence Martin, Domitille Malfait, Alan Tucholka, and Sarah Lippé. Statistical shape analysis of subcortical structures using spectral matching. *Computerized Medical Imaging and Graphics*, pages 1–14, 2016.

[139] Yonggang Shi, Rongjie Lai, Danny J J Wang, Daniel Pelletier, David Mohr, Nancy Sicotte, and Arthur W. Toga. Metric optimization for surface analysis in the Laplace-Beltrami embedding space. *IEEE Transactions on Medical Imaging*, 33(7):1447–1463, 2014.

[140] John G Sled, Alex P Zijdenbos, and Alan C Evans. A Nonparametric Method for Automatic Correction of Intensity Nonuniformity in MRI Data. *IEEE Transactions on Medical Imaging*, 17(1):87–97, 1998.

[141] Yuqing Song, Conghua Xie, and Jianmei Chen. Medical image segmentation using characteristic function of Gaussian Mixture Models. *3rd International Conference on Biomedical Engineering and Informatics*, 1:375–379, 2010.

[142] Sara Soria-Pastor, Monica Gimenez, Ana Narberhaus, Carles Falcon, Francesc Botet, Nuria Bargallo, Josep Maria, and Carme Junque. Patterns of cerebral white matter damage and cognitive impairment in adolescents born very preterm. *International Journal of Developmental Neuroscience*, 26:647–654, 2008.

[143] Joshua V Stough, Jeffrey Glaister, Chuyang Ye, Sarah H Ying, Jerry L Prince, and Aaron Carass. feature classification. In *Medical Image Computing and Computer-Assisted Intervention (MICCAI)*, number 17, pages 169–176, 2014.

[144] Martin Styner, Ipek Oguz, Shun Xu, Dimitrios Pantazis, and Guido Gerig. Statistical Group Differences in Anatomical Shape Analysis using Hotelling T2 metric. In *SPIE Medical Imaging*, page 65123, 2007.

[145] Andrew Sweet and Xavier Pennec. Log-Domain Diffeomorphic Registration of Diffusion Tensor Images. In *WBIR*, pages 198–209, 2010.

[146] Tuomas Tallinen, Jun Young Chung, François Rousseau, Nadine Girard, and Julien Lefèvre. On the growth and form of cortical convolutions. *Nature Physics*, 12(February):588–593, 2016.

[147] Sudhin Thayyil, Enrico De Vita, Neil J Sebire, Alan Bainbridge, David Thomas, Roxanne Gunny, Kling Chong, Mark F Lythgoe, Xavier Golay, Nicola J Robertson, Ernest B Cady, and Andrew M Taylor. Post-mortem cerebral magnetic resonance imaging T1 and T2 in fetuses, newborns and infants. *European Journal of Radiology*, 81(3):232–238, 2012.

[148] Sudhin Thayyil, Nicola J Robertson, A Scales, M A Weber, T S Jacques, and Neil J Sebire. Prospective parental consent for autopsy research following sudden unexpected childhood deaths: a successful model. *Archives of Disease in Childhood*, 94(5):354–358, 2009.

[149] Sudhin Thayyil, Nicola J. Robertson, Neil J. Sebire, and Andrew M. Taylor. Post-mortem MR and CT imaging in fetuses, newborns and children: an evidenced based approach. *Diagnostic Histopathology*, 16(12):565–572, 2010.

[150] Sudhin Thayyil, Neil J Sebire, Lyn S Chitty, Angie Wade, W K Chong, Oystein Olsen, Roxana S Gunny, Amaka C Offiah, Catherine M Owens, Dawn E Saunders, Rosemary J Scott, Rod Jones, Wendy Norman, Shea Addison, Alan Bainbridge, Ernest B Cady, Enrico De Vita, and Nicola J Robertson. Post-mortem MRI versus conventional autopsy in fetuses and children: a prospective validation study. *The Lancet*, 6736(13):1–11, 2013.

[151] Sudhin Thayyil, Neil J Sebire, Lyn S Chitty, Angie Wade, Oystein Olsen, Roxana S Gunny, Amaka Offiah, Dawn E Saunders, Catherine M Owens, W K Kling Chong, Nicola J Robertson, and Andrew M Taylor. Post mortem magnetic resonance imaging in the fetus, infant and child: a comparative study with conventional autopsy (MaRIAS Protocol). *BMC Pediatrics*, 11(1):120, 2011.

[152] Deanne K Thompson, Terrie E Inder, Nathan Faggian, Simon K Warfield, Peter J Anderson, Lex W Doyle, and Gary F Egan. Characterization of the corpus callosum in very preterm and full-term infants utilizing MRI. *NeuroImage*, 55(2):479–490, 2012.

[153] Jean A Tkach, Noah H Hillman, Alan H Jobe, Wolfgang Loew, Ron G Pratt, Barret R Daniels, Suhas G Kallapur, Beth M Kline-Fath, Stephanie L Merhar, Randy O Giaquinto, Patrick M Winter, Yu Li, Machiko Ikegami, Jeffrey A Whitsett, and Charles L Dumoulin. An MRI system for imaging neonates in the NICU: initial feasibility study. *Pediatric Radiology*, 42(11):1347–56, 2012.

[154] Arthur W Toga, Paul M Thompson, and Elizabeth R Sowell. Mapping brain maturation. *Trends in Neurosciences*, 29(3):148–59, 2006.

[155] Fabio Triulzi, Cecilia Parazzini, and Andrea Righini. Magnetic resonance imaging of fetal cerebellar development. *The Cerebellum*, 5(3):199–205, 2006.

[156] David C Van Essen. A tension-based theory of morphogenesis and compact wiring in the central nervous system. *Nature*, 385(6614):313–318, 1997.

[157] K Van Leemput, F Maes, D Vandermeulen, and P Suetens. Automated model-based tissue classification of MR images of the brain. *IEEE Transactions on Medical Imaging*, 18(10):897–908, 1999.

[158] B C Vemuri, J Ye, Y Chen, and C M Leonard. Image registration via level-set motion: Applications to atlas-based segmentation. *Medical Image Analysis*, 7:1–20, 2003.

[159] Tom Vercauteren, Xavier Pennec, Aymeric Perchant, and Nicholas Ayache. Diffeomorphic demons: efficient non-parametric image registration. *NeuroImage*, 45:S61—-S72, 2009.

[160] Joseph J Volpe. Brain injury in premature infants: a complex amalgam of destructive and developmental disturbances. *Lancet Neurology*, 8(1):110–24, 2009.

[161] M D Waehnert, J Dinse, M Weiss, M N Streicher, P Waehnert, S Geyer, R Turner, and P Bazin. NeuroImage Anatomically motivated modeling of cortical laminae. *NeuroImage*, 93:210–220, 2014.

[162] San Mei Wang, Chang Shuan Yang, Yu Hou, Xiu Wei Ma, Zhi Chun Feng, and Yu Zhen Liao. Perinatal occipital lobe injury in children: Analysis of twenty-one cases. *Pediatric Neurology*, 47(6):443–447, 2012.

[163] Yi Wang, Aditya Gupta, Zhexing Liu, Hui Zhang, Maria L. Escolar, John H. Gilmore, Sylvain Gouttard, Pierre Fillard, Eric Maltbie, Guido Gerig, and Martin Styner. DTI registration in atlas based fiber analysis of infantile Krabbe disease. *NeuroImage*, 55(4):1577–1586, 2011.

[164] Dieter Wolke and Renate Meyer. Cognitive status, language attainment, and prereading skills of 6-year-old very preterm children and their peers: the Bavarian Longitudinal Study. *Developmental Medicine and Child Neurology*, 41(2):94–109, 1999.

[165] Nicholas S Wood, Neil Marlow, Kate Costeloe, Alan T Gibson, and Andrew R Wilkinson. Neurologic and developmental disability after extremely preterm birth. *The New England Journal of Medicine*, 343(6):378–384, 2000.

[166] Keith J. Worsley, JE Taylor, F Carbonell, MK Chung, E Duerden, B Bernhardt, O Lyttelton, M Boucher, and AC Evans. SurfStat: A Matlab toolbox for the statistical analysis of univariate and multivariate surface and volumetric data using linear mixed effects models and random field theory. In *Human Brain Mapping*, pages 3–5, 2009.

[167] R. Wright, A. Makropoulos, V. Kyriakopoulou, P.a. Patkee, L.M. Koch, M.a. Rutherford, J.V. Hajnal, D. Rueckert, and P. Aljabar. Construction of a foetal spatio-temporal cortical surface atlas from in utero MRI: Application of spectral surface matching. *NeuroImage*, 120:467–480, 2015.

[168] Shugao Xia, Xiaobo Li, Ariane E Kimball, Mary S Kelly, Iris Lesser, and Craig Branch. Thalamic shape and connectivity abnormalities in children with attention deficit / hyperactivity disorder. *Psychiatry Research: Neuroimaging*, pages 1–7, 2012.

[169] Hui Xue, Latha Srinivasan, Shuzhou Jiang, Mary Rutherford, David Edwards, Daniel Rueckert, and Joseph V Hajnal. Automatic segmentation and reconstruction of the cortex from neonatal MRI. *NeuroImage*, 38(3):461–77, 2007.

[170] B T Thomas Yeo, Mert R Sabuncu, Tom Vercauteren, Nicholas Ayache, Bruce Fischl, and Polina Golland. Spherical demons: fast diffeomorphic landmark-free surface registration. *IEEE Transactions on Medical Imaging*, 29(3):650–68, 2010.

[171] B T Thomas Yeo, Tom Vercauteren, P Fillard, Xavier Pennec, P Gotland, Nicholas Ayache, and O Clatz. DTI registration with exact finite-strain differential. *IEEE International Symposium on Biomedical Imaging: From Nano to Macro*, 3(1):700–703, 2008.

[172] Xintian Yu, Yanjie Zhang, Robert E Lasky, Sushmita Datta, Nehal A Parikh, and A Ponnada. Comprehensive Brain MRI Segmentation in High Risk Preterm Newborns. *PLoS ONE*, 5(11), 2010.

[173] Paul Yushkevich, Joseph Piven, Heather Cody Hazlett, Rachel Gimpel Smith, Sean Ho, James C Gee, and Guido Gerig. User-guided 3D active contour segmentation of anatomical structures: significantly improved efficiency and reliability. *NeuroImage*, 31(3):1116–28, 2006.

[174] Hui Zhang, Torben Schneider, Claudia A Wheeler-Kingshott, and Daniel C Alexander. NODDI: practical in vivo neurite orientation dispersion and density imaging of the human brain. *NeuroImage*, 61(4):1000–1016, 2012.

[175] Hui Zhang, Paul Yushkevich, Daniel C Alexander, and James C Gee. Deformable registration of diffusion tensor MR images with explicit orientation optimization. *Medical Image Analysis*, 10:764–785, 2006.